Sintering of Zirconium Diboride-Silicon Carbide (ZrB2-SIC) and Titanium Dibor'ide-Silicon Carbide (TiB2-SIC) Ceramic Composites and Laser Surface Treatment : Application in Low Temperature Protonic Ceramic Fuel Cells (LTPCFCs)

Dayang Salyani Binti Abang Mahmod

UNIVERSITÉ DE LIMOGES
ÉCOLE DOCTORALE
Science et Ingénierie en Matériaux,
Mécanique, Energétique et Aéronautique
FACULTÉ DES SCIENCES ET TECHNIQUES
Laboratoire Sciences des Procédés Céramiques et
Traitements de Surfaces (UMR CNRS – 7315)

UNIVERSITI MALAYSIA SARAWAK
DOCTORAL PROGRAM
Advanced Material
FACULTY OF ENGINEERING
Department of Mechanical and
Manufacturing Engineering

THÈSE

DOCTEUR DE L'UNIVERSITÉ DE LIMOGES
Spécialité: Matériaux Céramiques et Traitements de Surface
et
DOCTOR OF PHILOSOPHY
UNIVERSITI MALAYSIA SARAWAK
Speciality: Advanced Material

Présentée et soutenue par

Dayang Salyani Binti ABANG MAHMOD

Octobre, 2017

Sintering of Zirconium Diboride-Silicon Carbide (ZrB_2-SiC) and Titanium Diboride-Silicon Carbide (TiB_2-SiC) Ceramic Composites and Laser Surface Treatment: Potential Application in Low Temperature Protonic Ceramic Fuel Cells (LTPCFCs)

JURY:

Président	Andrew Ragai Henry Rigit	Professor Ir. Dr., Universiti Malaysia Sarawak Kota Samarahan, Sarawak, Malaysia.
Rapporteurs	Laurence Latu-Romain	Associate Professor, Université de Grenoble Alpes, France.
	Ramesh Singh A/L Kuldip Singh	Professor Ir. Dr., University of Malaya, Kuala Lumpur, Malaysia.
	Pang Suh Cem	Professor Dr., Universiti Malaysia Sarawak, Kota Samarahan, Sarawak, Malaysia.
Examinateurs	Jean-Claude LABBE	Professor Emeritus, Université de Limoges, France.
	Nicolas GLANDUT	Associate Professor, Université de Limoges, France.
	Amir Azam KHAN	Professor Dr., Universiti Malaysia Sarawak, Kota Samarahan, Sarawak, Malaysia.

To the Parents Who Nurtured Me

To Brothers and Sister Who Never Doubt on Me

To the Teachers Who Inspired, Engaged, Passionate and Amazing Human Beings

To All Who Continue to Fight

And

To the Readers

“Never give up on anybody, Miracles do happen”

“It’s supposed to be hard. If it wasn’t hard, everyone would do it.

The hard is what makes it great”. – Wisdom for the Seeker.

Acknowledgements

Thank you to the Malaysia-France University Centre (MFUC) for giving me the opportunity to experience the Joint-Ph.D Program and also to the Ministry of Higher Education, Malaysia (MOHE) for granted me MyPhD scholarship from MyBrain15 Scholarship Program 2013 and to the Embassy of France in Kuala Lumpur, Dr. Maxime Feraille, and Mr. Xavier Flamand. The French Ministry of Foreign Affairs for the French Government's Scholarship that funded my stay and the Campus France Organization for managing my stay in Limoges, France. I would like to sincerely thank Dr. Thierry Chartier, the director of the Laboratory Science des Procédés Céramiques et de Traitements de Surface (SPCTS UMR CNRS 7315), Limoges for having me in the lab. Without your support and confidence towards the Ph.D. Joint Thesis Program, it would have been impossible.

I would like to express my gratitude to my dedicated and patient supervisors Professor Amir Azam Khan, Associate Professor Dr. Nicolas Glandut and Professor Emeritus Jean-Claude Labbe from both universities, Universiti Malaysia Sarawak (UNIMAS) and Université de Limoges (UNILIM) for their wisdom, expert advice, and encouragement throughout this thesis process. Thank you for your patience and faith in me.

Not forgetting to the colleagues at UNILIM and Centre Européen de la Céramique (CEC), Science des Procédés Céramiques et de Traitements de Surface (SPCTS); Pawel Sokolowski, Aleksandra Malachowska, Rolando Candidato, Launay Yann, Ariane Sado-Maguekam Patrice Duport, Richard Mayet, Marion Vandenhengan, Solange Degot and more that I could not mention here, thank you for your precious time for sharing, teaching and guiding me at your own best. Finally, to the staffs and colleagues at UNIMAS for their support, critiques, comments and enthusiasm and to anyone directly or indirectly involved in helping hands throughout the 4 years of struggling. **Thank you** for being part of my life.

Abstract

Sintering and laser are a remarkable technology with a broad range of applications especially material processing. It offers a wide variety of desired surface properties depending on the type of usage. Sintering allows high reliability and repeatability to the large mass production. Laser benefits in the aspect of energy saving compared to conventional surface heat treatment due to the heating is restricted and localized only to the required area. Therefore, this research aims to develop a silica-glass-layer onto a porous non-oxide, Zirconium Diboride-Silicon Carbide (ZrB_2-SiC) and Titanium Diboride-Silicon Carbide (TiB_2-SiC) ceramic composites by sintering and laser surface treatment for potential application in the Low-Temperature Protonic Fuel Cells (LTPCFCs). ZrB_2-SiC and TiB_2-SiC mixed powders at different composition were cold-pressed around 40 MPa under ambient environment. Next, the composites were pressureless sintered at 1900 °C and 2100 °C for 2.5 h dwell time under argon atmosphere, respectively. The pressureless sintering was conducted by Nabertherm furnace and followed by surface treatment via an ytterbium fibre laser (Yb). A new round spiral laser pattern was inspired, designed and scanned onto the surface of pellets to obtain a smooth glass surface layer that acted as proton-conducting (electrolyte) while preserving the beneath structures of laser-treated pellets that served as an electrode. Characterization techniques such as Scanning Electron Microscope (SEM) equipped with Energy Dispersive X-Ray Spectroscopy (EDS) and X-ray Diffraction (XRD) were performed accordingly onto the samples. Pressureless sintering of 61 mol.% ZrB_2-SiC and 61 mol.% TiB_2-SiC pellets at 1900 °C exhibited ca. 29% porosity. The resulting porosity was in the best range of effectiveness for gas diffusion. SEM micrographs revealed the formation of semi-glassy layer on the surface of sintered 61 mol.% ZrB_2-SiC pellets. The bulk structures remained unaffected and unoxidized. SEM micrographs and EDS patterns displayed that silica (SiO_2) at a thickness of 8 μm, presence on the surface of ZrB_2-SiC structures. It demonstrated that the surface treatment by Yb-fibre laser on sintered ZrB_2-SiC ceramic composites at 1900 °C had accomplished. The laser surface treatment was ineffective for TiB_2-SiC pellets due to several bubbles formation and crack deflection. Nevertheless, at higher magnification of the SEM for laser-treated ZrB_2-SiC ceramic composites, cracks were observed. Therefore, the pressureless sintering at high temperature was conducted to improve the ZrB_2-SiC structural properties. Sintering at 2100 °C had demonstrated increment of density and at 80 mol.% ZrB_2-SiC sintered pellet unpredictably exhibited the presence of boron carbide (B_4C) compounds. SEM micrographs revealed the dark cuboidal shapes and

XRD patterns identified as B_4C peaks. The reactions of B_4C formation were proposed and supported by thermodynamic analysis. In conclusion, the present research had developed a glassy layer on the surface of ZrB_2-SiC ceramic composites which has potential in the application of LTPCFCs. It proved that B_4C was possible to be developed by pressureless sintering at 2100 °C and it might assist in developing better morphology for ZrB_2-SiC ceramic composites.

Keywords: Sintering, Ceramic, Boron Carbide, Laser, Oxidation

Frittage des Composites Diborure de Zirconium-Carbure de Silicium (ZrB_2-SiC) et Diborure de Titane-Carbure de Silicium (TiB_2-SiC)

Traitement de Surface par Laser :

Application Potentielle aux Piles à Combustibles Fonctionnant à Basse Température.

Résumé

Le frittage et le traitement par laser sont des techniques remarquables, couramment utilisées dans de nombreux domaines d'applications du fait des qualités qu'ils confèrent aux surfaces traitées. Ces technologies permettent de substantielles économies d'énergie comparée aux traitements de surfaces conventionnels. Le chauffage est par ailleurs, strictement localisé à la zone choisie. Notre recherche a pour objectif de développer une fine couche de verre de silice à la surface de céramiques poreuses composites : le diborure de zirconium-carbure de silicium (ZrB_2-SiC) et le diborure de titane-carbure de silicium (TiB_2-SiC) frittées avec une porosité contrôlée d'environ 30%. La principale application de ces matériaux concerne les piles à combustibles protoniques fonctionnant à basse température (de type LTPCFCs). Les poudres ZrB_2-SiC et TiB_2-SiC sont soigneusement mélangées et pressées à froid dans un moule à la pression de 40 MPa. Le frittage naturel est conduit dans un four à 1900 et 2100 °C durant 2,5 heures, sous atmosphère contrôlée d'argon. Après polissage, le traitement de surface est effectué par laser verre-ytterbium. Les paramètres du traitement ont été optimisés (puissance et trajet du faisceau laser, temps de traitement, atmosphère) et ont permit d'obtenir une couche superficielle d'un verre à forte conduction protonique, sans affecter la structure et la composition des couches situées au-dessous de la surface. Les échantillons ont été caractérisés en utilisant les méthodes classiques : EDS, XRD, MEB, microscopie optique. Les meilleurs résultats ont été obtenus avec des échantillons de composition 61 mol. % ZrB_2-SiC et 61 mol. % TiB_2-SiC traités thermiquement a 1900 °C. La porosité obtenue, de l'ordre de 30%, assure une bonne circulation des gaz. La couche de verre produite sur le composite ZrB_2-SiC, d'une épaisseur moyenne de 8 µm, est continue et exempte de macro fissuration. Une microfissuration est cependant détectée par MEB aux plus forts grossissements. Les essais ont été conduits à plus haute température de frittage (2100 °C) et avec des compositions différentes dans le but d'améliorer les propriétés du substrat. ZrB_2-SiC. A la composition de 80 mol. % ZrB_2-SiC les analyses révèlent la présence de cristaux de forme cuboïdale, attribuée à la formation de carbure de bore B_4C dont la formation est admise par l'analyse thermodynamique. Les essais sur le composite ZrB_2-SiC conduisent à l'apparition de bulles et de défauts dans la couche de verre. Une optimisation des conditions de traitement sera nécessaire pour contrôler ce phénomène. Cette étude démontre qu'il est possible de développer des couches poreuses de matériaux céramiques de type ZrB_2-SiC, et de former à leur surface une couche de verre dense et exempte de fissuration par

traitement laser. Les propriétés générales de cette couche permettent d'envisager une utilisation comme électrolyte solide dans les piles à combustibles de type LTPCFCs.

Mots Clés : *Frittage, Composite, ZrB_2- SiC, Carbure de bore, Laser et Oxidation,*

Table of Contents

List of Tables

List of Figures

List of Abbreviations and Acronyms

AFC	Alkaline Fuel Cell
BSE	Backscattering Electrons
CNC	Computer Numerical Control
CPOX	Catalytic Partial Oxidation
DMFC	Direct Methanol Fuel Cell
EDS	Energy Dispersive Spectrometry
FC	Fuel Cell
HAZ	Hazard Analysis Software
LTPCFCs	Low-Temperature Protonic Ceramic Fuel Cells
LSM	Lanthanum Strontium Manganite
MCFC	Molten Carbonate Fuel Cell
MEA	Membrane Electrode Assembly
MIEC	Mixed Ionic Electronic Conducting
PAFC	Phosphoric Acid Fuel Cell
PCFCs	Protonic Ceramic Fuel Cells
PEMFCs	Polymer Electrolyte or Protonic Exchange Membrane Fuel Cells
PROX	PReferential Oxidation
SE	Secondary Electrons
SEDA	Sustainable Energy Development Association Malaysia
SEM	Scanning Electron Microscopy
SOFCs	Solid Oxide Fuel Cells
TEA	Transversely Excited Atmosphere
TEC	Thermal Expansion Coefficient
TPB	Triple Phase Boundary
UHTC	Ultra-High Temperature Ceramics
WGS	Water-Gas Shift
XRD	X-ray Diffraction
YSZ	Yttria-stabilized Zirconia

List of Symbols

°C	Degree celsius
Ø	Diameter
GPa	Gigapascal
kPa	Kilopascal
kW	Kilowatt
MPa	Megapascal
MW	Megawatt
µm	Micron/micrometer
mtoe	Million tonnes of oil equivalent
mol.%	Molar percent
nm	Nanometer
Ωcm^2	Ohm centimeter square
ppm	Parts per million
%	Percent
W	Watt
$mScm^{-1}$	MiliSiemens per centimeter

GENERAL INTRODUCTION

Research Background

As reported by Enerdata Global Energy Statistical Yearbook 2016, the total world energy consumption increases every year. Since 2015, Malaysia population is about 30.7 million, and the total energy consumption grew at the rapid pace of 4.5%/year, on average from 2000 to 2015 (Enerdata 2016). An agency which is known as Sustainable Energy Development Association Malaysia (SEDA) is aware of the importance of alternative energy. Therefore, the objective is to increase alternative energy contribution to the national power generation mix. Meanwhile, for the European Commission, their focus is to find a sustainable energy source as it is the basis for all human progress besides the global warming and the tightening supplies of energy (Fabbri et al. 2012). Moreover, it is the biggest European Union (EU) research program that is known as Horizon 2020 to support the transition of a reliable, sustainable, and competitive energy system. In summary, the development of alternative energy in the global arena is crucial due to the depletion of hydrocarbon resources, need for emission reduction and the efficient production of electricity.

The alternative energy consists of solar, wind, hydropower, geothermal, bioenergy, ocean energy and fuel cell technology. The fuel cell is one of the reliable alternative sources due to its ability to convert fuel to power with higher conversion efficiency compared to the conventional combustion engines, clean and eco-friendly, installation simplicity, operation stability and ease of maintenance (Evans et al. 2011; Novaresio et al. 2012). Moreover, it is the best choice because of its quiet (stealth vehicles), flexible (portable power systems), and energy-efficient operation. Principally, classified by the electrolyte type and also by the material of construction or fabrication techniques and system requirements (Holland et al. 2001), it remains attractive as an alternative energy and interesting to be studied.

Solid oxide fuel cell (SOFC) has been on top of the list of fuel cells. It is mainly due to its outstanding capability in achieving larger electrical efficiencies and fuel flexibility compared to other fuel cell types (Evans et al. 2011; Tseronis et al. 2008; Richter et al. 2009; Spivey & Edgar 2012; Napoli et al. 2015). It emits only power, heat, and water as the emission. The power and heat can be fully utilized with the existing of cogeneration. It comprises of a solid

electrolyte that can avoid corrosive environments, two porous electrodes, a fuel channel, an oxidant channel and the electrical interconnect. It operates in the range of temperature of 500 °C to 1000 °C, and the typical stack size is 1 kW to 2 MW.

The electrolyte is the key component of SOFC as it determines the operating temperature of the system. It must be sufficiently dense to prevent gas leakages and possess a negligible electronic conductivity to avoid electrode crosstalk (disturbance caused by the electric field). So far, the materials used for electrolyte are zirconia, ceria, lanthanum and the most common is yttria-stabilized zirconia (YSZ). It possesses an adequate oxide-ion conductivity (~0.13 S/cm at 1000 °C), and shows a desirable phase stability in both oxidizing and reducing atmospheres. However, it causes ohmic losses. The ohmic losses result from resistance to the flow of ions in the electrolyte and electrons through the cell hardware and various interconnections. The corresponding voltage drop is essentially proportional to the current density, hence the term "ohmic losses" (Mahato et al. 2015; Zhang et al. 2007). Unfortunately, to avoid the ohmic losses, SOFC based on YSZ electrolyte requires operating at the temperature of 800 to 1000 °C. It is the primary cause for the limitation of SOFC commercialization (Fabbri et al. 2012). Therefore, in order to compensate the ohmic losses, fabrication of thin solid electrolyte is necessary (Lee et al., 2012; Menzler et al., 2010; Tietz et al., 2002).

Several techniques to produce solid electrolyte with a specific thickness are investigated. The high ranges of thickness are obtained by employing tape casting (50-300 µm) and slurry coating (100-150 µm). Other techniques are lamination and sintering (10-30 µm), reactive magnetron (≤ 16 µm), screen printing (7-10 µm), vacuum slip casting (10 µm), wet powder spraying (10-25 µm) and electrochemical vapour deposition (EVD) (40 µm) (Mahato et al. 2015).

As reported by Saigal (2007), the fabrication of electrolyte via sputtering has been successful in fabricating an electrolyte of 40 nm thickness. Nevertheless, the thinner electrolyte has an impact on increasing of ohmic polarization (arises due to electrical resistance in the cell components). Thus, the electrolyte-supported cell has been transitioned to the electrode-supported cells. This greatly reduces the ohmic loss attributed to the electrolyte thickness, which enables lower operating temperature and higher performance (Wachsman et al., 2011).

However, studies by Tiez et al. (2002) differed from other researchers (Huijsmans, 2001; Menzler et al., 2010; Saigal, 2007; Wachsman et al., 2011). They mentioned that the contribution of ohmic losses from the thinner electrolyte had been rather small. In agreement with Ralph et al. (2001), it is hard to fabricate thinner electrolyte below 1 µm without forming small pinholes or cracks during cross mixing of gases. Therefore, they suggested improving the electrode performance by lowering the operating temperature (Tietz et al. 2002).

The fuel cell electrode comprised of two porous structures; cathode and anode, which allow gas transport to the reaction sites. For anode, accessible materials such as nickel (Ni), copper (Cu), and lanthanum (La) are typically employed for the fuel cell. The most common anode for SOFC is Ni/YSZ cermet (Badwal et al., 1996; Menzler et al., 2010; Minh, 2004; Zhu et al., 2003). It is because of its low cost and stability. However, Ni-based anode has a low tolerance toward sulphur poisoning, poor redox stability, and carbon deposition (Jiang 2012; Sun & Stimming 2007).

The anode can be fabricated with various techniques such as screen printing (3-7 µm; 30-60 µm), painting (150 µm), vacuum slip casting (5-15 µm), slurry coating (80-100 µm) and EVD (100 µm) (Mahato et al. 2015). The anode is least studied compared to cathode and electrolyte. It still needs to be further improved by extending the anode material at different operating temperatures.

Several types of cathode materials are lanthanum (La), gadolinium (Gd), praseodymium (Pr), strontium (Sr) and yttria (Y_2O_3). Lanthanum manganite ($LaMnO_3$) with substitutions of strontium or calcium at the A-site is frequently employed as the cathode (Badwal & Foger 1996; Minh 2004; Menzler et al. 2010; Huijsmans 2001; Jeffrey W. Fergus 2006; Ralph et al. 2001). It is due to its stability in an oxidizing atmosphere. Also, it has electrical conductivity and thermal expansion that match YSZ electrolyte (Ralph et al. 2001).

At the lower operating temperature, the cathode has encountered the polarization loss issue. To tackle this problem, incorporation of electrolyte material is necessary without performance loss. The electrolyte material will be forming oxygen conducting for oxygen ions between the lanthanum strontium manganite (LSM) cathode materials. Huijsmans (2001) has determined that an optimum thickness of this structure should be around 15 µm to ensure the transfer of oxygen charge carriers into the electrolyte. This thickness is applied

in the porous zirconia network. Several cathode fabrication techniques employed are screen printing (50-150 μm), sputtering, painting (150 μm), wet powder spraying (50 μm), extrusion and sintering (2200 μm-cathode tube) and atmosphere plasma spraying (150-200 μm) (Mahato et al. 2015).

This research has been actively pursued to ensure the achievement of improved electrolyte and electrode either by exploring the new material or innovating the existing content or upgrading the fabrication techniques to cope with the present challenges in more efficient and intelligent approach. Therefore, for better understanding of the fuel cell material, an intensive study of favourable ceramic composites and the development of ceramic structures that contributes to the lower operating temperature and investigation of a dynamic range (efficient) of substrate porosity are further required. Hence, the identification of the problem statements is described in the next section.

Problem Statements

Solid oxide fuel cell (SOFC) is a promising candidate to be commercialized as an alternative energy as they have cheaper catalyst (nickel electrode cheaper than platinum) and larger electrical efficiencies (Tseronis et al. 2008). However, operating at high temperature (500-1000 ^{o}C) has led to the problem of preheating the cell. If hydrogen leaks and exposes to an ignition source, it can create an explosion. Moreover, it limits the selection of material (Zhi et al. 2012) as well as increases the difficulty of the fabrication process. In the case of low conductivity electrolyte, it might decrease the performance of the cell. The ohmic losses over the electrolyte are also the reason of the cell performance inefficiency (Huijsmans 2001).

To be feasible for SOFC to operate at low temperature, it requires a desirable ceramic that exhibits higher oxygen conductivity and thinner electrolyte structures to reduce ohmic losses. Besides that, high cost, operating complexities, and shorter operational life have also been constraining the SOFC to be employed widespread. To compensate the real drawbacks, numerous efforts to reduce the SOFC operating temperature are still being developed, such as thin-film technology for the electrolyte, alternative electrolyte and electrode materials, hybrid and nano-composites material and much more (Huijsmans, 2001; Zhu et al., 2003). These efforts will significantly extend the fuel cell lifetime, provide better flexibility in materials selection and then reduce the overall system cost (Zhi et al. 2012).

Meanwhile, a study by Lonné et al. (2011) has shown the glass-coated electrodes exhibited features such as the small thickness of 3.5 µm and high protonic conductivity ca. 2 $mScm^{-1}$. Also, the electrode formation is rich in ZrB_2, electronically conductive, porous and has an oxygen concentration gradient. It indicates that the classical furnace oxidation developed a protonic conducting SiO_2-rich glass layer which can be fabricated and applied as proton-conducting fuel cell or protonic ceramic fuel cell (PCFC). Nevertheless, this process is causing the oxidation of the whole area of the sample.

The hot pressing technique is a typical fabrication process for the ceramic composites to achieve higher densification (Appetecchi et al., 2003; Huang et al., 2006; Xie et al., 2006; Zhu, 2003). Even so, extreme conditions are required at a higher temperature and moderate pressures or vice-versa (Fahrenholtz et al. 2008). Meanwhile, pressureless sintering is regularly employed for ZrB_2-SiC ceramic processing. It is commonly provided by incorporation of sintering aids, or additives such as TiB_2, Si_3N_4, SiC, $MoSi_2$, Mo, Fe, Ni, B_4C and C (Mallik et al., 2017; Mashhadi et al., 2015; Peng, 2008; Zhang et al., 2009a).

Other researchers presented the laser studies for a variety of treatments such as surface densification of porous ZrC and still maintain the beneath structure without traces of oxidation into zirconia or oxycarbide (Bacciochini et al. 2009). Surface densification of porous ZrB_2-39 mol.% SiC ceramic composites have also proven the capability of the laser as there are no traces of carbon and oxygen beneath the samples. It is suggested to be employed for low temperature protonic ceramic fuel cells (Lonné et al., 2011, Lonné et al., 2012a, Lonné et al., 2012b). This previous research represented reliability of laser for the surface oxidation process. The majority of them is utilizing the similar design, scanning patterns (Kido et al., 2011; Kido et al., 2014a; Kido et al., 2014b; Lonné et al., 2011, Lonné et al., 2012a). Nonetheless, the study of laser oxidation to promote a glassy layer act as a protonic conduction property is still lacking. After considering the topic, it is compelling to conduct research to further investigate the ceramic material properties and structures fabricated by laser. Since the existing materials are susceptible to high operating temperature, an in-depth study on the laser formation layers and substrates in term of structural and chemical analysis are conducted.

Research Gap

From the problem statements, the research gaps are described:

a) The investigation on the microstructural development of ZrB_2 and TiB_2 ceramic were mostly conducted by hot pressing with additives and sintering aids (Buyakova et al., 2016; Chao et al., 2015; Eakins et al., 2011; Guo, 2014; Patel et al., 2012; Sai Krupa et al., 2013; Shahedi Asl et al., 2016; Zhao et al., 2014b). The present study investigates ZrB_2 (100 mol.%), ZrB_2-SiC (10 to 30 mol.% SiC) and TiB_2-SiC (39 mol.% SiC) ceramic composites of various compositions by pressureless sintering (sintering that performs just using temperature) at different sintering temperatures (1900 °C and 2100 °C).

b) Previous research also widely studied the oxidation process by the furnace. This process tend to oxidize the whole substrates (Beauvais-Réveillon et al., 1995; Blokhina et al., 2014; Guo et al., 2010; Ivanov et al., 2014; Karlsdottir et al., 2009a, Karlsdottir et al., 2009b; Qu et al., 2016; C. Tian et al., 2011; Zhang et al., 2011). In the present study, the oxidation process of sintered ZrB_2-SiC and TiB_2-SiC ceramic composites were conducted via ytterbium fibre laser that produced localized heat under ambient surrounding.

c) In recent years, the reported studies employed several scanning patterns to modify the ceramic properties. Among them are the single spot, lattice pattern, stripe hatch, meander hatch and chess board hatch (Cui et al., 2015; Jwad et al., 2016; Kido et al., 2011; Kido et al., 2014a; Lonné, 2011; Qian et al., 2013). A different scanning pattern was configured and employed for laser oxidation to promote the glassy layer on the surface of ceramic composites.

Research Hypotheses

There are two significant hypotheses to be investigated:

a) The pressureless sintering of ZrB_2-SiC and TiB_2-SiC ceramic composites without any sintering additives, at 1900 °C and above is expected to produce adequate porosity in the range of 20% to 40% that is suitable for gas diffusion in the protonic conducting/ceramic fuel cell.
b) High-temperature pressureless sintered ceramics for the system of ZrB_2-SiC and TiB_2-SiC would result in suitable density, which is favourable to be laser-treated to obtain a continuous glassy layer on the substrate for protonic conduction.

Research Objectives

To fulfil the research hypotheses, identification of research objectives are as follows:

a) To sinter ZrB_2-SiC and TiB_2-SiC ceramic composites by pressureless sintering at different temperatures under argon flow and to study and compare sintered ZrB_2-SiC and TiB_2-SiC ceramic composites properties and select the desirable one to be laser-treated.
b) To treat the selected sintered ceramic composites by ytterbium fibre laser under ambient surrounding using a new laser scanning pattern, optimal scanning rate, and laser power to promote continuous semi-molten/molten surface layer.
c) To characterize and investigate the characteristics of ceramic composite substrates and molten/semi-molten layer based on the morphological, structural, and chemical analyses.
d) To propose the reaction mechanism occurring in the ZrB_2-SiC ceramic composite system at the temperature above 1900 °C depending on the results and thermodynamic analyses.

Scope of Research

The research scope covers only the aspects of producing the ZrB_2-SiC and TiB_2-SiC ceramic composites using pressureless sintering and selects the favourable among both types of ceramic composites to be treated by ytterbium fibre laser for the oxidation process. The comparison of the sintered and oxidized pellets was investigated. The essential characterization techniques were selected and conducted to limit the range of research. There are two compelling reasons for conducting studies on fuel cell which are for the environmentally friendly system and economic benefits.

Most of the published journal articles on the ceramic composites are done using furnace, which is a conventional oxidation process. In this study, the laser approach for surface oxidation is highlighted. Several significant findings in the laser system are discussed. Laser as an alternative approach to the oxidation process, particularly for ceramic composite materials will be introduced. Followed by the potential oxidized ceramic composites use in PCFCs. The laser approach will compensate the weaknesses of the conventional furnace approach. Moreover, the discovery of new laser scanning pattern is beneficial to the present and the future study as it may be the solution for developing substrates which can be designed for a specific pattern, precise and more detailed. It will speed up the entire oxidation process that leads to time-saving work and cost saving technology. However, the process is very much depending on the working surface area of the materials. The laser surface oxidation approach can also be upgraded for industrial application.

This research extends the opportunities in the development of PCFCs at lower temperatures than SOFCs (250 °C to 550 °C versus ≥ 600 °C) and overcomes the deficiency of SOFCs and PEMFCs. It will be valuable towards the future reference by researchers, especially fuel cell system. Apart from that, it will also attract keen interest and provide a positive impact for material processing and other potential applications such as microelectronic devices and sensors. Overall, this research gives a tremendous impact on increasing and enhancing the knowledge and research skills that can be contributed to the society.

CHAPTER 1

Literature Review

The chapter describes the concept of alternative energy exclusively for the solid oxide fuel cells (SOFCs), and protonic ceramic fuel cells (PCFCs) that include the basic configurations, benefits, challenges, and applications. It also provides the bibliography related to the ceramic composite system to be proposed and used in the fuel cell. Moreover, it discusses the previous and potential treatment approaches for oxidation, thus determining the central focus of sintering and laser treatment in the process of producing molten/semi-molten surface layer.

1.1 Sintering of Ceramics

Sintering is a treatment, when thermal energy is applied to a powder compact, and it is densified, and the average grain size increases. The process involves the heat treatment of powder compacts at elevated temperatures. It is usually at $T > 0.5Tm$ [K], in the temperature range where diffusional mass transport is appreciable. Tm is the melting temperature in Kelvin. For monolithic material, sintering temperature should be greater than half the melting point for solid state sintering. The sintering is an essential step for ceramic fabrication due to their high melting point. The brittleness of ceramics causes the solidified microstructures cannot be modified through additional plastic deformation and re-crystallization. Also, the resulting coarse grains would act as fracture initiation sites whereby during an impact event, the point at which the first crack begins to form in the test specimen. Low thermal conductivities of ceramics, in contrast to metals, cause large temperature gradient, thus thermal stress and shock in melting-solidification of ceramics.

1.1.1 Sintering Fundamental

Two notable sintering variables are material variables; (i) powder: chemical composition of the powder compact, powder size, powder shape, powder size distribution, the degree of powder agglomeration etc., (ii) chemistry: composition, impurity, non-stoichiometry, homogeneity, etc. It influences the powder compressibility and sinterability (densification and grain growth). Secondly are thermodynamic variables such as temperature, time, atmosphere, pressure , heating, and cooling rate and etc. (Rahaman, 2003).

Figure 1.1 displays the six distinct mechanisms that contribute to the sintering of crystalline particles. It represents a clearer version of the occurrence of sintering mechanism. For sintering to be conducted, there are a few criteria that are required to make it happen. First, the presence of mechanism for material transport, which are diffusion and viscous flow. Secondly, heat is a source of energy to activate and sustain this material transport. The most important and beneficial uses of sintering in the modern era are the fabrication of sintered parts of all kinds, including powder-metallurgical parts and bulk ceramic components.

All the mechanisms can be classified into two groups: (i) densifying mechanisms and (ii) non-densifying mechanisms, depending on whether they can cause shrinkage or densification of the compact. Non-densifying mechanisms include surface diffusion, lattice diffusion from the particle surfaces to the neck, and vapor transport, i.e. mechanisms 1,2, and 3 which leads to neck growth without densification. In contrast, grain boundary diffusion and lattice diffusion from the grain boundary to the pore, i.e., mechanisms 4 and 5, are densifying mechanisms, which are the most important contributions to the densification of polycrystalline ceramics. Diffusion from the grain boundary to the pore is beneficial to both neck growth and densification. Mechanism 6, also leads to neck growth and densification, but it is more pronounced in the sintering of metal powders.

The objectives of sintering are to produce sintered parts with reproducible and if possible, designed microstructure through control of sintering variables. Micro-structural control means the control of grain size, sintered density, and size and distribution of other phases including pores. In most cases, the final goal of micro-structural control is to prepare a fully dense body with a fine grain structure.

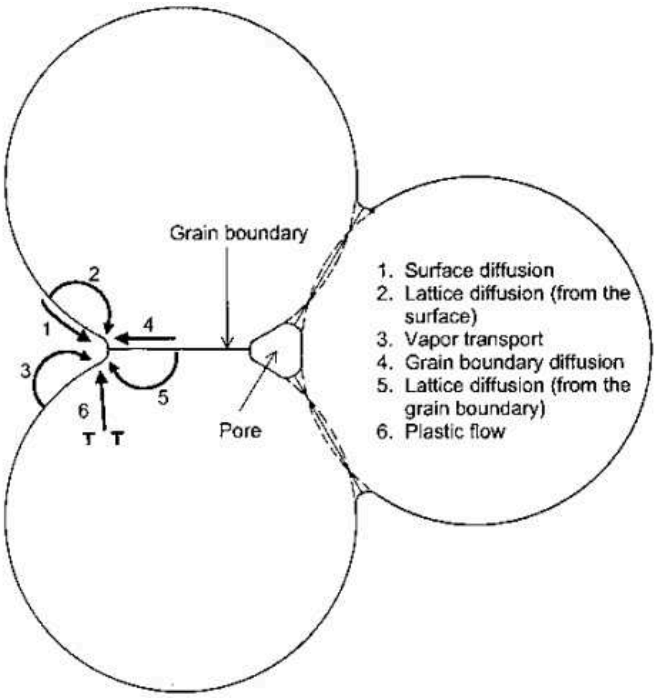

Mechanism 1 to 3
Lead to neck growth without densification (non-densifying).

Mechanism 4 to 5
Diffusion from the grain boundary to the pore permits neck growth as well as densification.

Mechanism 6
Lead to neck growth and densification (Common in metal

Figure 1.1: Six distinct mechanisms contribute to the sintering of a consolidated mass of crystalline particles: (1) surface diffusion, (2) lattice diffusion from the surface, (3) vapor transport, (4) grain boundary diffusion, (5) lattice diffusion from the grain boundary, and (6) plastic flow. Only mechanisms 4 to 6 lead to densification, but all cause the necks to grow and so influence the rate of densification (Rahaman, 2003).

The powder does not melt; instead, the joining together of the particles and the reduction in the porosity (i.e., densification) of the body, as required in the fabrication process, occurs by atomic diffusion in the solid state. This type of sintering is usually referred to as solid state sintering. It is the simplest case of sintering, the processes occurring, and their interaction can be complex. The driving force for sintering is the reduction in surface free energy of the consolidated mass of particles. This reduction in energy can be accomplished by atom diffusion processes that lead to either densification of the body (by transport matter from inside the grains into the pores) or coarsening of the microstructure (by rearrangement of matter between different parts of the pore surfaces without leading to a decrease in the pore volume).

The effects of key material and processing parameters such as temperature, particle (or grain) size, applied pressure, and the gaseous atmosphere on the densification and coarsening processes are well understood. The rates of these processes are enhanced by

higher sintering temperature and by fine particle size. Densification is further enhanced by the application of an external pressure. A key issue that has received increasing attention in recent years is the effect of micro-structural inhomogeneities present in the green body (e.g., density, grain size, and compositional variations) (Rahaman, 2017; Shojai and Mäntylä, 2001). It is now well recognized that inhomogeneities can seriously hinder the ability to achieve high density and to adequately control the fabricated microstructure.

Ostwald ripening is an observed phenomenon in solid (or liquid) solutions which describes the evolution of an inhomogeneous structure over time. When a phase precipitates out of a solid, energetic factor will cause large precipitates to grow, drawing material from the smaller precipitates, which shrink. Ostwald ripening (or disproportionation) is the process of disappearance of small particles or droplets by dissolution and deposition on the larger particles or droplets. The driving force for Ostwald ripening is the difference in solubility between the small and the large particles. The smaller particles (with higher radius of curvature) are more soluble than the larger ones (with lower radius of curvature). With time, the smaller particles or droplets dissolve, and their molecules diffuse in the bulk and become deposited on the larger ones. This results in a shift of the particle or droplet size distribution to larger values (Tadros 2013).

1.1.2 Pressureless Sintering

There are two types of sintering, which are solid state sintering and liquid phase sintering. Other than that, is activated sintering. A method used to create objects from metal powders. It is performed in the gaseous atmosphere which enhances aggregation of metal particles and hot consolidation. Hot consolidation methods are applied to obtain fully dense metal powder compacts with controlled microstructures. This encompasses many diverse operations, including uniaxial hot pressing and pressure sintering, hot isostatic pressing, hot extrusion and hot forging. These types are known as conventional sintering processes. Others are the rate-controlled sintering, plasma sintering, and microwave sintering and cold sintering (This technology is a protocol to achieve dense ceramic solids at extremely low temperatures (< 300 °C) via integrating particle, particle-fluid interface control, and external pressure to allow the cold sintering process (CSP). The major variables which determine sinterability and the sintered microstructure of a powder compact may be divided into two categories: material variables and process variables. Here, the focus is on pressureless

sintering. This is because of it is an affordable manufacturing technology and requires less preparation of the components (Pines 2004).

Most of previous studies reported on ZrB_2-based ceramics were prepared by hot-pressed sintering rather than pressureless sintering. This is mainly due to the low sinterability of ZrB_2-based ceramics which has become a major obstacle that restrains them from having an economical process. As the consequences, spark plasma sintering (SPS) and reactive hot processing (RHP) and hot pressing (HP) have been preferred for processing the diborides (Zhang et al., 2009b). However, hot pressing is only limited to a simple geometric shape and fabrication of complex components requires expensive and time consuming diamond machining (Zhu et al., 2009).

Recently, there are few articles that reported regarding the benefits that can be offered by using pressureless sintering (Chamberlain et al., 2006; Mukhopadhyay et al., 2007; Wang et al., 2009; Zhang et al., 2009b; Zhu et al., 2009). Despite weak sinterability (lacking the power to perform sintering) that could be compensated by employing the sintering aid, pressureless sintering could be one of the efforts to contribute to the more economical process. Pressureless sintering is advantageous in term of its ability to fabricate components to near-net end shape using standard powder processing methods, thus reduces the processing cost (Guo, 2009). By employing pressureless sintering, the formations of pellet shapes are not limited to one shape only and can be varied into variety form of shapes. It is also one single step of furnace (single speed furnaces, only have one stage of heat output – high). The time, cost and material waste could be reduced, which associates with diamond machining to the final component dimensions (Chamberlain et al., 2006; Yan et al., 2006; Zhang et al., 2009b; Zhang et al., 2008; Zhu et al., 2009). Sintering is also more efficient because multiple articles can be produced in a single furnace run. Fine-grained ZrB_2 has been successfully densified by pressureless sintering with the addition of 2–4 wt.% boron carbide (B_4C) (Zhang et al., 2008).

1.2 Laser Technology for Material Processing

Light amplification by stimulated emission of radiation or simply known as the laser is essentially a coherent, convergent and monochromatic beam of electromagnetic radiation with the wavelength ranging from ultraviolet to infrared, wide range of energy/power and

beam-modes/configurations. It can deliver very low (~ mW) to extremely high (1–100 kW) focused power with a precise spot size/dimension and interaction/pulse time (10^{-3} to 10^{-15} s) onto any kind of substrate through any medium (Dahotre et al., 2008; Majumdar et al., 2003; Samant et al., 2009b; Steen et al., 2010). Three basic components of a laser are as follows (Steen & Mazumder 2010):

a) Active medium (to amplify light).
b) The pumping source (to excite the active medium to the amplifying state).
c) Optical resonator (to provide an optical feedback).

The wavelength, λ, of a laser is decided by the energy difference as the excited species is stimulated to a lower energy level, E [$E = hc/\lambda$, where h is Planck's constant (6.626×10^{-34} Js) and c is the velocity of light (3×10^{8} ms^{-1})]. In general, the quantum states refer to molecular vibration levels for long-wavelength lasers, to electron orbit levels for visible laser radiation and to ionization effects of ultraviolet lasers.

Laser technology is renowned as an alternate solution for material processing. It will become a better material processing technology in the future considering there are many previous and recent studies that are still ongoing for advancement and establishment of the laser. Laser types such as CO_2, Nd:YAG and fibre lasers are the most popular system for material processing. The excimer and diode laser types are also fast appearing in the research world. Among the reasons, the laser is an attractive technology for flexible manufacturing systems ultimately due to it can perform several processes. This can be viewed in Figure 1.2 that shows a single laser can perform several processes if the power density and interaction time are manipulated (Steen & Mazumder 2010).

Particularly, laser machining involves a high density optical energy which is incident on the surface of the workpiece and the material is removed by melting, dissociation/decomposition (broken chemical bonds causes the material to dissociate/decompose), evaporation and material expulsion from the area of laser–material interaction. Absorption of laser energy and multiple reflections (physical phenomena) that take place when the laser beam is incident on the ceramic surface includes reflection, absorption, scattering and transmission as displayed in Figure 1.3. The vital parameters

governing this process are the different ceramic properties such as reflectivity, thermal conductivity, specific heat and latent heats of melting and evaporation.

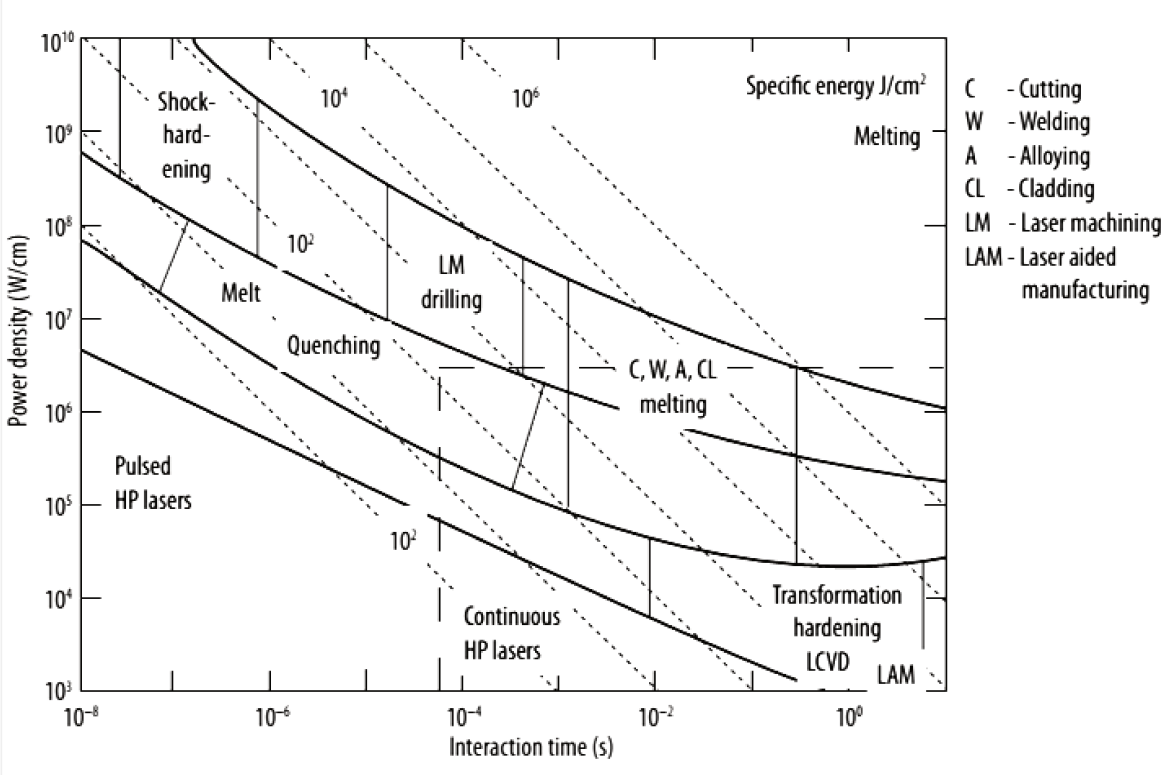

Figure 1.2: Operational regimes for various processing techniques. high-powered (HP), laser chemical vapour deposition (LCVD) (Steen & Mazumder 2010).

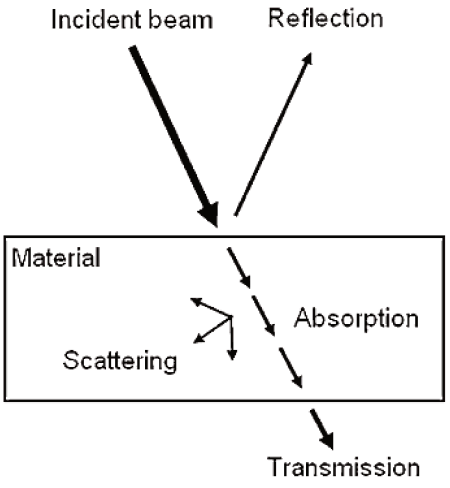

Figure 1.3: Interactions of incident laser beam with material (Dahotre et al., 2008; Samant et al., 2009b).

Apart from all the physical phenomena, absorption is significant as it is the interaction of the electromagnetic radiation with the electrons of the material. It depends on both the wavelength of the material and the spectral absorptivity characteristics of the ceramic being machined (Samant & Dahotre 2009). An important characteristic of the laser source is the wavelength, which should be well-matched to the absorption characteristics of the powder material (Stotko, 2009). The excitation energy from the laser is rapidly converted into heat and this is followed by various heat transfer processes. Conduction into the materials, convection, and radiation from the surface are the heat transfer processes. The temperature distribution within the material because of these heat transfer processes depends on the thermo-physical properties of the material (density, emissivity, thermal conductivity, specific heat, thermal diffusivity), dimensions of the sample (thickness) and laser processing parameters (absorbed energy, beam cross-sectional area). The magnitude of temperature rise due to heating governs the different physical effects in the material such as melting, sublimation, vaporization, dissociation, plasma formation and ablation, which are responsible for material removal/machining as presented in Figure 1.4.

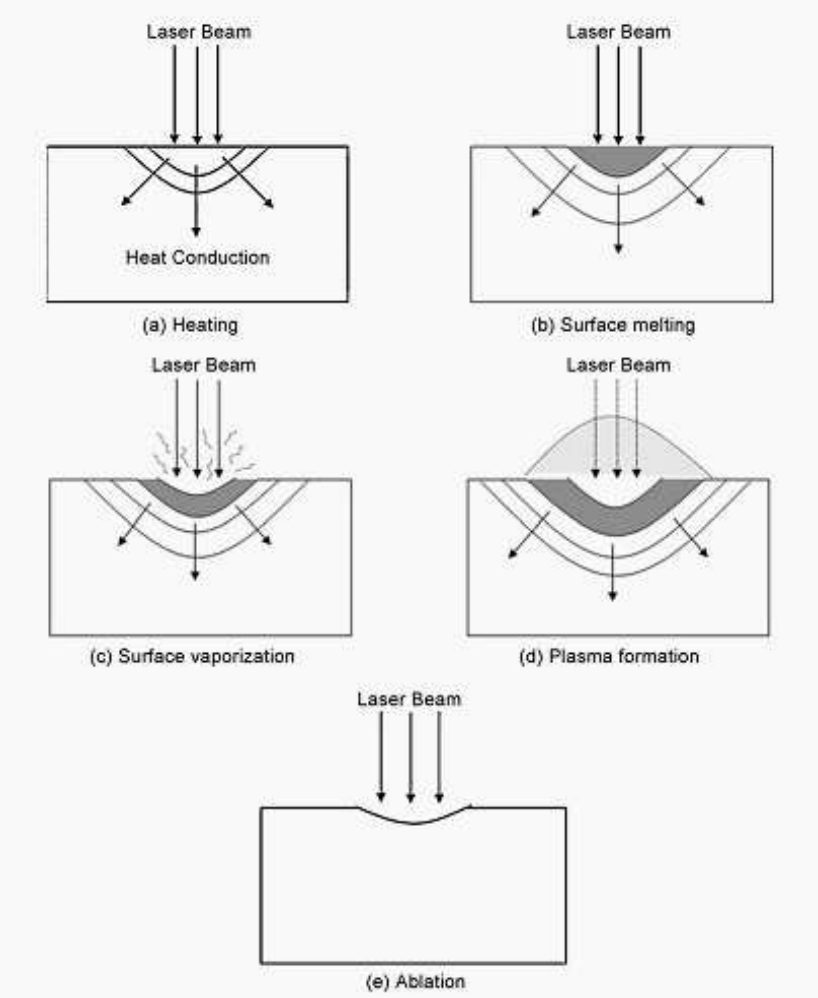

Figure 1.4: Various physical phenomena during laser–ceramic interaction (Dahotre et al., 2008; Samant et al., 2009b).

A laser is a lucrative tool due to their outstanding features which can replace mechanical material removal methods in several engineering applications (Samant & Dahotre 2009):

a) Non-contact process: Energy transfer from the laser to the ceramic through irradiation eliminates cutting forces, tool wear and machine vibration. Furthermore, the material removal rate is not affected by the maximum tool force, tool chatter or built-up edge formation, but can be controlled by varying the laser processing parameters such as input energy and processing speed.

b) Thermal process: The efficiency of laser machining depends on the thermal and, to some extent on the optical properties of the material. This makes hard or brittle materials such as structural ceramics with low thermal diffusivity and conductivity suitable for machining.

c) Flexible process: In combination with a multi-axis positioning system or robot, lasers can be used for drilling, cutting, grooving, welding and heat treating on the same machine without any necessity to transport the parts for processing them with specialized machines. In-process monitoring during the laser machining process can allow key parameters to be measured and a high level of reproducibility can be attained.

1.2.1 Current Status of Laser Research

Numerous investigations in laser technology have been conducted and are still underway in the efforts to expand the use of the laser. Since, there are gaps in laser knowledge, theories about how laser might work better and ideas for improvement, more research are needed. Part of them will be discussed here.

Recently, Ristić et al. (2014) investigated an analysis of neolithic ceramics surface modification induced by pulsed laser treatment (Transversely Excited Atmosphere (TEA)) CO_2 and Nd:YAG). The aims are to gain information on the choice of materials and techniques for further conservation and restoration of ceramics. Besides that, the investigation is performed to determine the surface modifications induced by pulsed laser treatment above damage threshold and considered as the significant parameter for the cleaning of cultural ceramic materials. They have concluded that different processes occur during the laser treatment because of irradiation effects. There are melting, ablation and sedimentation. Formation of the conical structures and the ceramic surface becomes more roughness are observed after the TEA CO_2 laser treatment. Meanwhile, Nd:YAG treatment produces crates on the surface and typical for the spallation mechanism (Laser induced spallation is a recent experimental technique developed to understand the adhesion of thin films with substrates). A high energy pulsed laser (typically Nd:YAG) is used to create a compressive stress pulse in the substrate, wherein it propagates and reflects as a tensile wave at the free boundary. This tensile pulse spalls/peels the thin film while propagating towards the substrate. Using theory of wave propagation in solids it is possible to extract the interface strength. The stress pulse created in this example is usually around 3-8 nanoseconds in duration while its magnitude varies as a function of laser fluence. Due to the non-contact application of load, this technique is very well suited to spall ultra-thin films (1 micrometer in thickness or less). It is also possible to mode to convert a longitudinal stress wave into a

shear stress using a pulse shaping prism and achieve shear spallation). Furthermore, the morphological modifications are depending on the laser fluencies and the number of pulses (Slavica Ristić et al., 2014).

Other researchers investigated the feasibility of laser type. In the opinion of Sun et al., (2008), concentric dual laser system is a feasible method to obtain a sintered layer with uniform surface morphology and moreover ZrB_2 required small particle size (~ 2 μm) in order to improve its surface meltability and sinterability. They have observed needle-like nanostructures on the pulsed laser sintered which was caused by the rapid cooling rate.

Investigation on laser irradiation of α-SiC ceramics in an oxygen-containing atmosphere leads to the formation of porous (loose) silica on the surface of SiC ceramics. It is due to the release of gaseous products through the layer of SiO_2 melt. The photograph of the SiC and SEM images of products formed can be observed in Figure 1.5. This study was performed because they believed that laser-induced corrosion of SiC ceramics would be one of the techniques to produce silicon oxide films on substrates (Vlasova et al. 2009).

Another researcher reported that a combination of laser sintering/melting, and induction heating techniques are used to fabricate ZrB_2–Zr ceramic–metal composite (cermet) 3-D structures using a layer by layer deposition. It allows fabricating complex-shaped structures, and joining or repairing objects made from analogous ultra-high temperature materials (Sun et al., 2009).

In the same year, a study by Bacciochini et al. (2009) had reported on surface densification of porous ZrC by a laser process. Thin films of 100%-dense zirconium carbide, ZrC, on top of ca. 30%-porous ZrC were obtained by using an ytterbium-doped fibre laser under argon atmosphere. It is shown experimentally and theoretically that oxidation into the bulk of zirconia or oxycarbide is completely avoided at the working temperature of at least 3420 °C. Apart from densification, the laser process can also be employed to purify from oxygen the surface of carbides obtained by thermal carboreduction of oxides (Bacciochini et al. 2009).

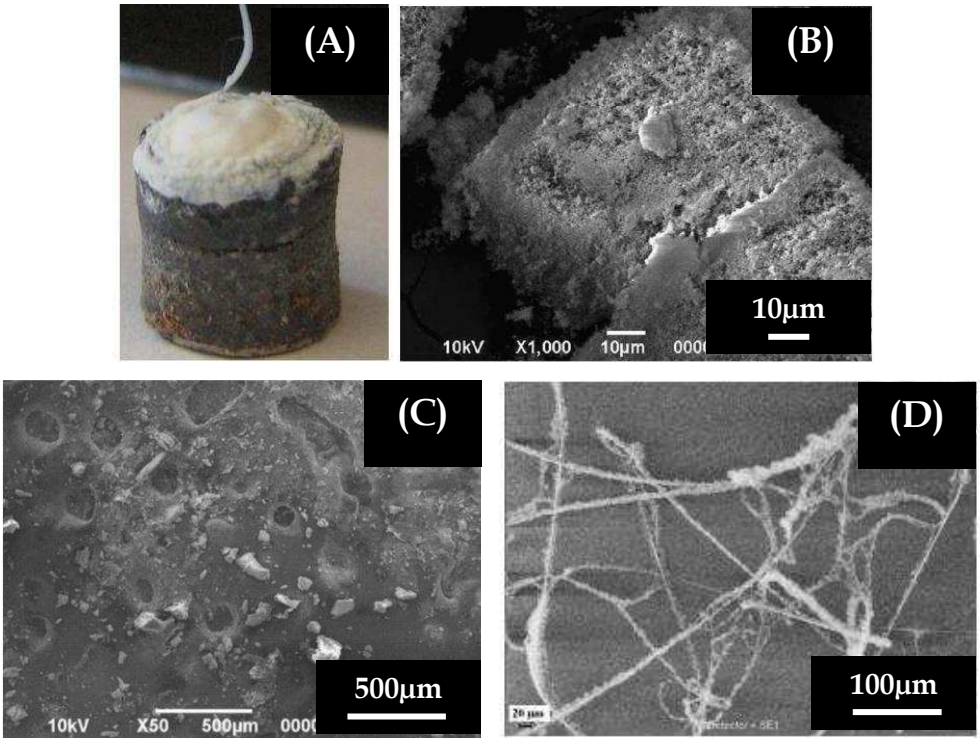

Figure 1.5: Photographs of SiC laser-irradiated at 170 W. (A) SEM micrographs of laser irradiated α-SiC ceramics, (B) Deposit formed on the surface, (C) A surface formed under a deposit, and (D) Fibres and whiskers formation (Vlasova et al. 2009).

As studied by Triantafyllidis et al. (2006), it is possible to produce the crack-free surfaces with laser treatment by employing a single laser beam without pre- and post-heating. However, it is a lack of practicability. According to them, the formation of cracks can be avoided through modification of the heat transfer conditions on the material surface, resulting in slower surface cooling rates.

Dong et al. (2015) claimed that laser melting of the electrophoretically deposited ZrB_2 powder can develop a dense and uniform ZrB_2 ceramic coating. The ZrB_2 coating formed a layer of ZrO_2, which effectively prevented unacceptable oxidation (external oxidation and deep granular internal oxidation) of a refractory Ta–W alloy in air at 2000 °C.

Further, high power diode laser (HPDL) also has the potential to be used to modify the surface of aluminium matrix composites reinforced with SiC particles. Laser surface melting allows obtaining composites with increased corrosion resistance and surface hardness (increased 48 – 80%) (Rams et al. 2007).

The laser can also be employed to synthesis the titanium oxide nanoparticles. Boutinguiza et al. (2013) have successfully obtained colloidal nanoparticles of TiO_2 in de-ionized water and ethanol using a continuous wave (CW) laser to ablate metallic Ti target.

Other researchers have reported that by employing laser, the electrical properties of ceramics can be modified. These studies have been reported by Kido et al. in different years such as modification of electrical properties of TiO_2 and Zinc peroxide (ZnO_2). (Kido et al., 2011; Kido et al., 2014a). Both reported studies are employing continuous-wave ytterbium fibre laser irradiation. Kido et al. (2014) conducted the laser irradiation on TiO_2 and reported that the modified layers are n-type semiconductor with a carrier concentration of 3.6×10^{17} cm^{-3} at 2.0 W. Previously in the year of 2011, they reported on ZnO material and the modified layers are n-type semiconductor with the carrier concentration of 1.9×10^{18} cm^{-3} at 126 W. The modified layers can be observed in Figure 1.6. These findings have great potential application in the fields of microcircuits and zinc oxide-based electronic devices.

There are varieties of laser scanning patterns that have been reported in the published journals (Kido et al., 2011; Kido et al., 2014a; Kido et al., 2014b; Lonné, 2011; Lonné et al., 2011; Lonné et al., 2012a; Lonné et al., 2012b; Mahmod et al., 2015), however some of the reports do not illustrate their laser scanning patterns.

In Figure 1.7, the most of laser scanning patterns are designed for sintering (Bacciochini et al., 2009; Lonné et al., 2012a; Qian et al., 2013; Sun et al., 2009, Sun et al., 2008). On the other hand, (Kido et al. (2014b) has successfully employed laser patterning to exhibit a high thermoelectric power and claimed it was seven times larger than that of the K-type thermocouple.

According to Honma et al. (2008), it is important to avoid crystal nucleation during laser irradiations for the patterning of homogeneous crystal lines. The proposed of laser-irradiated spots for the $Li_2Si_2O_5$ crystal growth would be 650–850 °C in order $Li_2Si_2O_5$ crystals in the lines are oriented and exhibit second harmonic generations (SHGs).

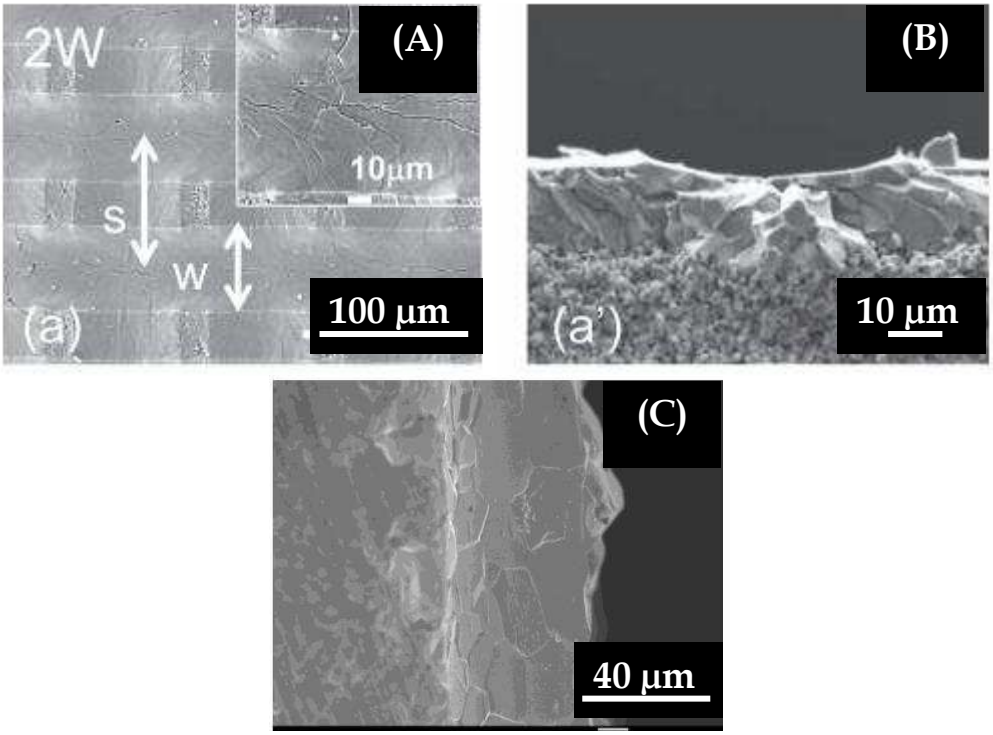

Figure 1.6: SEM images (A) Surface image of TiO_2 at 2 W, (B) Cross-sectional of TiO_2 at 2 W, and (C) Cross-sectional of ZnO irradiated at 126 W (Kido et al., 2011; Kido et al., 2014a).

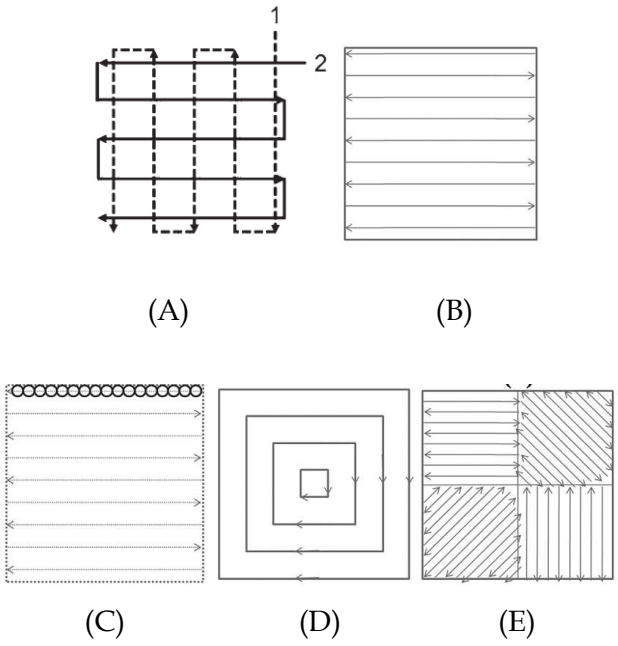

Figure 1.7: Laser scanning patterns (A) Lattice pattern (Kido et al., 2011; Kido et al., 2014b; Lonné et al., 2012b), (B) Stripe hatch with either a continue wiring mode, (C) Pulse mode, (D) Meander hatch, and (E) Chess board hatch (Qian & Shen 2013).

Meanwhile, Lusquiños et al. (2008) reported that Nd:YAG pulsed laser could be used for repairing surface defects of silicon infiltrated silicon carbide ceramics (Si-SiC) by coating using the powder blowing technique (Laser cladding using the powder blowing technique comprises a fusion of an alloy powder layer to a substrate with minimum melting of the substrate. Melting starts at the surface and the particles being heated and melted when passing the laser beam are trapped in the melt pool. This technique is used for the deposition of alloys on turbine blades, engine valves, valve seats and drilling components).

In summary, laser research can be conducted to achieve various objectives for a variety of applications. However, to achieve those objectives, trial and errors on miscellaneous materials, laser types and fresh ideas for laser execution and etc. is necessary. The full meaning of this research might not find its answer today, but will be shown in the future.

1.2.2 Laser Surface Treatment

One of the processes that is able to be conducted by laser is surface treatment or precisely surface heating. It offers a wide range of possibilities to achieve desired surface properties in order to enhance their performance for a variety of applications. This process has its own various advantages compared to conventional processing techniques such as minimizing the chemical cleanliness, controlled thermal penetration (distortion) and controlled thermal profile (shape and heat-affected zone (HAZ) location), less after-machining, remote non-contact processing and easily automated (Steen & Mazumder 2010).

Figure 1.8 illustrates the principle of laser surface treatment which has been taken from Handbook of the EuroLaser Academy, Volume 2 edited by Dieter Schuöcker. The principle of laser surface treatment is the modification of a surface as a result of interaction between a beam of coherent light, with high power density, and the surface within a specified atmosphere (vacuum, protective or processing gases). The light generated in a resonator is directed onto the surface of a sample via an optical transmission system (mirror systems or fibre optics). Starting from a given mean optical output power, the required power density, which is the ratio of power to a focused spot area, and intensity distribution throughout the beam is modified by beam focusing and/or beam shaping optics such as lenses, mirrors, scanner units or beam integrators. During the movement of the laser beam over the workpiece, a track pattern can be successively generated at the surface of a component.

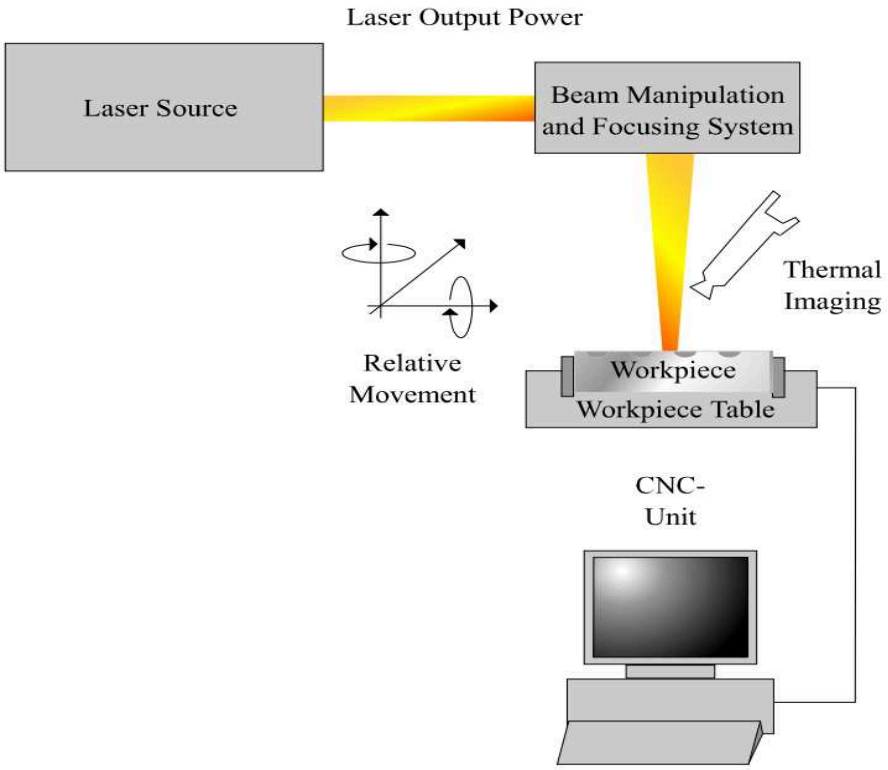

Figure 1.8: Principle of laser surface treatment (University of Miskolc 2014).

The interaction time is then determined by the cross-section of the beam and the feed rate. Depending on the type of process and the workpiece geometry translation stages, portal systems or robots can be used by which such relative movement is achieved. The section of a suitable handling system for the beam and/or workpiece depends primarily on the precision required, the processing speed and the masses that should be handled. The time for fastening and alignment of the workpiece as well as the investment costs are other important considerations (University of Miskolc 2014). A variety of laser usage in surface treatment such as surface heating for transformation hardening or annealing, scabbling, surface melting, surface alloying, surface cladding and many more. The laser surface melting is an interesting subject to be studied. An overview of several researches on laser oxidation is presented in Table 1.1.

Table 1.1: Research overview of oxidation by laser.

Years	Topics	Main Findings	Oxide	Future Prospects	References
2015	Effects of Laser Repetition Rate and Fluence on Micromachining of TiC Ceramic	With increasing laser fluence, four kinds of typical morphology were observed, including ripples, cauliflower-like particles, ball-like particles, and deposited oxide layer	Various stages of oxidation on the surface of TiC	Wear resistance tools, cutting tools and aircraft parts	(Zhang et al., 2015)
2015	Novel morphologies and growth mechanism of Cr_2O_3 oxide formed on stainless steel surface via Nd: YAG pulsed laser oxidation.	Cr_2O_3 morphologies (dendritic, gear-like, flower-like and regular hexagonal morphologies) are formed on AISI 304 stainless steel surface.	Cr_2O_3 oxide formed on stainless steel surface.	Industrial application.	(Cui et al. 2015)
2015	Oxidation of a ZrB_2 coating fabricated on Ta–W alloy by electrophoretic deposition and laser melting.	ZrB_2 coating effectively prevented the Ta–W alloy from heavy external oxidation and deep granular internal oxidation at 2000 °C in air.	ZrB_2 coating formed a layer of ZrO_2.	Aerospace industries.	(Dong et al. 2015)

Table 1.1 continued.

2010	Laser modified microstructures in ZrB_2, ZrB_2/SiC and ZrC.	Formation of a range of micro-structural features with morphologies such as needle-like nanostructures, dendrites, eutectic lamellae, nano-grained web and multifaceted polygonal surface grains.	Solid-liquid-vapour phase mechanism.	Extreme aero thermal and nuclear power generation environments.	(Jayaseelan et al. 2010)
2009	Laser irradiation of α-SiC ceramics	SiC oxidation and evolution of CO_2, porous SiO_2 forms on the target surface	Loose SiO_2 film forms.	Engineering field.	(Vlasova et al. 2009)
2008	Local laser oxidation of thin metal films: Ultra-resolution in Theory and in Practice.	Arrhenius dependence of oxidation speed from temperature raises this limit on some orders of magnitude higher than the resolution of thermal image.	Theoretical and experimental limitation on resolution depends on minimal thickness H_{min} of the oxide resistant to etching, the less are H_{min}, d_{min}, t_{min}, and the higher is the resolution δ.	Photo masks, diffractive optical elements.	(Veyko 2008)

Table 1.1 continued.

2004	Oxidation of Si surface by a pulsed Nd:YAG laser.	SiO_2 films formed by Nd:YAG laser-enhanced oxidation at low temperature.	Formation of small-spot oxide with the desired dimensions and good oxide quality.	Device applications – microelectronics.	(Aygun et al. 2004)
1997	Laser-induced oxidation of metals: state of art.	It is possible to create oxide layers (with given stoichiometric characteristics) of desired geometrical form, thickness, roughness, crystallinity and adhesion properties.	Measurement of the oxide thickness and temperature variations of the absorptivity.	MOS structures and semiconducting.	(Nánai et al. 1997)
1995	Comparison of Classical Oxidation and Laser Oxidation of a Chromium PVD Coating on a Pure-Iron Substrate.	Laser oxidation; greater oxidation rate without modifying any parameter; its morphology, its nature (chromia), and its composition (impurities incorporated in the scale) are similar.	The growth occurs by counter-current diffusions of oxygen and chromium along grain boundaries.	N/A	(Beauvais-Réveillon et al. 1995)

Laser heating/melting offers several benefits over traditional methods of studying refractory materials, e.g. ultra-high temperatures are readily, and rapidly achieved and large test samples are not required. Moreover, laser surface modification (LSM) has emerged as a flexible and convenient technique for improving the surface properties of oxide ceramics including of porous alumina (Jayaseelan et al. 2010). Among the advantages can be offered by laser-induced oxidation are the oxidation of pixels/spots with a resolution down to laser wavelength, high precision spatial-temporal control, less processing time for relatively small processing areas and finally high repeatability (Jwad et al. 2016).

1.2.3 Ytterbium Fiber Laser

Although there are many different laser types and several different laser wavelengths have been used and are being used, fibre lasers particularly have seen a dramatic increase. The industrial main reasons are due to the affordability, compactness, maintenance-free and energy efficient, saving money upfront and minimizing overhead costs, further because of fibre's excellent properties such as high brightness, efficient heat dissipation, robustness and compactness, and so on (IPG Photonics Corporation 2016; Shirakawa et al. 2011). One of them is recognized as ytterbium fibre laser. An ytterbium fibre laser (Yb) is a laser whereby the active gain medium is an optical fibre doped with rare-earth elements which is ytterbium. Yb-doped fibres have theoretical emission bandwidth ranging from 976 to 1200 nm (Royon et al. 2013). The following are the typical laser beam and process parameters:

a) Wavelength (λ) – 1072 ± 10 nm.
b) Power (W) – Maximum power of the equipment (100 W).
c) Focal spot (mm) – Original (5 mm).
d) Power density (W/m^2) – The laser intensity is dependent on beam diameter and power.
e) Processing time (t) – Depending upon the table or source velocity.
f) Laser beam polarization (p) - For rod cavities mostly statistical.

Globally, the benefits of fibre laser technology are well known and well documented such as inherent flexibility, speed, reliability and ease-of-use of laser systems compared to conventional techniques. The attractive properties of this kind of laser which makes them as one of the tools to be studied such as high energy conversion efficiency (> 30%), high power,

low heat evolution and high beam quality (M^2 = 1.1) represents the degree of variation of a beam from an ideal Gaussian beam. It is calculated from the ratio of the beam parameter product (BPP) of the beam to that of a Gaussian beam with the same wavelength. It relates the beam divergence of a laser beam to the minimum focused spot size that can be achieved. For a single mode TEM_{00} (Gaussian) laser beam, M^2 is exactly one. The M^2 value for a laser beam is widely used in the laser industry as a specification, and its method of measurement is regulated as an ISO Standard (Bacciochini et al., 2009; Kido et al., 2011; Kido et al., 2014a; Lonné et al., 2012b; Mahmod et al., 2015). Apart from Yb-fibre laser benefits are ensuring the absence of mechanical contact between the machining tool and the ceramic workpiece and a high degree of treatment localization (restrict something to a particular place). This makes laser treatment the only contact-free technique for formation of holes, cavities and other elements in ceramics (Krasnikov et al. 1999). Furthermore, rapidity is increased, energy consumption is reduced, and the cost is cheaper than the conventional sintering equipment (Lonné et al., 2012a; Lonné et al., 2012b). Table 1.2 represents some of the research overview of ytterbium fibre laser according to the recent and previous years.

Table 1.2: Research overview of ytterbium fibre laser.

Years	Topics	Main Findings	Future Prospects	References
2015	Ytterbium fibre laser welding of Ti_6Al_4V alloy.	The weld pool was efficiently shielded by adopting a reliable system of gas supplying. Contaminations and oxidations were adequately prevented.	Industries for which fuel consumption and resistance to severe working conditions are critical aspects.	(Casalino et al. 2015)
2015	Surface oxidation of porous ZrB_2-SiC ceramic composites by continuous-wave ytterbium fibre laser.	At laser power of 70 W, the sample exhibits a dense glassy SiO_2-rich layer prevents the inward oxygen diffusion into the inner bulk hence enhances the oxidation resistance.	Fuel cell application.	(Mahmod et al. 2015)
2014	Modelling of ytterbium fibre laser parameters during micro machining of Al-15 wt%Al_2O_3-MMC.	Material removal rate (MRR) is increased with the decrease of wait time and laser power. At wait time 17.5 s and laser power 500 w the MRR is maximum i.e 0.23 g/s. Due to less wait time, the possibility of heat loss is less so MRR increases.	Drilling machining.	(Ghosal et al. 2014)

Table 1.2 continued.

2014	Modification of electrical properties of TiO_2.	Modified electrical properties.	Microelectronic devices, sensors, catalysts.	(Kido et al., 2014b)
2014	Laser patterning of thermoelectric iron silicide (FeSi) on alumina substrates.	Iron silicide thermoelectric devices were successfully fabricated by direct patterning with a continuous-wave Yb-fibre laser.	Microelectronic devices, sensors, catalysts.	(Kido et al., 2014a)
2013	Synthesis of titanium oxide nanoparticles by Ytterbium fibre laser ablation	The produced titanium oxide crystalline nanoparticles show the spherical shape and are polycrystalline, exhibiting anatase as well as rutile phases.	Catalysis and biomedical engineering.	(Boutinguiza et al. 2013)
2013	Laser sintering of ceramics.	Laser sintering technology allowing net shape production of customized 3D parts in a single manufacturing operation but also a promising way for developing ceramics with structures that can hardly be made by conventional processing methods.	Construction of complicated 3D bodies.	(Qian & Shen 2013)
2012	Laser densification of porous ZrB_2-SiC composites.	Dense layer was developed on top of the porous structures. Formation of the SiO_2-rich glass layer by furnace (conventional method).	Aerospace and ceramic fuel cells.	(Lonné, N. Glandut, et al. 2012)

Table 1.2 continued.

2012	Surface densification of porous ZrB_2–39mol.% SiC ceramic composites by a laser process.	Feasibility of laser surface densification of porous ZrB_2-SiC.	Aerospace and low temperature protonic ceramic fuel cells.	(Lonné, Nicolas Glandut, et al. 2012)
2011	Modification of electrical properties of zinc oxide (ZnO).	Modified electrical properties.	Microelectronic devices, sensors, catalysts.	(Kido et al. 2011)
2011	Purification of hot-pressed ZrCO into ZrC by a laser treatment.	Purification of zirconium carbide.	Production of oxygen-free zirconium, carbide powders.	(Goutier et al. 2011)
2009	Surface densification of porous ZrC by a laser process.	Surface densification of porous ZrC. Could be used in high temperature applications where both diffusion and thermal barrier properties are needed.	To purify from oxygen the surface of carbides obtained by thermal carboreduction of oxides.	(Bacciochini et al. 2009)

1.3 Ceramics

1.3.1 Zirconium Diboride (ZrB_2)

Zirconium diboride (ZrB_2) is a transition metal boride compound and classified as an ultra-high temperature ceramics (UHTCs) -borides, carbides, and nitrides of group IV and V elements in the Periodic Table (Gonzalez-Julian et al. 2014; He et al. 2012). It is a highly covalent refractory ceramic material with a hexagonal crystal structure. Figure 1.9 represents the crystal structure of ZrB_2 (Fahrenholtz et al., 2007; Li et al., 2010; Lonné, 2011). The crystal structure of ZrB_2 is designated as AlB_2-type transition metal diborides with the space group symmetry P6/mmm. It is simply a hexagonal lattice in which close packed TM (transition metal) layers are present alternative with graphite- like B layers. Choosing appropriate primitive lattice vectors, the atoms are positioned at TM (0,0,0), B (1/3, 1/6, 1/2), in the unit cell (Fu et al. 2010).

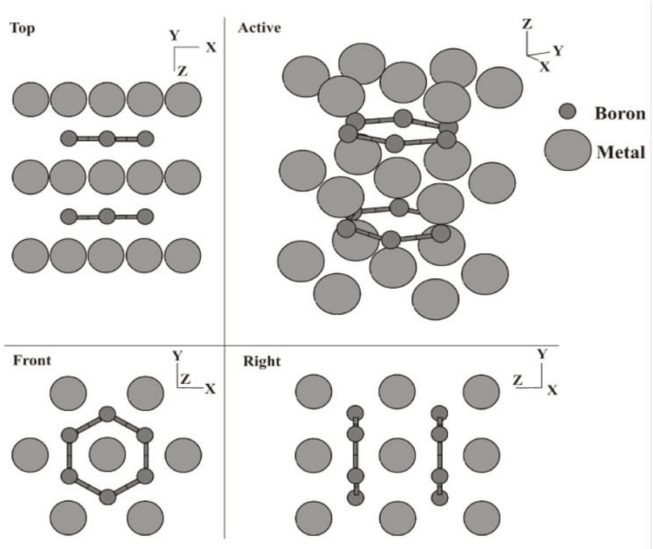

Figure 1.9: Schematic ZrB_2 crystal structure (Fahrenholtz et al., 2007; Li et al., 2010; Lonné, 2011).

Table 1.3: Zirconium diboride properties.

Properties	References
Lower theoretical density or low density (6.09 g/cm^3 to 6.11 g/cm^3)	(Lü et al. 2011; Kim et al. 2014; Tian et al. 2011; Lin et al. 2014; M. Kazemzadeh Dehdashti et al. 2013; Hu et al. 2010)
Lower cost and high melting point (> 3000 °C to 3250 °C)	(Lü et al., 2011;Ang et al., 2013; Gonzalez-Julian et al., 2014; He et al., 2012; C. Hu et al., 2010; Kazemzadeh Dehdashti et al., 2013a; Kim et al., 2014; N. Li et al., 2013; W. Li et al., 2009; Lin et al., 2014; Neuman et al., 2013; Tian et al., 2011; X. Yang et al., 2013)
High electrical and higher thermal conductivities (56-125 W/mK) than carbide or nitride ceramics	(He et al. 2012; Hu et al. 2010; Neuman et al. 2013; Maryam Kazemzadeh Dehdashti et al. 2013)
Lower electrical resistivity (7.8-22 μΩcm), high hardness (23 GPa)	(He et al. 2012; Yang et al. 2013; Li et al. 2013; Hu et al. 2010; Gonzalez-Julian et al. 2014)
Good chemical inertness against molten metal or non-basic slag	(Ang et al. 2013; Gonzalez-Julian et al. 2014; Li et al. 2009; He et al. 2012; Li et al. 2013; Lin et al. 2014)
High wear resistance and excellent resistance to thermal shock	(He et al. 2012; Kim et al. 2014; Hu et al. 2010; Lin et al. 2014; Rezaie et al. 2007)
Oxidation relative to other non-oxide engineering ceramics	(Kim et al. 2014)
Retained high strength at high-temperatures and high-elastic modulus	(Yang et al. 2013; Li et al. 2013; Tian et al. 2011)
Moderate thermal expansion, high elastic modulus (491 GPa), Good high-temperature oxidation resistance.	(Li et al. 2013; Hu et al. 2010)
Zirconium compounds can accelerate the graphitization of carbon and improve the integrated properties of carbon materials also can effectively reduce the diffusion of oxygen	(X. Li et al. 2006)

As shown in Table 1.3, these properties have made borides candidates for various applications. The benefit of electrical conductivity for application such as furnace heating elements, high-temperature electrodes, and metal evaporator boats (Zimmermann et al. 2008) including molten metal crucibles, furnace electrodes, cutting tools, wing leading edges, nose tips and propulsion components on future hypersonic aerospace vehicles whereby sharp profiles are required to reduce the aerodynamic drag (Gonzalez-Julian et al. 2014; Neuman et al. 2013; Sai Krupa et al. 2013; Fahrenholtz et al. 2008).

However, the common challenges faced in the ZrB_2-based ultra-high temperature ceramics (UHTCs) process are poor sinterability, high temperature oxidation, grain growth (Snyder et al. 2012), the brittleness and low oxidation resistance at temperature above 1200 °C (Gonzalez-Julian et al. 2014). In general, the densification of ZrB_2 powder requires very high temperatures due to the strong covalent nature of the bonding as well as its low bulk and grain boundary diffusion rates (low self-diffusion coefficients) (Kim et al., 2014; Zhang et al., 2009b).

1.3.2 Oxidation of ZrB_2

The oxidation of ZrB_2 occurs at about 700 °C (Hu et al., 2009). As explained by Karlsdottir and Halloran (2007), when monolithic $ZrB_2(s)$ oxidizes an oxide scale composed of zirconia, $ZrO_2(s)$, and boron oxide liquid, $B_2O_3(l)$, forms by the reaction equation (1.1):

$$2ZrB_2(s) + 5O_2(g) \rightarrow 2ZrO_2(s) + 2B_2O_3(l) \qquad (1.1)$$

ΔH = - 2002 kJ/mol at 700 °C

$$B_2O_3(l) \rightarrow B_2O_3(g) \qquad (1.2)$$

ΔH = + 389 kJ/mol at 1000 °C

The liquid B_2O_3 forms a continuous passive layer acting as a barrier to oxygen (O) diffusion, which results in passive oxidation of ZrB_2 and a parabolic oxidation kinetics below ca. 1000 °C. Above 1000 °C or 1400 °C, the active oxidation occurs, the oxidation resistance of ZrB_2 is poor due to volatilization of B_2O_3. The kinetics are then controlled by the competition between mass gain ($ZrO_2(s)$ and $B_2O_3(l)$ formation) and mass loss ($B_2O_3(g)$ vaporization). At higher temperatures, ZrB_2 actively oxidizes due to volatilization of the B_2O_3 liquid and forms

$B_2O_3(g)$ by direct vaporization and results in a porous, non-protective ZrO_2 layer (Hu et al., 2009; Karlsdottir and Halloran, 2007) according to the reaction equation (1.2).

Because of the poor oxidation of ZrB_2, numerous investigations to improve the oxidation resistance of ZrB_2 have been reported (Gao et al., 2013; Gonzalez-Julian et al., 2014; Guo et al., 2010; Hu et al., 2009; Hwang et al., 2007). From the various studies reported, silicon carbide (SiC) addition was found to effectively improve the oxidation resistance by promoting the formation of borosilicate glass. This borosilicate glass afforded more oxidation protection than boria since it is more viscous, has a higher melting temperature and a lower vapor pressure, and is more of a barrier to oxygen diffusion (Hu et al., 2009).

1.3.3 Titanium Diboride (TiB_2)

Titanium boride (TiB_2) is a solid refractory compound. It is among the hardest (H ≈ 33 GPa) and high stiffness (Young's modulus E ≈ 551 GPa) (Kulpa & Troczynski 1996). According to Torizuka et al., (1995), TiB_2 has both high wear resistance and high corrosion resistance because of its hardness (H_v, = 2600), high Young's modulus (550 GPa), and high corrosion resistance (it does not react with Al or Zn). Figure 1.10 presents the hexagonal unit cell of single crystal TiB_2.

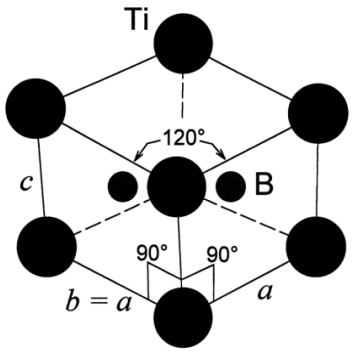

Figure 1.10: The hexagonal unit cell of single crystal TiB_2 (Munro 2000).

It is applied as a temperature-resistant material, especially as a functional component of the aluminium wettable cathodes composite material in the perspective technologies of aluminium production (Blokhina & Ivanov 2014; Ivanov et al. 2014). It has been studied extensively for its potential applications and received great attention because of its high melting point (~ 3200 °C), low density, high hardness, excellent abrasion resistance, elastic

modulus, greater chemical stability, good thermal and electrical conductivity and wettability by molten AI (Demirskyi et al., 2013; Li et al., 2006; Tampieri et al., 1992; Zhao et al., 2014a; Zhao et al., 2014b). The potential applications for TiB_2 are high temperature structural applications such as cutting tools, armour and wear parts (Zhao et al. 2014b). It can also be used as electrodes, high temperature heaters and heat exchangers (Tampieri et al. 1992).

Despite its attractive properties, the application of monolithic TiB_2 ceramic is restricted by its poor sinterability whereby the finer the powder, the more oxygen is carried into the system with the surface oxides (Kulpa & Troczynski 1996), exaggerated grain growth at high temperature and poor oxidation resistance above 1000 °C (Kulpa & Troczynski 1996; Zhao et al. 2014b). At temperatures around 2000 °C, grain growth occurs, instead of densification and, therefore, pressure is required for densification (Torizuka et al. 1995). The densification of pure TiB_2 is difficult due to their strong ionic/covalent bonds, high melting point, low self-diffusion coefficient and the comparatively high vapor pressure of the constituent (Shahedi Asl et al. 2016).

1.3.4 Oxidation of TiB_2

The oxidation of TiB_2 powders is a complicated heterogeneous process and starts at T ≈ 700 K (426.85 °C) (Blokhina & Ivanov 2014). According to Tampieri et al. (1992), TiB_2 ceramic starts to oxidize is about ~ 400 °C, and the oxidation kinetics are being controlled by diffusion up to T = ~ 900 °C. The first stage of the oxidation is either at ~ 1000 °C or ~ 1100 °C (up to 800 min and 500 min, respectively), and by a linear law at higher temperatures and for longer periods. The overall reaction equation of the TiB_2 as shown in the equation (1.3):

$$2TiB_2(s) + 5O(g) \rightarrow 2TiO_2(s) + 2B_2O_3(l) \quad (1.3)$$

ΔH = - 1489 kJ/mol at 700 °C

From 400 °C to 900 °C and at 1000 °C or 1100 °C oxidation of monolithic TiO_2 results in crystalline TiO_2 and B_2O_3. At 700 °C to 900 °C, TiB_2 oxidized into TiO_2 and B_2O_3 in a glassy form or vapor form (above 1000 °C) (Kulpa & Troczynski 1996).

Minor amount of Ti_2O, TiO, Ti_2O_3 and TiBO are also detected. Studies Kulpa et al. (1996) revealed that TiB_2 powders oxidized in low partial pressure oxygen at 10 and 0.05 ppm in

argon at a temperature range of 25 °C to 900 °C exhibited the titanium borate ($TiBO_3$) and B_2O_3 (glass or crystalline phases) are the principal phases.

1.3.5 Silicon Carbide (SiC)

Silicon carbide (SiC) is a non-oxide ceramic which is strong, hard (high hardness) and chemically inert ceramic that normally employs at extreme environments and brittle due to its low fracture toughness (King et al. 2013). The schematic of SiC crystal structure is displayed in Figure 1.11. The most common polytypes includes 3C (β-SiC), 2H, 4H, 6H (α-SiC), and more. There are three basic crystal structures; cubic (C), hexagonal (H) and rhombohedral (R) crystallographic categories. It has exclusive properties such as excellent oxidation resistance, strength retention to high temperatures, high melting point, high wear resistance, high thermal conductivity and good thermal shock. In armour applications, the high hardness of SiC, which is commonly reported to be in the range of 20–27 GPa, is advantageous for projectile defeat i.e. armour systems capable of defeating an incoming projectile on the surface of a ceramic (King et al. 2013).

These SiC properties create a potential material for high power, high temperature electronic devices as well as abrasion, cutting applications (National & Recherche 2008), biomedical applications; bio transducer in biosensors and micro-device fabrication (Oliveros et al. 2013). The main drawback of SiC is the same as ZrB_2, it has extremely low self-diffusion coefficient and brittle due to its low fracture toughness (2–5 MPa $m^{1/2}$) (King et al. 2013; Jan 2014). The densification of SiC powders alone is only possible at extremely high pressure and/or at a temperature exceeding 2100 °C. Sintering aids are necessary to successfully densify SiC (Jan 2014). Nevertheless, the toughness of SiC can be improved up to 6–9 MPa $m^{1/2}$ with additives that promote densification and crack propagation along the grain boundaries as well as increasing the grain size (King et al. 2013).

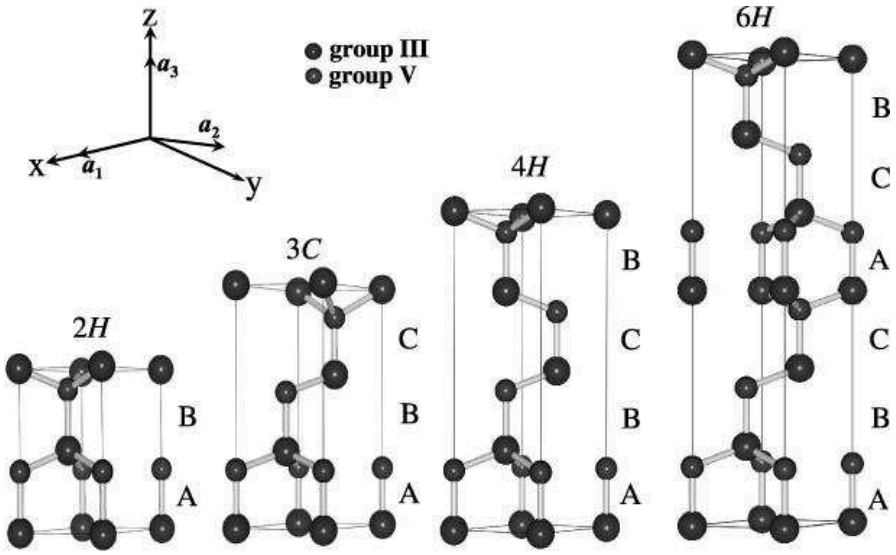

Figure 1.11: Schematic SiC crystal structure (Bechstedt & Belabbes 2013).

1.3.6 Oxidation of SiC

Researchers have reported that by adding SiC to ZrB_2 as presented by reaction equation (1.4), the oxidation resistance of the composite above 1200 °C is improved by the formation of less volatile silica (SiO_2)-rich glass on the exposed surface. The SiO_2-rich layer has been reported to provide passive oxidation resistance to up at least 1500 °C due to the lower volatility of SiO_2 compared with B_2O_3 at these temperatures (Karlsdottir & Halloran 2007).

$$SiC(c) + \frac{3}{2}O_2(g) \rightarrow CO(g) + SiO_2(g) \qquad (1.4)$$

ΔH = - 944 kJ/mol at 700 °C

In keeping up with Hu et al. (2009), the oxidation behaviour of SiC has two types of classifications which are known as active and passive oxidation. The reaction equations (1.5) and (1.6) are shown as below:

$$SiC(c) + O_2(g) \rightarrow CO(g) + SiO(g) \qquad (1.5)$$

ΔH = - 353 kJ/mol at 1200 °C

$$SiC(c) + \frac{1}{2}O_2(g) \rightarrow C(c) + SiO(g) \qquad (1.6)$$

ΔH = - 38 kJ/mol at 1200 °C

The most common route of SiO*(g)* generation is active oxidation. Although this can lead to rapid degradation, it only occurs at low oxygen potentials and high temperatures. The major issue with active oxidation of SiC is the P_{O2} (partial pressure of oxygen) transition point. For reaction equation (1.5), the calculation of the oxygen pressure transition point is complex because two gaseous species are involved. The calculation of active to passive transition for reaction equation (1.6) can be obtained directly based on SiO equilibrium (Hu et al., 2009). The oxygen partial pressure versus temperature for the active to passive oxidation SiC under standard air is shown in Figure 1.12. The details of explanation can be referred at Hu et al. (2009). According to Hu et al. (2009), the SiC oxidation is significantly influenced by the temperature and oxygen partial pressure. The construction of Figure 1.12 were performed using JANAF data (Chase 1998).

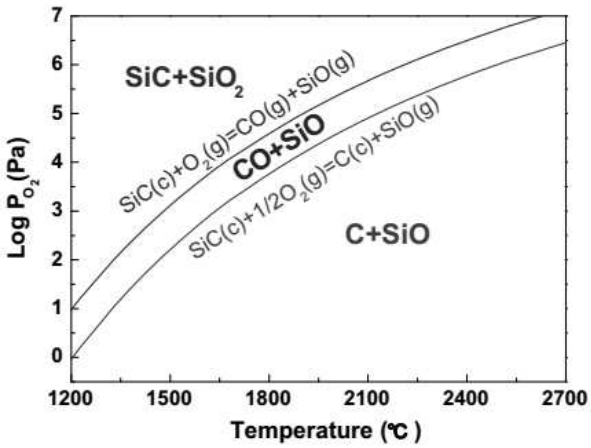

Figure 1.12: Oxygen partial pressure versus temperature for the active to passive oxidation SiC under standard air (Hu et al., 2009).

.

1.3.7 Zirconium Diboride–Silicon Carbide (ZrB_2-SiC) Ceramic Composites

In the recent past, a lot of research have been carried out in the field of ultra-high temperature ceramics (UHTC), especially on ZrB_2 based ceramics and composites. Moreover, several studies have demonstrated that the addition of SiC could improve the oxidation resistance and mechanical properties of ZrB_2 ceramics (Lü et al., 2011; Mashhadi et al., 2015; Yan et al., 2006; Zhang et al., 2009b). At an optimum composition, ZrB_2-SiC ceramic

composites are compatible and well-known to have better strength and oxidation resistance than monolithic ZrB_2.

Several studies of ZrB_2-based ceramics demonstrated that ZrB_2 with 30 vol.% SiC addition exhibited the best combination of strength, fracture toughness (improve mechanical properties), improve oxidation resistance and enhance thermal conductivities (Han et al., 2007; Hu et al., 2009; Kim et al., 2014; Lü et al., 2011; Zhu et al., 2007). It would lead to the excellent combination of mechanical and physicochemical properties. Moreover, SiC could effectively enhance the densification of ZrB_2 probably by reacting with the oxides on ZrB_2 particle surface. The as-sintered ZrB_2–20 vol.% SiC or 20-30 vol.% SiC had improved relative density and mechanical properties at room temperature and high temperatures in order that flexural strength at room temperature exceeds 1000 MPa and fracture toughness achieves values of 5.3 MPa $m^{1/2}$ (Gonzalez-Julian et al. 2014; Lü et al. 2011). Low density of SiC makes it a light-weight alternative for re-entry vehicle applications and components used in the propulsion systems of rockets and satellites. The SiC remained stable up to 2500 °C (Sai Krupa et al. 2013).

The addition of SiC is well-known as the second phase opens up new avenues for the improvement of oxidation resistance (Gonzalez-Julian et al. 2014) by forming a protective borosilicate glass on the surface which can inhibit (hinders/restrain/prevent) the diffusion of oxygen or oxygen penetration into the inner part of the ZrB_2-SiC composites at up to ~1500 °C (Gonzalez-Julian et al., 2014; Li et al., 2013) and which has a higher boiling point, higher viscosity and lower vapor pressure than B_2O_3 (Gao et al. 2013). Further, it acts as a grain growth inhibitor (Snyder et al. 2012). SiC has excellent corrosion resistance properties in severe chemical conditions as well as high wear resistance at room and higher temperatures, especially silicon nitride (Lusquiños et al. 2008).

In conclusion, most of the persuasive features which make ZrB_2 as an excellent combination with SiC are as follows:

a) Its strong covalent bonding and low self-diffusion coefficient, monolithic ZrB_2 is always added to SiC particles to promote the densification, mechanical properties and oxidation resistance (He et al. 2012; Kim et al. 2014).

b) The addition of SiC to ZrB_2-based ceramic provides enhanced mechanical properties and thermal conductivities (Kim et al. 2014).

c) SiC reinforced ZrB_2 composites possess remarkable anti-ablation capability (Hu et al., 2010).

d) The addition of SiC particles into ZrB_2 matrix enhances the fracture toughness of composites from 2-4 $MPa^{1/2}$ which upgrade the use reliability (Hu et al., 2010).

1.3.8 Titanium Diboride-Silicon Carbide (TiB_2-SiC) Ceramic Composites

Like Like other types of ceramics, monolithic TiB_2 has the same drawback which is poor sinterability, exaggerated grain growth at high temperature and poor oxidation resistance (Zhao et al. 2014b). Grain growth occurs at high temperature, instead of densification and therefore, pressure is required for densification. To avoid the grain growth, sintering aid/additive is necessary. Previous research has shown that SiC addition is very effective in improving the sinterability of TiB_2. As presented in the reaction equation (1.3), the overall reaction of TiB_2 and reaction equations (1.4) to (1.6) shows SiC reacts with the TiO_2, that is on the surface of the TiB_2 powder to form an amorphous SiO_2 layer. The amorphous SiO_2 phase is liquid during sintering (Torizuka et al. 1995). The reaction is as shown in the reaction equation (1.7):

$$TiO_2(s) + SiC(s) \rightarrow SiO_2(l) + TiC(s) \qquad (1.7)$$

$$\Delta H = -697 \text{ kJ/mol at } 1200\ ^{\circ}C$$

Generally, SiC is employed to improve the oxidation resistance and mechanical properties of TiB_2. The sinterability of TiB_2, was dramatically improved by the addition of 1.5-5.0 wt.% SiC and it is due to liquid-phase sintering (Torizuka et al. 1995).

Besides that, the increase of SiC content from 10 to 20 wt.%, the fracture toughness increased while the hardness decreased. The composite containing 20 wt.% SiC had the optimum comprehensive mechanical properties with flexural strength of 797 ± 21 MPa, fracture toughness of 6.97 ± 0.5 MPa $m^{1/2}$ and Vickers hardness of 19.47 ± 0.6 GPa (Zhao et al. 2014b).

1.4 Fuel Cells (FCs)

Fuel cells are a favourable solution to environmental challenges due to the effluent gas emission mainly CO_2 that causes global warming. Higher efficiency, cleanliness and cost-effective supply of power are also the reasons they are gaining popularity among other alternative energy sources (Kirubakaran et al. 2009). In fact, they may be better than our current fossil energy conversion system. The reason is that they can be considered as the simplest technology based upon the simple combustion reaction (O'Hayre et al. 2006; Rayment & Sherwin 2003) as given in the reaction equation (1.8):

$$2H_2(g) + O_2(g) \leftrightarrow 2H_2O\ (l) \qquad (1.8)$$

$$\Delta H = -237\ \text{kJ/mol at } 1200\ ^\circ\text{C}$$

A fuel cell is a device that employs hydrogen as fuel to produce electrons, protons, heat and water. Theoretically, it will continue to produce electricity as long as fuel is supplied. As reviewed by Kirubakaran et al. (2009) that the fuel cell is the best combination features of engines and batteries; like an engine they can operate for long, as fuel is available without any intermediate mechanical energy conversion and the characteristics of fuel cells are similar to a battery under load conditions (Kirubakaran et al. 2009; Cook & Heliocentris 2001).

Table 1.4: Comparison of different generation systems (Kirubakaran et al. 2009).

Parameters	Reciprocating engine: diesel	Turbine generator	Photo voltaics	Wind turbine	Fuel cells
Capacity Range	500 kW to 5MW	500 kW to 25 MW	1 kW to 1 MW	10 kW to 1 MW	200 kW to 2 MW
Efficiency	25%	29-42%	6-19%	25%	40-60%
Operation and Maintenance Cost ($/kW)	0.005-0.015	0.005-0.0065	0.001-0.004	0.01	0.0019-0.0153

Table 1.4 shows a comparison of different generation systems, according to Kirubakaran et al. (2009). They observed that the efficiency of fuel cells has been always higher as compared

with conventional systems and other distributed generation systems. While comparing the fuel cell with other distributed generation technologies, it offers more advantages like high energy conversion efficiency, zero emission, modularity, scalability, quick installation and gives good opportunities for cogeneration operations. To understand more, a sub-topic below describes the basic principle of fuel cell operation.

The basic principle of fuel cell involves fuel and oxygen to generate electricity (flow of electrons). The electrons travel around an external circuit delivering electric power. The reaction area is also known as three-phase contact where the reactants, the electrode, and electrolyte meet (Larminie & Dicks 2001). The fuel cell operation involves the reduction of the oxidant (oxygen) at the cathode (positive terminal) and the oxidation of the fuel (hydrogen) at the anode (negative terminal). Thus, if the fuel cell has an oxygen-ion conducting electrolyte, the reactions involve the oxidation and reduction of oxygen at the electrodes. Meanwhile, for the proton-conducting electrolyte, the reactions involve the oxidation and reduction of hydrogen. The difference between oxide-ion (O^{2-}) and proton (H^{+}) conducting is the type of ions passing through the electrolyte either from the cathode to anode or vice-versa (O'Hayre et al. 2006). Electrochemical complete reaction in the electrode for solid oxide fuel cell (SOFC) and polymer electrolyte membrane fuel cell (PEMFC) can be expressed as follows (O'Hayre et al. 2006; Larminie & Dicks 2001; Lonné 2011):

For SOFC:

$$\text{Anode (Hydrogen):} \quad 2H_2 \rightarrow 4H^+ + 4e^- \qquad (1.9)$$

$$\text{Cathode (Oxygen):} \quad O_2 + 4H^+ + 4e^- \rightarrow 2H_2O \qquad (1.10)$$

For PEMFC:

$$\text{Anode (Hydrogen):} \quad 2H_2 + 2O^{2-} \rightarrow 2H_2O + 4e^- \qquad (1.11)$$

$$\text{Cathode (Oxygen):} \quad O_2 + 4e^- \rightarrow 2O^{2-} \qquad (1.12)$$

It is necessary to know the basic structure of electrode and electrolyte since it is where the vital reactions occur. The fuel cell electrodes ought to possess a combination of properties in order to perform better. Among all the properties mentioned here are the significant ones. The electrode material should possess good electrical conductivity, chemical resistance,

corrosion resistance, sufficient mechanical strength, reasonable tolerance to vibration and flexural damage and high reactivity for the electrode reaction (Reed & Brodd 1965). The electrode structure requires porous structure, to resist corrosion and chemically inert and also electronically conducting. It is crucial for gas diffusion. Therefore, a very porous electrode with a spherical microstructure (spherical particles will provide the highest energy densities) is optimal so that penetration by the electrolyte and gas can occur (Rayment & Sherwin 2003).

Meanwhile, for the electrolyte, it is significant since most of the fuel cell is classified by its electrolyte type. The electrolyte type is affecting the characteristic properties of the fuel cell such as operating temperature and mechanism of conductivity. Typically, an electrolyte should be fabricated from solid materials due to practical applications. The most common electrolyte is produced either from polymers or ceramics. Several electrolyte criteria are that it should be dense, leak-tight and good ionic conductivity at the operating temperature. The electrolyte structure should be a thin layer to reduce ionic resistance, thermal shock resistance and economically processable (Singhal et al., 2003). Most of the requirements are not easily compatible. The scientists globally are in the effort of producing the most economical fuel cell in the overall system. Figure 1.13 represents the schematic diagram of the basic principle of a fuel cell for a better view and process understanding on the oxygen-ion/oxide conducting and hydrogen-ion/proton conducting electrolyte.

Fuel cells are mainly classified by the selection of electrolyte and fuel. Further, fuel cells are classified based on the operating temperature. Mostly, electrolyte type determines the kind of chemical reaction, type of catalyst needed, temperature range and fuel type. These characteristics are affecting the suitability of application types. Others can also be differentiated by the materials of construction, the fabrication techniques, and the system requirements. According to Steele and Heinzel (2001), Figure 1.14 summarizes several types of fuel cells under active development. There are as follows:

a) Solid oxide fuel cell (SOFC).
b) Molten carbonate fuel cell (MCFC).
c) Phosphoric acid fuel cell (PAFC).
d) Polymer exchange membrane fuel (PEMFC).
e) Alkaline fuel cell (AFC).

(A)

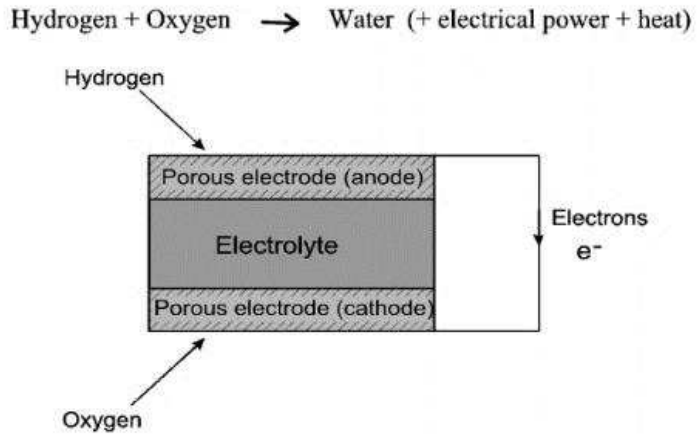

(B)

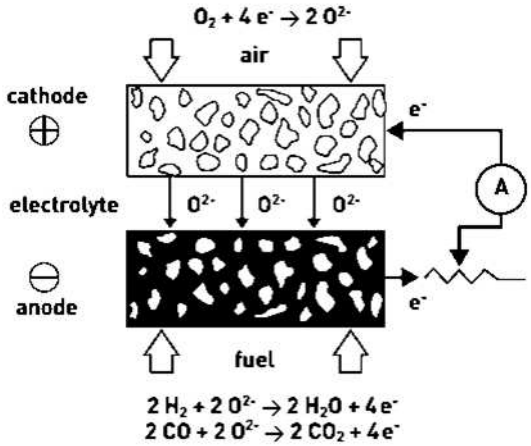

(C)

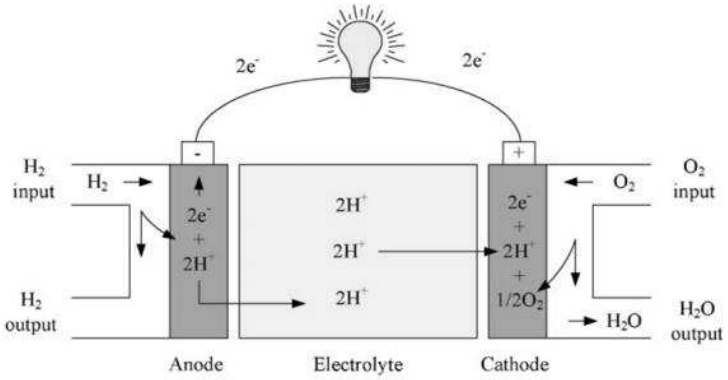

Figure 1.13: Basic principle of the fuel cell. (A) General operating principle of the fuel cell (Ormerod 2003), (B) Oxygen-ion/oxide conducting (CLEFS CEA -No.50/51 2005) and (C) Hydrogen-ion/proton conducting (Andujar & Segura 2009).

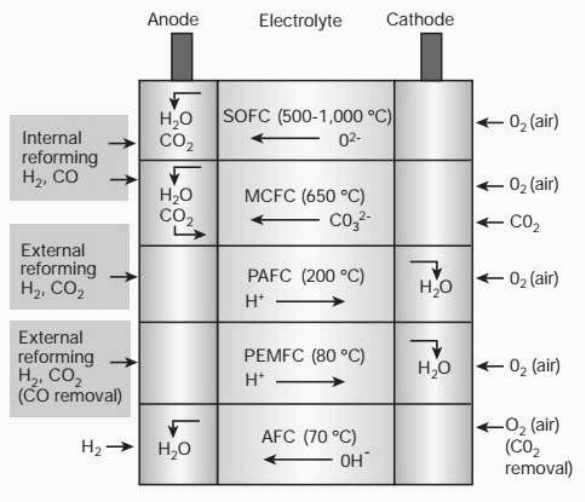

Figure 1.14: Summary of fuel cell types (Steele & Heinzel 2001).

Exclusively, two types of fuel cells are discussed in the next sub-topics. These sub-topics are chosen since they are related to the investigation conducted. They are SOFC and protonic ceramic fuel cell (PCFC). PCFC is still at the early age of research and development.

Fuel cells have a huge potential for power generation in stationary, portable and transport applications and our increasing need for sustainable energy resources (Ormerod 2003). They offer high efficiency and environmental advantages (nearly zero-greenhouse emissions) (Mohamed et al. 2009) which means lower emissions of sulphur and nitrogen oxides and hydrocarbon pollutants and significantly reduced CO_2 emission (Ormerod 2003). In terms of design, they are highly scalable, modular and compact design based on power requirements (Badwal & Foger 1996; Mohamed et al. 2009). There are numerous types of potential fuel sources available; mainly pure hydrogen, natural gas and methanol (fuel flexibility). Furthermore, the fuel cells themselves do not have any moving parts, allowing for quiet and highly reliable operation. In addition, they have nearly instantaneous recharge capability compared to batteries (Mohamed et al. 2009).

A common limitation of all fuel cells is the cost of fuel cell technology (Ormerod 2003; Mohamed et al. 2009; Rayment & Sherwin 2003). It has been an obstacle for worldwide for promoting the widespread fuel cell application. Table 1.5 presents the advantages and disadvantages of fuel cell types.

There are three broad areas of fuel cell applications such as a portable power generation, stationary power generation and power for transportation. The fuel cell applications are primarily influenced by the working temperature (T) of the fuel cells which is governed by the electrolyte. As mentioned by Garche et al. (2015), the electrolyte determines the significant parameters that are mostly dedicated to the ceramic components of high temperature (HT) FCs; firstly, the efficiency η: with increasing T the internal resistivity and polarization is decreased, which overcompensates the T-dependent voltage decrease, followed by the start-up time: time to reach the optimal operating temperature, which increases with increasing T and thirdly is the dynamic behaviour: load changes lead to temperature changes and changes (expansions/contractions) in the stack material, resulting in mechanical stress, which gives rise to a lifetime reduction.

For large stationary applications, it is preferable to have a system with high efficiency; start-up time and load-following dynamics and the SOFC is the preferred FC type. While for mobile and portable applications, the primary parameters are short start-up time (even from temperatures below 0 °C) and high load-following dynamics, and the PEFC or PEMFC is the suitable system.

Table 1.5: Advantages and disadvantages of fuel cell types (Andujar & Segura 2009).

Fuel Cell Types	Advantages	Disadvantages
Solid Oxide Fuel Cell (SOFC)	• Allow spontaneous internal reforming fuel. Because the oxide ions travel through the electrolyte, the fuel cell can be used to oxidize any combustible gas. • Generate a lot of heat. • Chemical reactions are very fast. • High efficiency. • Current densities higher than MCFC. • Solid electrolyte. • No need a noble metal catalyst.	• Not a mature technology. • Moderate intolerance to sulphur (50 ppm).
Molten Carbonate Fuel Cell (MCFC)	• Allow spontaneous internal reforming fuel. • Generate a lot of heat. • High-speed reactions. • High efficiency. • No need for a noble metal catalyst (cost reduction).	• Need to be designed using materials resistant to corrosion and dimensionally stable and resistant. • High intolerance to sulphur. • Liquid electrolyte (handling problems). • Require preheating before starting work.
Alkaline Fuel Cell (AFC)	• Low temperature operation. • A fast start. • High efficiency. • Usage of a very little amount of catalyst, and thereby lowers costs. • Do not have corrosion problems. • A simple operation. • Have low weight and volume.	• Extremely intolerant to CO_2 (up to 350 ppm). • Liquid electrolyte (handling problems). • Require an evacuation of the water treatment complex. • Relatively short lifetime.

Table 1.5 continued.

Polymer Electrolyte Membrane Fuel Cell (PEMFC)	• The cell operates at relatively low temperature; aspects such as handling, assembly or tightness are less complex than in most other types of cells. • Usage of a non-corrosive electrolyte. • Remove the need to handle acid or any other corrosive, increasing security. • Tolerant of CO_2; so they can use the atmospheric air. • Employ a solid and dry electrolyte so it eliminates the handling of liquids and the problems of resupply. • High voltage, current and power density. - They can work at low pressure (1 or 2 bars), which adds security. • A good tolerance to the difference of pressure of the reactants. • Compact and robust and yet have a simple mechanical design. • Stable building materials.	• Sensitive to impurities of hydrogen. • Do not tolerate more than 50 ppm of CO and have a low tolerance to sulphur particles. • Need humidification units of reactive gases. • Usage of catalyst (platinum) and a membrane (solid polymer) very expensive.
Phosphoric Acid Fuel Cell (PAFC)	• Tolerate up to 30% CO_2. • Usage of waste heat for cogeneration. • Usage of an electrolyte with stable characteristics, low volatility even for temperatures above 200°C.	• Have a maximum tolerance of 2% CO. • Utilize liquid electrolyte, which is corrosive to average temperatures, which involves handling and safety problems. • Allow the entry of water that can dilute the acid electrolyte. • Big and heavy. • Cannot auto reform fuel. • Need to reach a certain temperature before starting to work (Slow start-up).

Another parameter is the availability of fuel. From the electrochemical point of view, hydrogen is the best fuel as its direct reaction gives the high power density, but using hydrogen leads to logistic challenges in fuel supply. Therefore, liquid fuels are preferable. Among liquid fuels, methanol reacts directly electrochemically at reasonable rates, however, with a much lower power density than a direct hydrogen FC (< 20% of H2) as reported by Garche et al. (2015). Nonetheless, every FC type has their own various power ranges to support different type of applications. The SOFCs application is considered, ranging from portable devices (e.g., 500 W battery chargers), small power systems (e.g., 5 kW residential power or automobile auxiliary power units) to distributed generation power plants (e.g., 100-500 kW systems). They can also be integrated with a gas turbine to form large (several hundred kW to multi-MW) pressurized hybrid systems. SOFC is the only type that has the potential for such a wide range of applications (Minh 2004).

Meanwhile, for PEMFC, there are three major applications such as transportation, stationary, and portable power generations. Transportation is in the range of 20 to 250 kW. Stationary power is 1-50 MW and portable power is in the range of 5-50 W (Wang et al., 2011). Specifically, the HT-PEMFC application focuses on automotive and stationary power (Lilavivat et al. 2015). Overall, PEMFC is more on transportation (automotive) application due to its potential impact on the environment, unfortunately, the high cost is still challenging for large-scale commercialization (Guerrero Moreno et al. 2015).

Currently, the PCFCs are still new technology. They have not been used to their full potential. The PCFCs application might be similar to SOFCs which is small to the large range; mobile, heavy transport and stationary. Table 1.6 presents the comparison of SOFC, PEMFC and PCFC types for immediate review.

Table 1.6: Comparison of SOFC, PEMFC and PCFC types.

Features	SOFC	PEMFC	PCFC
Operating Temperature	800-1000 °C (Mougin et al. 2009) 600 °C (Duan et al. 2015)	30-100 °C (Guan & Alvfors 2015)	500-700 °C (Frontera et al. 2010) 250 -550 °C (Duan et al. 2015)
Electrolyte	Oxide-ion conducting (O^{2-}) (Frontera et al. 2010; Nasani et al. 2013) • yttria-stabilized zirconia (YSZ) (1st generation). • Samarium-doped ceria (SDC) (2nd generation). • Nanostructured incorporating rare-earth elements (Eu or Ru) (3rd generation) (Duan et al. 2015).	Hydrogen-ion conducting (H^+)/Protonic (Frontera et al. 2010; Nasani et al. 2013) • fluorinated sulfonic acid polymer (Nafion®) (Dayton et al. 2001).	Hydrogen-ion conducting (H^+)/Protonic (Frontera et al. 2010; Nasani et al. 2013) • Ba-based perovskite-structured materials such as $BaZrO_3$ and $BaCeO_3$ doped by selected rare earth elements (Choi et al. 2013).
Electrical Efficiency	45-55% (Coors 2003)	35-45% (Coors 2003)	55-65% (Coors 2003)

Table 1.6 continued.

Main Advantages	• Fuel flexibility. • High efficiency. • Absence of precious-metal catalyst. (Duan et al. 2015).	• Operate at low temperature and high current densities. • Smallest, lightest and most durable tolerant of shock and vibration (Guerrero Moreno et al. 2015).	• Higher fuel conversion efficiency. • Fuel flexibility.(Nasani et al. 2014). • Water formation at the cathode and non-dilution fuel during cell operation. (Nasani et al., 2013a; Nasani et al., 2014b). • An excellent chemical stability against H_2O and CO_2, as well as high bulk proton conductivity (Nasani et al. 2013). • Higher CH_4 conversion (direct proton (hydrogen removal from the anode). • Higher carbon coking resistance (Duan et al. 2015).
Main Challenges	• High costs and material compatibility challenges (Duan et al. 2015). • Presence of water vapor at one of the electrodes lowers the performance. (Gawel et al. 2014). • Main current limitations of SOFCs lie in their reliability and durability, directly linked to the high operating temperature needed to limit ohmic losses across the electrolyte and ranging typically between 800 and 1,000 °C (Mougin et al. 2009).	• Reduced performance at low humidity. • Thermal and water management. • Limited operating temperature. • Large fuel crossover (Loong 2014).	• Presence of water vapor at one of the electrodes lowers the performance (Gawel et al. 2014).

1.4.1 Solid Oxide Fuel Cells (SOFCs)

Solid oxide fuel cells (SOFCs) are also identified as ceramic fuel cell (third generation fuel cell) (Badwal & Foger 1996) due to their material consisting of ceramics which can handle high temperature (>1000 ^{o}C) and therefore facilitate rapid electrode kinetics resulting in the use of no precious materials (Jiang 2012; Richter et al. 2009). It comprises of the cathode and anode as the electrode and an electrolyte. The structure of electrolyte is a dense structure and gas tight (Richter et al. 2009) and the charge carrier in an electrolyte is mostly oxygen species and some of it is used proton-conducting materials.

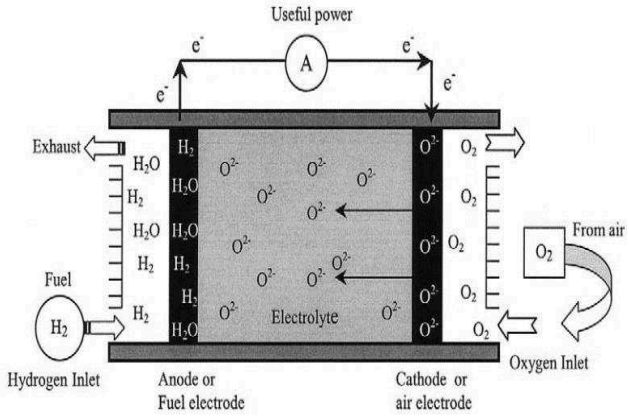

Figure 1.15: Concept diagram of SOFC based on oxygen-ion conductors (Stambouli & Traversa 2002).

The SOFC conceptual diagram for oxide-ion conducting is shown in Figure 1.15 (Stambouli & Traversa 2002). At the cathode (oxidant electrode), the oxygen (O_2) is reduced and become oxygen ions (O^{2-}) when reacted with the electrons from the external load. The oxygen ions are then transported through the electrolyte. At the anode, the fuel is oxidized by the oxygen ions and released electrons (e^-) to the external electrical circuit (Huijsmans, 2001; Wachsman et al., 2011; Zhu et al., 2003). More detail version can be seen in Figure 1.16.

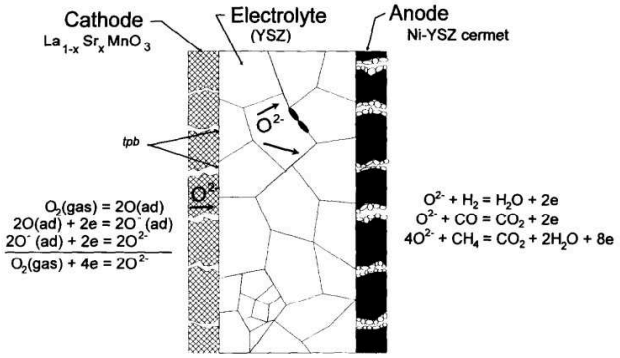

Figure 1.16: Operating principle of SOFC (Badwal & Foger 1996).

Figure 1.16 displays the operating principle diagram of SOFC. It operates at 1000 ^{o}C or below (Huijsmans 2001; Saigal 2007; Shao & Haile 2004; Badwal & Foger 1996). The electrode structure is porous precisely for gas diffusion. The character of the electrode is electronic conducting. The simplified explanation of SOFC process at the cathode, the reduction of oxygen occurs and passes through the electrolyte membrane via a vacancy mechanism to the anode. At the anode, oxidation of hydrogen occurs from the directed reformed natural gas or other hydrocarbons (Huijsmans 2001). It is well-known as an electrochemical device that generates clean, highly-efficient power on site from a wide range of fuel sources. It can be powered by using hydrogen and combustible fuel, including natural gas, liquid hydrocarbons and even solid derived from coal or biomass (Gorte & Vohs 2009). Conventional SOFC is composed of yttria-stabilized zirconia (YSZ) as an electrolyte which requires an operating temperature of over 800 °C.

An established high-temperature SOFC (HT-SOFC) offers a clean, pollution-free technology to electrochemically generate electricity at high efficiencies and with lower emissions than conventional power generation technologies (Li et al., 2012; Singhal, 2000). However, recent research progress in reducing operating temperature would benefit the system. Reduction of operating temperature below 800 ^{o}C will significantly extend the lifetime, provide flexibility in materials selection, and reduce the cost (Zhi et al. 2012; Souza et al. 1997).

Several types of SOFCs have been identified and classified into three types according to its operating temperature: Low temperature, intermediate temperature, and high temperature SOFC. Basically, the HT-SOFC operates at 600 to 1000 ^{o}C (Richter et al. 2009; Jiang 2012). Some of the researchers indicate that high temperature is in the range of 700-950 °C (CLEFS CEA -No.50/51 2005). It can be fuelled up with hydrogen, natural gas and hydrocarbons. At

this high temperature, it would benefit the CO and H_2 since it can be electrochemically oxidized at the anode to improve the system efficiencies.

At a high operating temperature (~1000 ^oC), SOFC benefits the system in such as no need for the expensive external reformer. Moreover, natural gas fuel can be reformed within the cell stack (Singhal, 2000) and this is an agreement with Steele and Heinzel (2001). According to Steel and Heinzel (2001), the fuel-processing reaction can be accomplished within the stack, thus enables innovative thermal integration/management design features to provide excellent system efficiencies. It has also been confirmed by the successful operation in several atmospheric pressure power generation systems of up to 100 kW in size. In addition, it removes the need for a precious-metal catalyst, thereby reducing cost and allowing for reforming fuels internally, which enables the use of a variety of fuels and reduces the cost associated with adding a reformer to the system. Atmospheric and pressurized SOFC based power systems are ideal distributed power generation systems-reliable, clean, quiet, environmentally friendly and fuel conserving (Singhal, 2000). Despite the HT-SOFC, combined advantages environmentally friendly with fuel flexibility, however constrain the materials selection and overall system cost.

The intermediate temperature of SOFC (IT-SOFC) is in the range of 500 to 700 ^oC (Sahibzada et al. 2000; Shao & Haile 2004). However, Richter et al. (2009) claimed that the intermediate temperature is between 600 to 800 ^oC. Jiang (2012) has reviewed that the range of intermediate temperature is 500 to 800 ^oC in proportional with Zhou et al. (2009). It is concluded that the intermediate temperature is in the range of 500 to 800 °C. $Ba_{0.5}Sr_{0.5}Co_{0.8}Fe_{0.2}O_{3-\delta}$ (BSCF) is one of the materials that has been chosen as a cathode in operating intermediate-temperature (500-700 ^oC) of SOFCs (Shao & Haile 2004). This material is selected due to its good oxygen surface exchange and diffusion properties (Richter et al. 2009) as well enables the system conducted in reduced temperature. It is believed that this high-performance cathode is employed to tackle the obstacle at the reduced temperature operation which conventional cathode material lack of the electrochemical reduction of oxygen.

The low temperature of SOFC (LT-SOFC) operates at less than 600 ^oC (Richter et al. 2009). In this condition, the potential for ohmic losses increases in the electrolyte and polarization losses increases in the electrolyte/cathode interface (Huijsmans 2001). Fabrication of LT-

SOFC with ultra-thin film yttria-stabilized zirconia (YSZ) electrolytes, the optimal SOFC operating temperature is approximately 300 °C since this is the temperature at which the anode and cathode can perform catalytic activity and metal can also be used for other components of the fuel cell since they will no longer melt (Saigal 2007).

1.4.1.1 SOFC Materials

This section discusses the SOFC components such as anode, cathode and electrolyte materials and their characteristics. However, interconnects and sealing are not discussed. As reviewed by Badwal and Foger (1996), general requirements for SOFC cell components are as below:

a) Chemical stability in fuel cell environments ($p(O_2) > 20$ kPa on the cathode side and $< 10^{-17}$ atm on the anode side) and compatibility with other cell components.
b) Phase and microstructural stability.
c) Minimum thermal expansion mismatch between various cell components (laminated structure).
d) For structural components, reasonable strength and toughness at the cell operating temperature, as well as reasonable thermal shock resistance.
e) Low vapor pressure to avoid loss of the material.
f) Must allow cost competitive component fabrication.

1.4.1.2 Cathode Materials

The cathode is where the electrochemical reduction of oxygen occurs and below are the characteristics of the cathode (Taroco et al. 2011).

a) Adequate porosity (approximately 30-40%) to allow oxygen diffusion.
b) Chemical compatibility with the other contacting components (usually the electrolyte and interconnect) under operating conditions.
c) A thermal expansion coefficient (TEC) matching those of the components.
d) Chemical and microstructure stability under an oxidizing atmosphere during fabrication and operation.
e) Low cost and relatively simple fabrication procedure.
f) High catalytic activity for the oxygen reduction reaction.

g) Large triple phase boundary (TPB).

h) Adhesion to electrolyte surface.

1) High electronic and ionic conductivity.

Figure 1.17 represents triple-phase boundaries (TPB). At these boundaries, it is believed that the occurrence of electrochemical reactions. The TPBs which are the sites where the oxygen ion conductor, electronic conductor, and the gas phase are in contact.

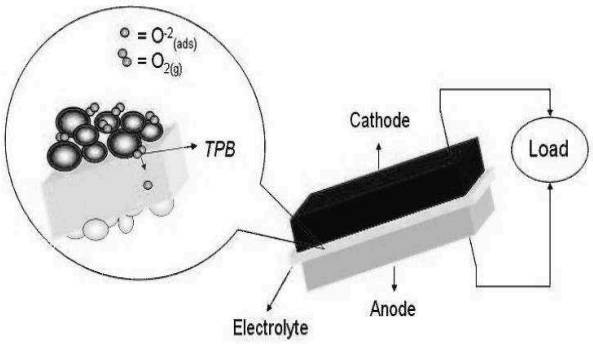

Figure 1.17: Triple-phase boundaries (TPB) (Taroco et al. 2011).

Currently, the perovskite material of the ABO_3 is normally employed as the cathode materials. Lanthanum manganite ($LaMnO_3$) with substitutions of strontium or calcium at the A-site is frequently employed (Badwal & Foger 1996; Minh 2004; Menzler et al. 2010; Huijsmans 2001; Jeffrey W. Fergus 2006; Ralph et al. 2001). This material is selected due to its stability in an oxidizing atmosphere. In addition, it has sufficient electrical conductivity and closer thermal expansion match to the YSZ electrolyte (Ralph et al. 2001). At the lower operating temperature, the cathode has encountered the polarization losses issue. To tackle, this issue, incorporation of electrolyte material has been employed without performance loss. The electrolyte material will be forming oxygen conducting for oxygen ions between the LSM cathode materials. Huijsmans (2001) has determined that an optimum thickness of this structure has to be around 15 µm to ensure that the transfer of oxygen charge carriers into the electrolyte. This thickness is only applied in the porous zirconia network.

The cathode structure is a porous structure for gas distribution as well as good electronic conductivity for electron transport to the electrochemically active cathode structure. Overall the cathode structure is a two-layer or duplex structure (Huijsmans 2001). The obstacle that occurs in the cathode material during the fuel cell operation is the oxygen diffusion due to

the creation of oxygen defect sites by the overpotential. It can be overcome by combining the cathode and electrolyte material in the vicinity of the electrolyte layer (Menzler et al. 2010).

Another alternative is by using mixed ionic electronic conducting (MIEC) cathode materials (Menzler et al. 2010; Huijsmans 2001). According to Menzler et al. (2010), the benefit of employing this MIEC is the reactive catalytic surface area over the whole perovskite grain would be increased. Hence, the charge transfer of adsorbed oxygen atoms could take place directly on the perovskite surface.

Furthermore, an effort by tailoring the microstructure and highly electrocatalytic materials such as $La_{1-x}Sr_xMnO_{3-\delta}$ (LSM) and $La_{1-x}Sr_xFe_{1-y}Co_yO_{3-\delta}$ (LSCF) with the perovskite (ABO_3) crystal structures has been conducted to increase the triple phase boundary density. LSCF perovskite material is considered as an alternative material with high ionic conductivity to be employed on the ceria or zirconia electrolytes. However, the drawback is the formation of reaction products between LSFC material and zirconia in direct used will cause deleterious conductivity characteristics. It can be resolved by the introduction of thin layer ceria between the zirconia and the LSCF cathodes (Huijsmans 2001). LSM is high thermal and chemically stable and reasonable catalytic activity for oxygen reduction in high temperature. Unfortunately, it cannot be employed at a lower temperature due to negligible bulk ionic conduction and high activation energy; the electrochemical reaction sites are restricted to the electrolyte/cathode interface. The solution to this is by adding an ionic conductor such as stabilized zirconia and doped ceria (Lee et al., 2012).

Yano et al. (2007) have concluded that $Sm_{0.5}Sr_{0.5}CoO_3$ (SSC) cathode can also be considered as an alternative material since it can be an inert catalyst for ethane oxidation at 500 °C (Yano et al. 2007). Shao et al. (2004) have produced a new cathode material $Ba_{0.5}Sr_{0.5}Co_{0.8}Fe_{0.2}O_{3-\delta}$ (BSCF) with low area specific resistances (ASRs) of 0.06 and 0.55 Ωcm^2 at 600 and 500 °C, respectively. BSCF is incorporated with thin-film doped ceria exhibited the high-power densities. It is suitable for dual or single chamber for configurations at lower temperature ~600 °C.

A pyrochlore structured bismuth ruthenate ($Bi_2Ru_2O_7$, BRO7) material also has been investigated. Ruthenium oxide is known for its highly catalytic activity. Lee et al. (1997) reported that using an A-site dopant with sufficiently large ionic radius, such as Bi or Pb,

ruthenium pyrochlores ($A_2Ru_2O_7$) become metallic due to the altered energy band structure by increasing the Ru–O–Ru bond angle. According to Lee et al. (2012) when using these materials with Bi as the A-site dopant, high electronic conduction is expected at low temperatures. BRO7 is proven compatible with both doped ceria and stabilized bismuth oxide and showed reasonably high performance at lower temperatures.

The latest development of National Research Council Canada Institute for Fuel Cell Innovation (NRC-IFCI) has developed cathode materials with new compositions (patent pending) for SOFCs operating at reduced temperatures. The new cathode material is as an oxygen reduction catalyst for the low temperature of SOFCs and it can be mass-produced. It allows for a significant reduction in fuel cell polarization at operating temperatures at range 450 to 600 °C while improving the performance, reliability and cost efficiency of the entire system (Canada 2011).

1.4.1.3 Anode Materials

The anode provides reaction sites for the electrochemical oxidation of the fuel gas. An adequate anode has to meet the requirement as shown below (Taroco et al. 2011; Jeffrey W Fergus 2006).

a) High electrical conductivity.
b) A thermal expansion coefficient (TEC) that matches those of the adjoining components.
c) The capacity of avoiding coke deposition.
d) Fine particle size (µm).
e) Chemical compatibility with another cell component (electrolyte and interconnector) under a reducing atmosphere at the operating temperature.
f) Large triple phase boundary (TPB).
g) High electrochemical or catalytic activity for the oxidation of the selected fuel gas.
h) High porosity (20-40%) adequate for the fuel supply and the reaction product removal.
i) Good electronic and ionic conductive phases.
j) Compatible with the electrolyte (chemical and thermal expansion).

The most common anode material employed in the conventional SOFCs is Ni/YSZ cermet (Nickel/yttria-stabilized zirconia) (Badwal et al., 1996; Huijsmans, 2001; Menzler et al., 2010; Minh, 2004; Zhu et al., 2003). It is selected due to its low cost and chemically stable in reducing atmosphere at high temperatures. Moreover, its thermal expansion coefficient is close to that of YSZ-electrolyte (Jiang, 2012; Zhu et al., 2003). The anode structure is a duplex structure or bi-layer system (Huijsmans 2001). The anode porous structure functions as providing the electrochemical reaction sites for fuel oxidation, which allows the fuel and by-products to be moved out from the surface sites and forming the electron path to be transported to the interconnect. Therefore, the anode must be an electronic conductor. Interconnect is a component to connect the anode to cathode so that voltage output can be enhanced for practical application (Zhu et al., 2003).

Recently, the researchers are more focused on the anode substrates compared to the anode itself. This is because of good electrical conductivity and gas permeability and fine-grained homogeneous microstructure features. It is also considered as the most promising candidate for material savings (Menzler et al. 2010). Another effort to improve anode is by applying nanoscale engineering structure. The nanostructured anode approach is to maximize the number of sites where the electrochemical reactions take place (Gorte & Vohs 2009). The mixed ionic and electron conducting (MIEC) for anode materials also positively extends the active zones that electrochemical reactions can occur by allowing O^{2-} ions to any position of interfaces between the anode and gas phase (Sun et al., 2007).

Ni/YSZ cermet is an anode material which has been classically known for its high electronic conductivity. The main purpose of oxide component is to reduce the sintering of the Ni metal phase, to decrease the thermal expansion coefficient and improve the electrochemical anode performance. YSZ phase in the cermet plays a significant role in the creation of addition reaction sites by extension of triple phase boundary (TPB). However, Ni-based anodes have very low tolerance toward the sulphur poisoning (Jiang, 2012; Sun et al., 2007), poor redox stability and carbon deposition when employed with hydrocarbon fuels and tendency of Ni agglomeration after prolonged operation (Sun et al., 2007). In order to avoid the carbon deposition, the operating temperature needs to be reduced or excess steam is present. Ni is an excellent catalyst for steam reforming and hydrogen cracking (Sun et al., 2007).

Composite material Cu-CeO_2-YSZ/SDC is another type of anode material. It allows the direct electrochemical oxidation of methane (Zhu et al., 2003). Sun et al. (2007) have reviewed that Cu-CeO_2-YSZ has high sulphur tolerance at the lower temperature using hydrogen fuel. Cu is effective as a current collector (Sun et al., 2007). Both doped and undoped ceria are MIEC at low oxygen partial pressure (Zhu et al., 2003). The ceria provides a high catalytic activity for hydrocarbon reforming due to its oxygen storage and transport properties (Sun et al., 2007). Ceria-based anodes have greater coking resistance and sulphur tolerance than zirconia-based anodes. This is due to the greater ionic conductivity and more facile $Ce^{3+/4+}$ redox behaviours. However, the disadvantage of ceria is the degradation of mechanical integrity due to the lattice expansion in the low oxygen partial pressure environment arising from the transition of Ce^{4+} to Ce^{3+} (Menzler et al., 2010; Zhu et al., 2003). Ni/CGO as a composite anode can also be employed at the temperature of 500 °C as it has shown an acceptable performance for simulated syngas fuels (Steele & Heinzel 2001). Ni acts as both the catalyst and electronic conducting phase, while gadolinia-doped ceria acts as a matrix to support the catalyst and prohibit the metal from agglomeration under operating condition (Zha et al. 2004). The composite Ni/Ce structures for the anode is also considered (Huijsmans 2001). Nickel/$Ce_{0.8}Sm_{0.2}O_{1.9}$ (Ni/SDC) has been investigated and appeared as an effective catalyst for the partial oxidation of ethane by oxygen at 500 °C (Yano et al. 2007). Besides that, the tri-metal alloy has also been studied such as $Fe_xCo_{0.5-x}Ni_{0.5}/Sm_{0.2}Ce_{0.8}O_{1.9}$ (SDC) cermet. This material shows the lowest interfacial resistance and highest power density (Sun et al., 2007). SDC has exhibited 2-3 times higher conductivity compared to YSZ. However, this material can cause an internal electrical shorting which then decreases the power output. This drawback contributed by the reduction of Ce^{4+} to Ce^{3+} which cause the electronic conduction (Yang et al., 2007).

Wachsman et al. (2011) have integrated the general method into anode-supported cell composed of a thin, dense GDC (`~ 10 µm)/ESB (~ 4 µm) bi-layered electrolyte with a newly developed high-performance bismuth ruthenate-bismuth oxide (BRO7-ESB) composite electrode. It demonstrated better high-power density compared to a single (~ 10 µm) layer GDC electrolyte. According to Lee et al. (2012), the anode substrates/supports should possess as large pore microstructure to accommodate rapid gas transport, both fuel in and reaction by-products, such as water, out. Secondly, it should have a high surface area triple phase boundary region to maximize anodic reactions.

The research indicates that particle size and distribution together with the sintering temperature of the anode influence in determining the anode performance (Huijsmans 2001; Jiang 2012). Alternative materials with high ionic and electronic conductivity are also considered in the absence of nickel (Huijsmans 2001; Steele & Heinzel 2001). Even though the anode materials have least research improvement on the overall system compared to cathode and electrolyte studies, the existing anode materials still should be further improved or finding an alternative material for anode should be continued as an option to extend the anode materials for specific operating temperature.

1.4.1.4 Electrolyte Materials

The electrolyte is the component of the cell responsible for conducting ions between the electrodes, for the separation of the reacting gases and for the internal electronic conduction blocking, forcing the electrons to flow through the external circuit. Without significant ion conduction, no current would pass through the cell and only a potential difference would be detected.

There are three types of electrolytes that differ by the ion transport mechanism: anionic, protonic and mixed ionic. However, most of the high temperature fuel cells operate via oxygen ion (O^{2-}) conduction from the air electrode to the fuel electrode. This conduction occurs because of the presence of oxygen ions vacancies, so the crystallites forming the electrolyte must have unoccupied anionic sites. The energy required for the oxide ion migration from one site to the neighbouring unoccupied equivalent site must be smaller (Faro et al., 2009). Its ionic conductivity and thickness, determine the operating temperature range of the SOFC (Taroco et al. 2011). Fergus (2006) has mentioned that the key requirement for the solid electrolyte is that it has good ionic conduction to minimize cell impedance, but also has little or no electronic conduction to minimize leakage currents, so control of the concentration and mobility of ionic and electronic charge carriers is critical.

As shown below listed several criteria of an optimum electrolyte operation and in parallel or added with other researchers (Fergus, 2006a; Singhal et al., 2003; Taroco et al., 2011).

a) It must be dense and leak-tight.
b) Optimum composition to give good ionic conduction at the operating temperatures (Oxide ion conductivity greater than 10^{-2} Scm^{-1}).
c) Negligible electronic conduction (An electronic transport number close to zero).
d) High-density to promote gas impermeability.
e) A thin layer to reduce the ionic resistance (less than 30 μm).
f) Extended in an area to maximize the current capacity.
g) Thermal shock resistance (suitable mechanical properties, with fracture resistance greater than 400 MPa at room temperature).
h) Thermodynamic stability over a wide range of temperature and oxygen partial pressure.
i) Thermal expansion coefficient (TEC) compatible with that of the electrodes and other cell materials from ambient temperature to cell operating temperature.
j) Negligible chemical interaction with electrode materials under operation and fabrication conditions (avoid the formation of blocking interface phases).
k) Chemically and mechanically compatible with other fuel cell components.
l) Economically processable (low cost of starting materials and fabrication).

For a better compilation of SOFC specification, Table 1.7 displays a compact view of significant specification for SOFC by Mougin et al. (2009).

In conclusion, the development of SOFCs is urgently focusing on lowering the operating temperature as much as possible. The effort to enhance the performance of electrolyte by reducing the electrolyte thickness is still considered to be an option for low temperature SOFCs. In the electrode development, the mixed ionic and electronic conduction structures are still reliable for lower operating temperature. The cathode material with the combining of electrolyte material and higher ionic conducting structures can be further studied at the lower temperature. As for the anode material, the reliability of direct used for hydrocarbons fuels can be further studied as well. Various efforts currently have been invested in low temperature SOFCs especially on the materials development.

Table 1.7: Main specification of SOFC constituting materials (Mougin et al. 2009).

Parameter	Anode	Electrolyte	Cathode
Material requirements	Chemical stability under reducing (p_{O2} ~ 10^{-18} Atm).	Chemical stability under high p_{O2} gradient (10^{-18} Atm to 1 Atm).	Chemical stability under oxidizing atm. (p_{O2} ~1 Atm).
Density	Porous (20 – 40%) Preferably with the gradient.	Dense (> 95%).	Porous (20 – 40%) Preferably with the gradient.
Ionic conductivity	Delocalised the electrochemical reaction.	Highest (YSZ: 10^{-1} S cm^{-1} at 1,000 °C, 10^{-2} S cm^{-1} at 750 °C).	Delocalised the electrochemical reaction.
Electronic conductivity	Highest (Ni-Cermet 10^{3} S cm^{-1}at 800–900 °C).	Negligible compared to ionic conductivity	Highest (LSM ~10^{2} S cm^{-1} at 800–900 °C).

The lab-scale technology should demonstrate its reliability and achieve the cost reduction at the field test and latter penetrate to the larger scale technology. The future work can also be divided into two levels which are the industrial level and research and development at the universities and institutes. The industries can focus on the reduction of materials and manufacture costs and the assembly of stacks. Meanwhile, the universities or institutes can focus on the understanding of degradation mechanisms, lifetime modelling and the development of novel materials. Even more, field tests have been already carried out yet still much more testing is necessary

1.4.1.5 SOFC Challenges and Efforts

Numerous efforts of research works have been done and underway for the development of novel types of ceramic electrolytes, anode, and cathode materials. The main reasons are to achieve lower operating temperatures and enable internal fuel in the system. Such investigations go hand in hand with the development and optimization of material fabrication and forming processes with the aim of bringing down manufacturing costs (CLEFS CEA -No.50/51 2005).

Since the major advantage of SOFCs over PEMFCs is their superior tolerance to impurities in the fuel, which allows for their operation using lower quality, thus less costly and more widely available, fuel (Jeffrey W. Fergus 2006). Various attempts have been sought to compensate the drawbacks.

Works done by Fergus (2006) concludes that the two most widely used alternatives to YSZ as electrolytes in IT-SOFCs are doped ceria and doped lanthanum gallate. Ceria has the highest conductivity and the best stability with cathode materials but suffers from stability in low oxygen partial pressures. The perovskite, $LaGaO_3$, can be doped with strontium and magnesium, $La_{1-x}Sr_xGa_{1-y}Mg_yO_3$ (LSGM), LSGM has higher conductivity than YSZ, but is less stable with the anode and more difficult to prepare than YSZ.

Fuel cell designs with layered structures can combine the advantages of the different materials, but simple structures are preferred to reduce cost and improve reliability. The required conductivity depends on the fuel cell design (e.g. electrolyte-supported versus anode supported), and compatibility (chemical and mechanical) depends on the materials used for other components, so these factors, must be considered in the selection of the optimal electrolyte material for a particular application (Jeffrey W. Fergus 2006).

The condition of SOFCs also must operate at ~ 800 °C to avoid unacceptably high polarization losses (Wachsman et al., 2009). Overall, it demonstrates that the efforts of overcoming the drawbacks are affecting the overall components of SOFC systems.

1.4.2 Protonic Ceramic Fuel Cells (PCFCs)

A new type of fuel cell has been investigated and lab-scale developed that comprised of both interesting features adopted from SOFC and PEMFC types. Mainly operates at an elevated temperature and exhibits high protonic conductivity. It is known as protonic ceramic fuel cells (PCFCs). They are based on a proton conducting oxide electrolyte and allow the significant decrease in operating temperature (Mougin et al. 2009).

The lower activation energy associated with proton conduction in oxides that makes them able to operate at lower temperatures than SOFC (Duan et al. 2015). PCFC believes to offer maximum theoretical electrical efficiency over SOFCs due to the formation of water at cathode hence the fuel does not become diluted during the operation (Nasani et al. 2015). The main benefit of PCFC is high fuel utilization that operates at high temperature and achieves 55-65% electrical efficiency (Coors 2003).

ZrB_2-SiC ceramic electrodes coated with a proton conducting SiO_2-rich glass layer has been developed for the future use of hydrogen or direct alcohol fuel cells and it is an example of

an ultra-high temperature ceramics (Lonné et al. 2011) and potential to be conducted as PCFC type.

Even so, there are still weaknesses can be found in PCFC such as lack of suitable cathodes and fabrication challenges stemming from the refractory nature of most PCFC electrolytes (Duan et al. 2015). Furthermore, they require long start-up times and bigger in size. In conclusion, these fuel cells working at high temperature are more efficient and fuel-flexibility (Frontera et al. 2010) compared to those working at low or intermediate temperature.

The main advantage of PCFC is their high ionic conductivity at intermediate temperature (Mougin et al. 2009). When a protonic conductor is used for SOFC instead of oxide-ionic conductor, fuel circulation is unnecessary in the case of hydrogen fuel cell because no water molecules are generated at the fuel electrode (Iwahara et al. 2004). They are targeted for operation at 55–65% electrical efficiency on pipeline natural gas. This can only be achieved with greater than 90% direct methane fuel utilization. Such high fuel utilization is made possible by three factors.

First, the high thermo-chemical efficiency of reforming and water shift reactions at the anode is possible at the high operating temperatures of 700–750 °C. Second, water vapor is produced at the cathode, where it is subsequently swept away by the air flow, rather than at the anode, where it would dilute the fuel (carbon dioxide is the only anode exhaust gas). Third, ambipolar steam permeation through the electrolyte provides the steam required for the reforming and shift reactions, thus preventing hydrocarbon coking and obviating the need for external steam injection (Coors 2003).

1.4.2.1 PCFC Materials

Before reviewing possible protonic devices, proton-conducting ceramics usable at elevated temperatures are briefly described. A typical proton-conducting ceramic $SrCe_{0.95}Yb_{0.05}O_3$ a is a solid solution based on the perovskite-type oxide $SrCeO_3$, in which 5% of Ce is replaced by Yb. Other perovskite-type oxides based on strontium cerate ($SrCeO_3$) or barium cerium(IV) oxide ($BaCeO_3$), in which some trivalent cations are partially substituted for cerium, are also protonic conductors. The general formula is written as $SrCe_{1-x}M_xO_{3a}$ or $BaCe_{1-x}M_xO_3$ a where M is some rare-earth element, x is less than its upper limit of solid solution formation range (usually less than 0.2) and a is the oxygen deficiency per unit formula.

The ceramics of these perovskite-type oxide solid solutions exhibit p-type electronic (hole) conduction under oxidizing atmosphere free from hydrogen or water vapour at high temperature. However, when they are exposed to hydrogen-containing atmosphere at elevated temperatures, the electronic conductivity decreases, and protonic conduction appears. Their conductivities in the hydrogen atmosphere are of the order of 10^2 to 10^3 S cm^1 at 600 °C to 1000 °C operating temperature.

The protonic conduction in these oxides has been verified by electrochemical hydrogen transport experiments under hydrogen- or water-vapor-containing atmosphere at elevated temperatures. After the discovery of $SrCeO_3$-based protonic conductors, $KTaO_3$-based oxide and Y_2O_3 ceramics were reported to have protonic conduction at high temperature, although the conductivities were not as high as those of the cerate-based perovskite-type oxide ceramics.

Some doped zirconates based on $CaZrO_3$, $SrZrO_3$ or $BaZrO_3$ were also confirmed to exhibit the same behaviour as the above cerates although their conductivities were about one order of magnitude lower than those of the cerates. A series of complex perovskites based on $Ba_3(CaNb_2)O_9$ or $Sr_2(ScNb)O_6$ were reported to exhibit the protonic conductivity as high as that of $BaCeO_3$-based ceramics. Among the oxides described above, $BaCeO_3$-based ceramics show the highest conductivity.

However, the contribution of oxide ions to the conduction grows markedly as the temperature is raised. Although the conductivity of $SrCeO_3$-based ceramic is rather low, the transport number of protons is higher than that of the $BaCeO_3$-based ones. The conductivity of zirconate-based ceramics is lower than that of the cerates, but they are superior with respect to their chemical and mechanical strength.

In contrast to cerates, zirconates hardly react with an acid solution, and they are stable against carbon dioxide gas, which reacts easily with cerate ceramics below 800 °C to form carbonates. Several kinds of non-perovskite-type oxides or salts have become known to exhibit protonic conduction at elevated temperatures, although their protonic conductivities are rather low compared to those of the above-mentioned perovskite-type oxides. Examples comprise $Ln_2Zr_2O_7$ and $LaPO_4$ systems. It was reported that even an alumina ceramic showed pure and stable protonic conduction at high temperature although the conductivity is very

low (Iwahara et al. 2004). Ni anode is found to be the most efficient metallic anode even though it is sensitive to pH_2 decrease (Mougin et al. 2009).

1.4.2.2 PCFC Design, Challenges and Overcomes

In consideration of PCFC technology is still new, it is most likely to have PEMFC design. Several challenges must be overcome before PCFC could be a competitive alternative for the users. The PCFC technology is remained in a laboratory scale due to the various challenges. At the present, this section discusses a part of them.

This is the most common drawbacks. Most conventional proton conducting solid electrolytes is unstable at elevated temperatures higher than 300 °C since they are dehydrated leading to a decrease in conductivity. Therefore, researchers have found perovskite-type oxide solid solution ceramics based on $SrCeO_3$ to resolve the instability at high temperature (Iwahara 1995).

Mougin et al. (2009) identified the same major issues; (i) the stability of proton conducting oxide materials, in particular regarding reducing environments and CO_2, to obtain acceptable durability and (ii) electrode stability and their interfaces with the electrolyte to further increase performance (Mougin et al. 2009).

As reported by Duan et al. (2015) that is in agreement with Kreuer studies an important step toward enabling viable PCFCs with the demonstration of stable yttrium-doped barium zirconate (BZY) proton conductors with high (bulk) proton conductivity. Despite this advance, the high grain boundary resistance and fabrication challenges associated with this refractory material system have, until now, constrained its application. Nevertheless, the intrinsic conductivities of currently available protonic ceramic electrolytes suggest that PCFCs can eventually deliver excellent performance between 250 °C and 550 °C (Duan et al. 2015; Kreuer 1997).

Even though, there are many efforts have been taken rigorously and little progress achieved. Researchers still think that PCFC is an opportunity to compensate both SOFC and PEMFC fuel cells drawbacks and more alternative towards achieving environmentally friendly energy.

CHAPTER 2

Research Methodology

This chapter details out the research methods applied in the present work. It explains the framework of research methods to prepare the sintered ceramic composite samples followed by the laser irradiation approach with the aim of producing proton conducting samples. Three main laboratory characterization techniques were performed for chemical and surface analysis, structure observation and crystalline material structure. Also, this chapter describes the research tool used and how the information gathered is transcribed and analysed.

2.1 Research Design and Procedures

Figure 2.1 shows the research methodology flow diagram. It is divided into three major stages. The first stage involved the preparation of materials and fabrication of samples in pellet form and sintering process at the desirable temperature. The preliminary characterizations and analysis were performed to observe the sintered pellet structure. The characterizations were necessary to ensure the densification took place and achieve the desired pellet density.

The next stage involves the critical laser scanning design before proceeding with the oxidation process. The scanning pattern was designed and configured thoroughly. After being satisfied with the laser design, the oxidation process was performed. The characterizations were employed to confirm the presence of glassy layer and to analyse the structure. At every stage of research, the characterizations were employed, and the results were analysed. Finally, the results were interpreted, discussed, concluded, and reported.

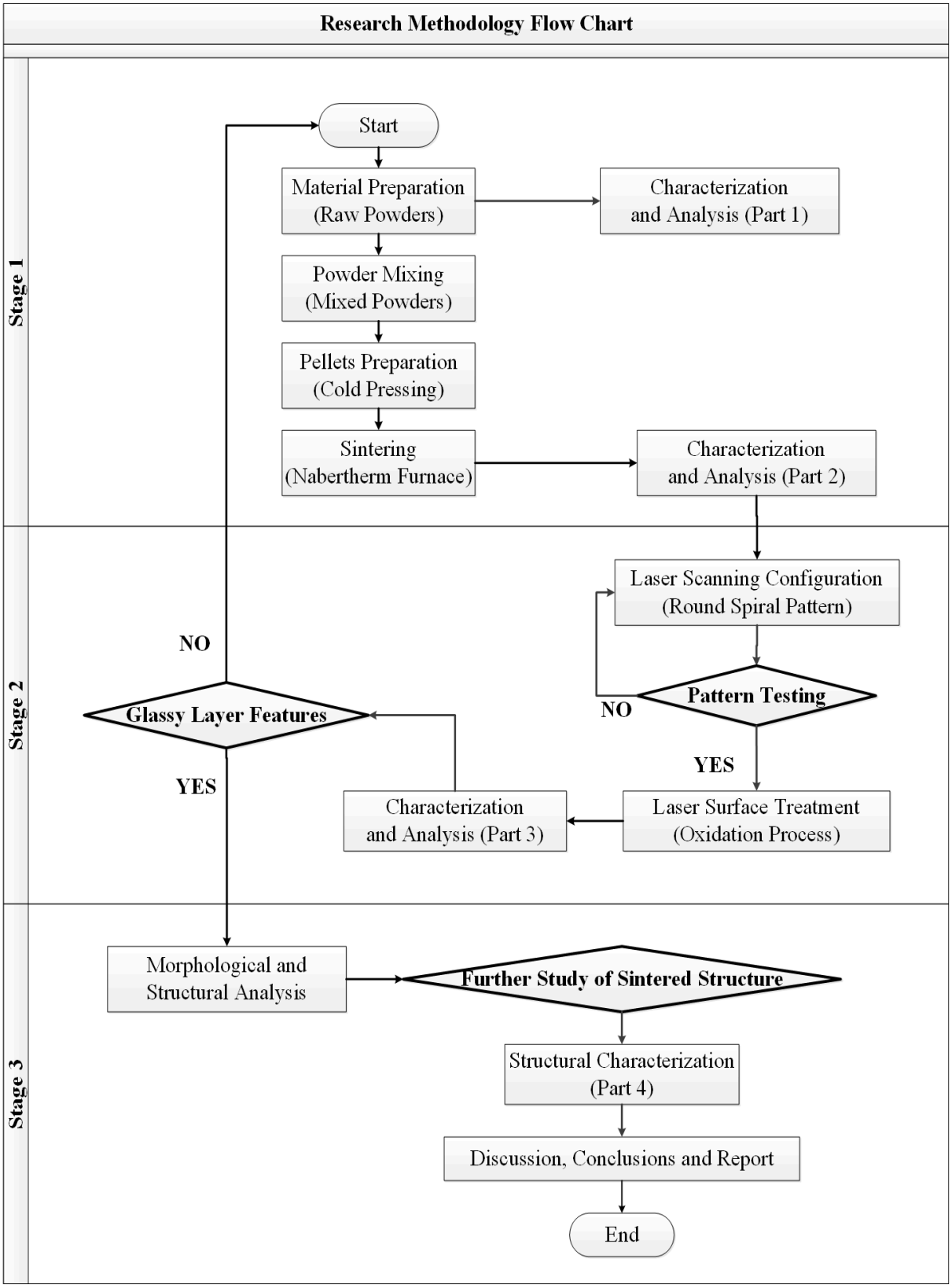

Figure 2.1: Research methodology flow diagram.

2.2 Materials Preparation, Selection Compositions and Powder Mixing

For the knowledge, this work was continuation of Lonné's research. The optimum composition of raw powders and sintering temperature were selected based on Lonné's research and the reported articles (Han et al., 2007; Lonné, 2011; Lonné et al., 2011, Lonné et al., 2012b; Zimmermann et al., 2008). It concluded the optimum composition and sintering temperature of both raw powders to obtain porosity at the range of 20 to 40% for efficient gas diffusion. The powder mixtures were divided into two batches in accordance to their sintering temperatures. The raw powders were purchased from H.C. Starck, USA. Grade B ZrB_2 was 97% + pure, TiB_2 was 98% + pure and Grade UF-25-α-SiC, purity was 98% +. Table 2.1 displays the raw powders properties which represent the physical properties of each type of powder employed. They were used directly, without further purification. The first batch of sample types, designations and compositions are presented in Table 2.2. They were sintered at 1900 °C of sintering temperature. Table 2.3 presents the second batch of sample types which were sintered at 2100 °C. For the mixing process, the mixed powders were prepared in 10 g total and immersed in 60 ml ligroin (petroleum ether; boiling point 40-65 °C; flash point -40 °C; density 0.65 g/cm^3 (20 °C)). Ligroin was selected as the dispersion medium. It was chosen because it did not affect the reaction mixture and merely used to disperse the raw powders to help the mixing process. The raw powders were then stirred together in ligroin inside a 30-kHz ultrasonic bath (Mecasonic, France) with powerful agitator for about 10 min stirring with a glass rod. The stirring process continued until the mixtures became visibly slurry and satisfied homogeneous. The slurry mixtures were placed under an extractor hood that lasted overnight to allow the ligroin evaporation as an initial drying. To ensure the mixed powders completely dried before the pelletizing, they were placed in the oven at 80 °C for 30 min.

Table 2.1: The properties of raw powders.

Material	Phase	Grade	Formula Weight (g/mol)	Density (g/cm^3)	Physical Properties						Supplier
					Particle Size (μm)				Specific Surface Area (m^2/g)	Melting Point (°C)	
					Average (Supplier Source)	Laser Diffraction Particle Size Distribution (Horiba-Partica LA-950V2)					
						D10	D50	D90			
Zirconium diboride (ZrB_2)	Hexagonal	B	112.84	6.1	1.5-3	2.41	3.97	5.93	N/A	3100-3500	H.C. Starck GmbH (Germany)
Titanium diboride (TiB_2)	Hexagonal	B	69.489	4.52	≤ 12	5.03	8.01	12.45	N/A	3230	
Silicon carbide (SiC)	Hexagonal (α-phase)	UF-25	40.1	3.21	0.45	0.25	0.47	0.95	23-26	2700	

Table 2.2: Sample types and compositions of mixture sintering at 1900 °C.

Sample Type	Designation	Composition						Law of Mixtures (vol.%) g/cm³
		First Batch						
		ZrB_2			SiC			
		Molar (mol.%)	Volume (vol.%)	Weight (wt.%)	Molar (mol.%)	Volume (vol.%)	Weight (wt.%)	
ZrB_2+α-SiC	61Z39AS	61	70	81	39	30	19	5.2330
TiB_2+α-SiC	61T39AS	61	66	73	39	34	27	4.0746

Table 2.3: Sample types and compositions of mixture sintering at 2100 °C.

Sample Type	Designation	Composition						Law of Mixtures (vol.%) g/cm³
		Second Batch						
		ZrB_2			SiC			
		Molar (mol.%)	Volume (vol.%)	Weight (wt.%)	Molar (mol.%)	Volume (vol.%)	Weight (wt.%)	
ZrB_2	100Z	100	100	100	0	0	0	6.1000
ZrB_2+α-SiC	90Z10S	90	93	96	10	7	4	5.8977
	85Z15S	85	89	94	15	11	6	5.7821
	80Z20S	80	86	92	20	14	8	5.6954
	75Z25S	75	82	89	25	18	11	5.5798
	70Z30S	70	78	87	30	22	13	5.4642

2.3 Pellet Sample Preparation by Cold Pressing

The pellet formation of mixed powders was shaped by uniaxial cold-pressed. The mixed powders were pelletized using stainless steel evacuable pellet dies (Ø = 10 mm) and Presses Atlas™ Manuelles Specac for uniaxial cold pressing (40 MPa). The principle of powder pressing is shown in Figure 2.2. The mixed powder weight for pelletizing was 1.25 g. The powder compaction method involved uniaxial pressure applied to the powder placed in a die between two rigid punches. It was effectively used for mass production of simple parts.

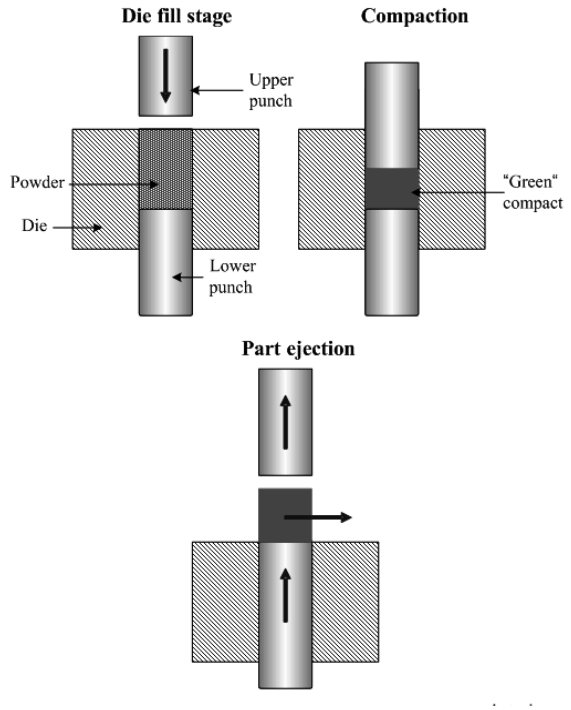

Figure 2.2: The principle of powder pressing (Specac 2013).

2.4 Pressureless Sintering and Polishing

Each of pellets were then sintered at 1900 °C and 2100 °C, respectively under argon flow (Alphagaz 1, Air Liquide, France) in the Nabertherm (VHT-08-22/GR) furnace equipped with a graphite resistor. The temperature setting was from ambient temperature to 1900 °C for the first batch as in Figure 2.3 and Figure 2.4 shows the sintering program at 2100 °C for the second batch, respectively. The heating and cooling rate were both employed at 10 °C/min followed by a dwell segment for 2.5 h, consecutively. The selection of sintering

temperature at 1900 °C was to achieve 80% to 90% samples densification. At 2100 °C sintering temperature was to improve the densification higher than 90%. Next, the sintered pellets were ground and polished to a 1 µm surface finish (standard surface roughness) by polishing machine (Mecatech 334 PRESI). Then, it was followed by ultrasonically cleaned with acetone and dried in the oven at 80 °C for at least for 12 hours. The pellets were polished to obtain surface homogeneity before continued to surface treatment by laser process.

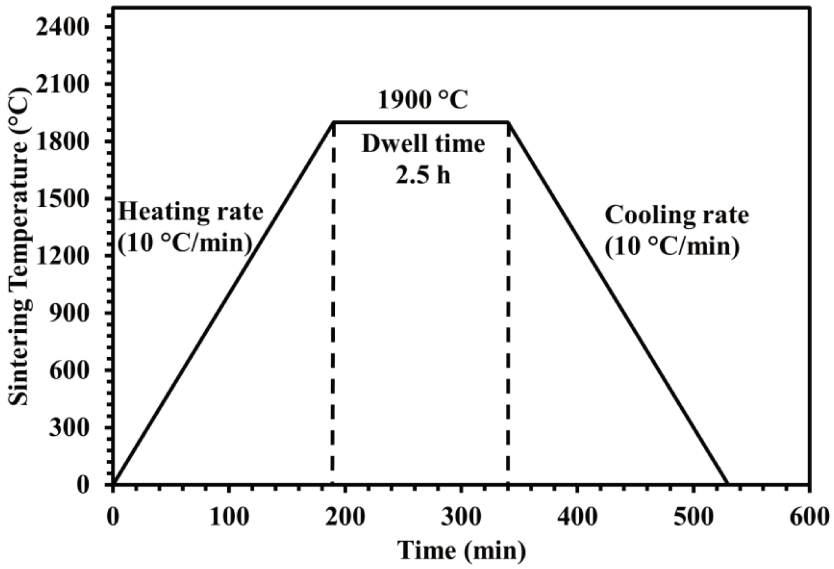

Figure 2.3: The sintering program at 1900 °C.

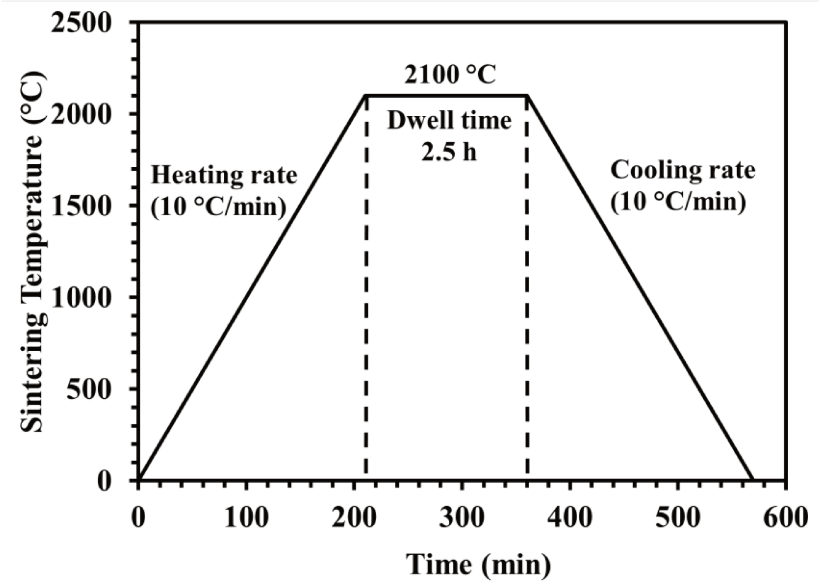

Figure 2.4: The sintering program at 2100 °C.

2.5 Ytterbium Fiber Laser and Scanning Pattern

The surface treatment was performed by an ytterbium fibre laser (IPG, Oxford, MA, USA; model LCF 100). It is associated with a high-resolution (> 0.0254 mm) motorized X-Y table, combined with an axes controller (Newport, CA, USA; models M-ILS 100CC and ESP300). The laser specifications are following: continuous wave, TEM_{00}, wavelength: 1072 ± 10 nm; maximum output power: 100 W and the spot diameter range from 1 to 5 mm. A beam reducer (LINOS) was also employed to reduce the spot diameter of the laser. The following are typical specification of YLR-100SM as presented in Table 2.4.

The laser oxidation was performed at laser power of 40 to 80 W. The laser beam was reduced to 1.25 mm with beam reducer. The laser operating parameter is presented in Table 2.5. The calculation of power density is straightforward. It is the power per unit area.

A round spiral laser pattern was designed and employed. A spiral laser pattern was developed in circular movement. The laser command for the spiral pattern can be found in Appendix A**.** At the best of knowledge, the spiral laser pattern was never being employed in other studies. This pattern was inspired to observe the possibility of producing glassy layer surface by spiral pattern depending on the sufficiency of laser power and favourable scanning rate. The round spiral laser pattern was induced on to the polished surface of ZrB_2-SiC and TiB_2-SiC pellets under the ambient surroundings. The round spiral pattern can be observed in Figure 2.5 and more details are being described below.

Table 2.4: Typical specification of YLR-100SM (An axes controller) (IPG Photonics Corporation 2016).

Optical Parameters	Unit	YLR-100SM
Mode of operation	-	CW
Central emission wavelength	nm	1075±5
Linewidth (FWHM)	nm	<3
Nominal output power	W	100
Output power tunability	%	10-100
Output power stability (long term)	%	+/-3
Typical beam quality	M^2	<1.1
Polarization extinction ratio	-	>17
Output fibre delivery	-	SM
Maximum modulation speed	kHz	40
Electrical Parameters		
Electrical measurement	V AC	110/220
Maximum power consumption	W	600
Cooling method	-	air
General Parameters		
Dimension (W×H×D)	cm	4U 19″
Weight	kg	15
Ambient temperature	^oC	0-45

Table 2.5: The laser operating parameter.

Beam diameter (mm)	Laser power (W)	Power density (kW/cm^2)
1.25	40	3.26
	50	4.07
	60	4.89
	70	5.70
	80	6.52

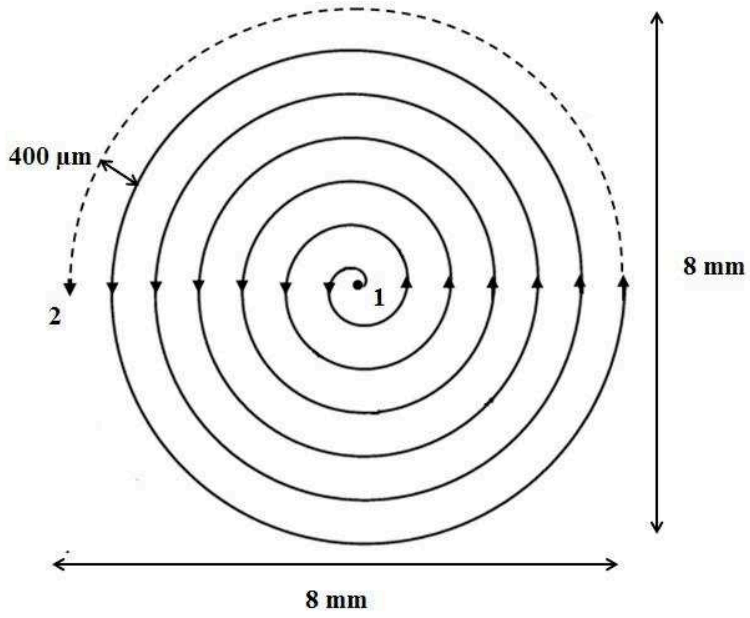

Figure 2.5: Schematic diagram of the round spiral laser pattern used in the present work for surface treatment.

The pattern dimension was 8 mm x 8 mm in diameter and the dimension size was chosen to be adapted to the size of pellet. It started from the inner centre part, which is indicated as 1, and ended at the outer part, indicated as 2. A complete round spiral pattern was produced by employing half circle each time and increased by 0.4 mm in diameter. It was executed in one cycle. Initially, the velocity of the X-Y table was conducted at 1 mm/s and 10 mm/s, respectively. Later, it was employed at 2 mm/s followed by acceleration and deceleration at 1 mm/s, respectively for the scanning effectiveness of the selected laser pattern. The scanning rate was selected mainly due to the notable change on the samples. In between the range of 1 mm/s and 10 mm/s, the structure evolution did not exhibit any notable change. The laser process with a round spiral pattern was accomplished in merely 5 min for a sample.

2.6 Characterization Techniques

The characterization techniques were employed onto the raw powders, sintered and surface-treated samples. The purpose was to study the microscopic structure and material properties. These characterization techniques were depended on the necessity, availability and accessibility of the equipment. Several equipment was discussed below.

2.6.1 Laser Diffraction Particle Size Analyzer

Laser scattering particle size distribution analyser (Horiba Partica LA-950V2) was performed for particle size distribution. The particle size was measured with the laser scattering method. The instrument detected the correlation between the intensity and the angle of light scattered from a particle, then calculated the particle size based on Mie-scattering theory (Scientific 2010). This technique was employed to ensure the raw powders were still in the industrial range size when they were purchased and kept. The results of microscopic particle measurements were presented based on the number and volume of the specific particles versus size.

2.6.2 Density Measurement

The density measurement is a measure of the "compactness" of matter within a substance. The experimental density of each pellet was calculated by measuring the mass (g), diameter (d), the thickness (t) and area (A) of the sintered pellets. Then, the density (ρ) was calculated using the formula: $\rho = \frac{m}{V}$. The theoretical density was calculated based on the law of mixtures. In example, $0.9\rho_{ZrB_2} + 0.1\rho_{SiC} = 5.8977\ g/cm^3$.

The density measurement was also performed by AccuPyc II 1340 Series Pycnometers. It uses the gas displacement method to measure volume. Inert gases, such as helium or nitrogen, are used as the displacement medium. Density calculations using the gas displacement method are much more accurate and reproducible than the traditional Archimedes water displacement method.

2.6.3 Scanning Electron Microscopy (SEM)/ Field Emission Scanning Electron Microscopy (FESEM) with Energy Dispersive Spectroscopy (EDS)

The morphological structure of raw powders, sintered pellets and laser-treated pellets were observed and analysed by Scanning Electron Microscope (SEM Philips XL30) equipped with Energy Dispersive Spectroscopy (EDS), Cambridge Instrument (Stereo scan 260) with EDS and Field Emission Scanning Electron Microscopy (FESEM-Joel JSM 7400F). The micrographs and EDS patterns were presented either in the secondary electrons mode (SE) or back-scattered electron mode (BSE).

The basic principle of SEM is that a beam of electrons is generated by a tungsten filament (field emission gun). The electron beam is accelerated through a high voltage (e.g.: 20 kV) and pass through a system of apertures and electromagnetic lenses to produce a thin beam of electrons., then the beam scans the surface of the specimen by means of scan coils (like the spot in a cathode-ray tube "old-style" television). Electrons are emitted from the specimen by the action of the scanning beam and collected by a suitably-positioned detector. The microscope operator is watching the image on a screen. Imagine a spot on the screen scanning across the screen from left to right. At the end of the screen, it drops down a line and scans across again, the process being repeated down to the bottom of the screen.

The Philips XL 30 is a conventional SEM. The microscope can be operated both at low accelerating voltage (200 V) and high accelerating voltage (30 kV). Resolution 3.5 nm at 30 kV, 25 nm at 1 kV Continuously Variable Accelerating Voltage Over the range 0.2 - 30 kV. Image rotation and focus automatically compensated over the full range. Continuously Variable Beam Current Control Maximum beam current: > 1 μA at 30 kV. 10 pre-calibrated values (spot sizes) and choice of automatic coupling of spot size to magnification.

The Cambridge Instruments Scanning Electron Microscope (SEM) is generally used for low-resolution imaging and teaching because of its user-friendly interface. It is also used to assess the preservation quality of samples before commencing with high-resolution imaging on the Helios 650 Dual Beam microscope. Also, this machine is very suitable for imaging bulk samples because of its large sample chamber and specimen stage. Image capture is facilitated using image grabber software (Orion) and uncompressed 8bit TIF images of 2560 × 2120 pixels can be digitally acquired.

The JSM 7400F is a field-effect SEM (FEG) cold cathode. It is intended for observation samples in ultra-high-resolution mode (nanometer-sized sample) especially in low voltage and chemical analysis of these samples. The resolution of this device is close to the nanometer even at low voltage. A detector of backscattered electrons (in lens) allows the study phase contrast at small distances from job. The principle is based on ultrafast freezing (a few milliseconds) of samples using Leica equipment EMPACT subjecting the sample to a jet of liquid nitrogen under high pressure.

All the samples were sputter-coated to prevent charging of the samples and improve the imaging. An ultra-thin coating of electrically-conducting metal was applied such as gold (Au), gold/palladium (Au/Pd), platinum (Pt) or carbon (C).

2.6.4 X-ray Diffraction (XRD)

X-ray diffraction (XRD) is based on constructive interference of monochromatic X-rays and a crystalline sample. These X-rays are generated by a cathode ray tube, filtered to produce monochromatic radiation, collimated to concentrate, and directed toward the sample. The interaction of the incident rays with the sample produces constructive interference (and a diffracted ray) when conditions satisfy Bragg's Law ($n\lambda = 2d \sin \theta$). This law relates the wavelength of electromagnetic radiation to the diffraction angle and the lattice spacing in a crystalline sample. These diffracted X-rays are then detected, processed, and counted. A key component of all diffraction is the angle between the incident and diffracted rays.

Siemens D5000 and Bruker D8 Advance were employed in this work. It was conducted to identify the presence of crystallize phases in a sample by comparison with standard patterns or reference patterns (Qualitative Analysis of XRD Data). Siemens D5000 diffractometer with a Cu anticathode monochromatized Cu Kα radiation under Bragg's Law, 35 kV voltage and 30 mA current and a back monochromator, working between 20° to 50° with a step of 0.02° and a 1.4 s exposure time. The diffraction patterns obtained were indexed with a DIFFRAC + EVA software (Bruker AXS) containing the Joint Committee on Powder Diffraction Standards (JCPDS) files database. For Advance Bruker D8 diffractometer with Cu Kα radiation (Billerica, MA, USA) under Bragg-Brentano configuration, 40 kV voltage and 40 mA currents. The parameters employed were 2θ° range that was 20° to 70° and the step size was 0.014° followed by step time of 174 s. The diffraction patterns obtained were analysed by International Centre for Diffraction Data (ICDD). The results obtained from both diffractometers were the same but for Advance Bruker D8, the peaks were more intensified compared to the Siemens D5000.

CHAPTER 3

Sintering of Zirconium Diboride-Silicon Carbide (ZrB_2-SiC) and Titanium Diboride-Silicon Carbide (TiB_2-SiC) Ceramic Composites at 1900 °C and Laser Surface Treatment

3.1 Results and Discussion

3.1.1 Powder Characterizations

Figure 3.1 displays the characterization analysis of SiC raw powder. From the SEM micrograph, the SiC grains in Figure 3.1(A) shows agglomerated powder. The reason was due to the high surface energy of particles that tends to agglomerate to minimize their excess surface energy. This was considered as soft agglomeration. Since the SiC grains were finer compared to ZrB_2 and TiB_2, the XRD analysis show broader peaks. No other impurities were detected in the XRD pattern. The particle size distribution displays a small bump in the starting of the graph. A small bump represents the minority amount of SiC finer sizes which leads to the soft agglomeration as seen in Figure 3.1(A). Overall, the mean size of SiC grains were d_{50} = 0.47 µm. Figure 3.2 displays the raw powder characterization analysis of ZrB_2. The ZrB_2 size were same as the as-received powders (d_{50} = 3.97 µm). XRD analysis exhibited less broad peak that represented the grains were bigger than SiC. No other distinct elements were detected in the XRD analysis. TiB_2 characterization is shown in Figure 3.3. SEM micrograph reveals an amount of irregular large sizes of TiB_2 grains. XRD analysis did not show any other peaks other than TiB_2 and the peaks were sharper due to larger size of grains. The particle size distribution exhibited d_{50} = 8.01 µm for TiB_2.

(A)

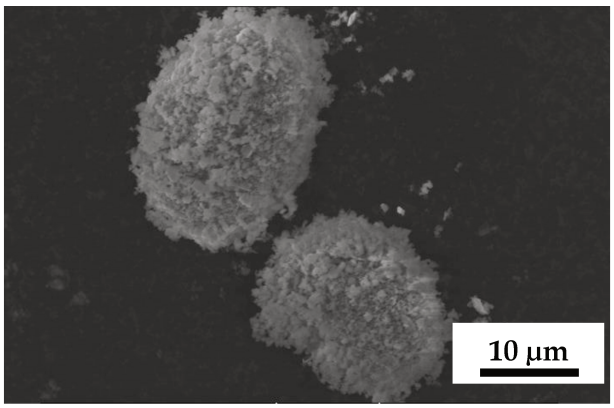

(B)

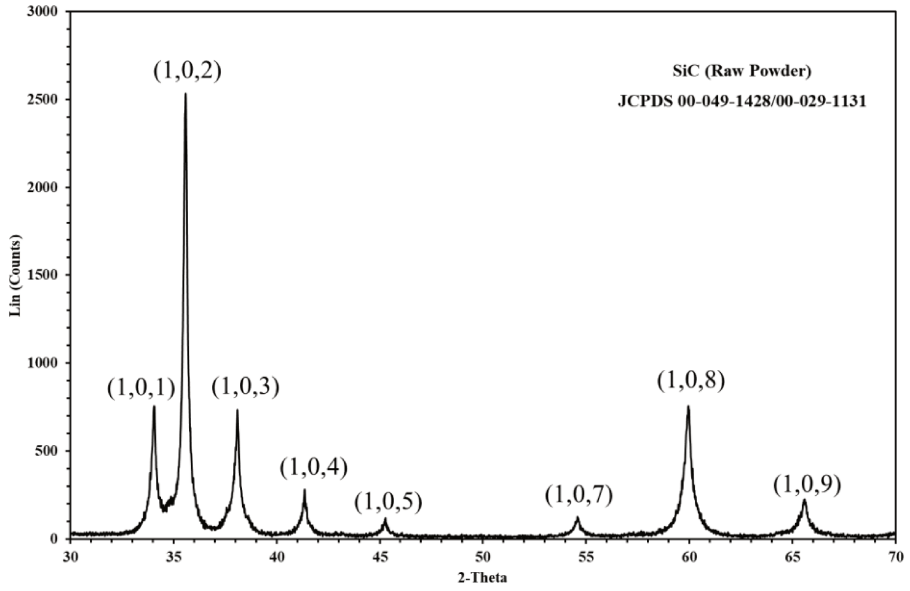

(C)

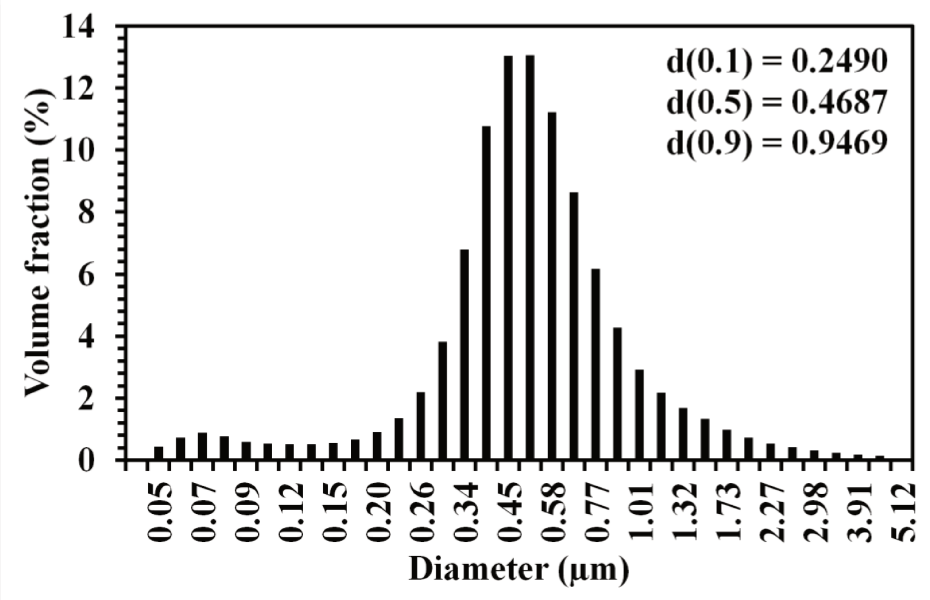

Figure 3.1: Analysis of SiC raw powders. (A) SEM micrograph (2000×), (B) XRD pattern and (C) Particle size distribution.

(A)

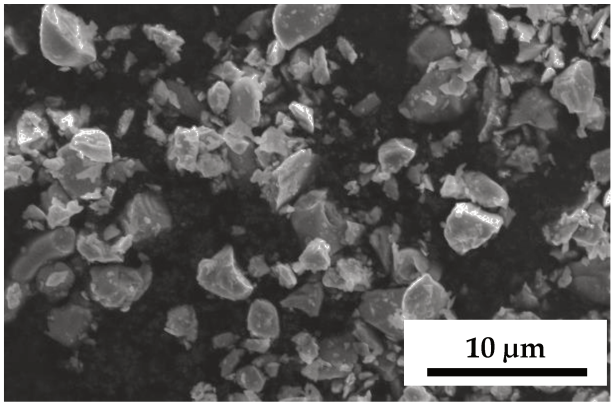

(B)

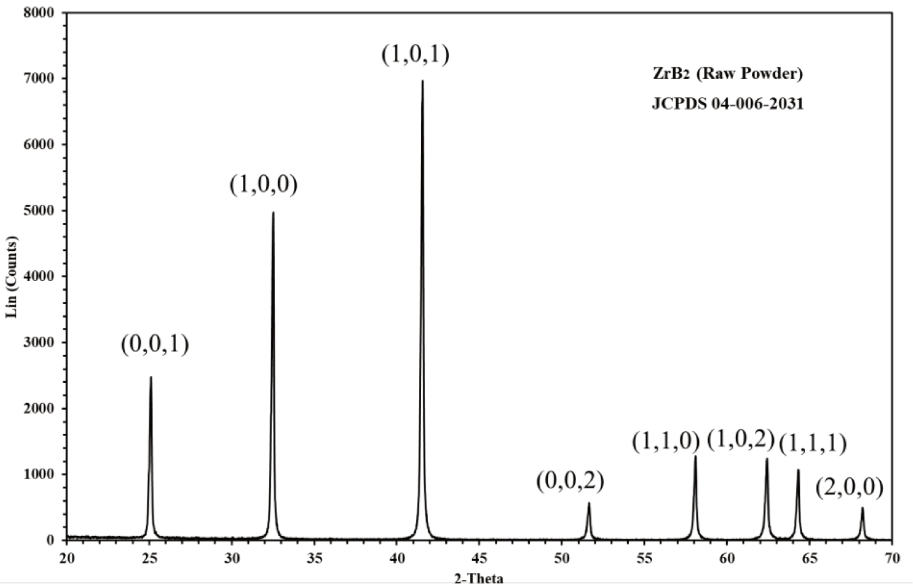

(C)

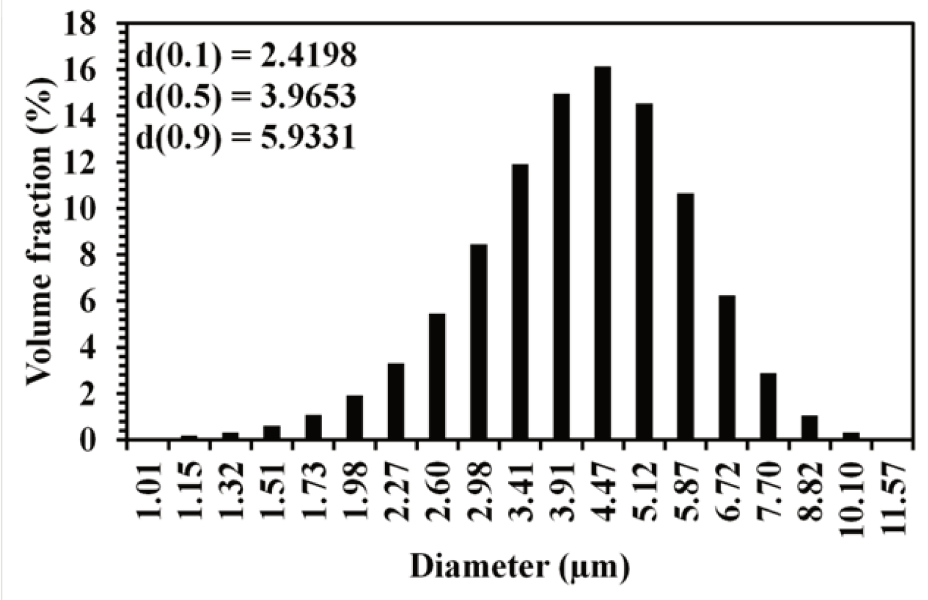

Figure 3.2: Analysis of ZrB_2 raw powders. (A) SEM micrograph (2500×), (B) XRD pattern and (C) Particle size distribution.

(A)

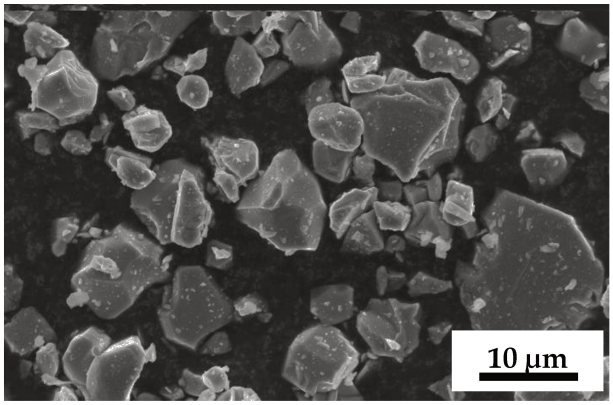

(B)

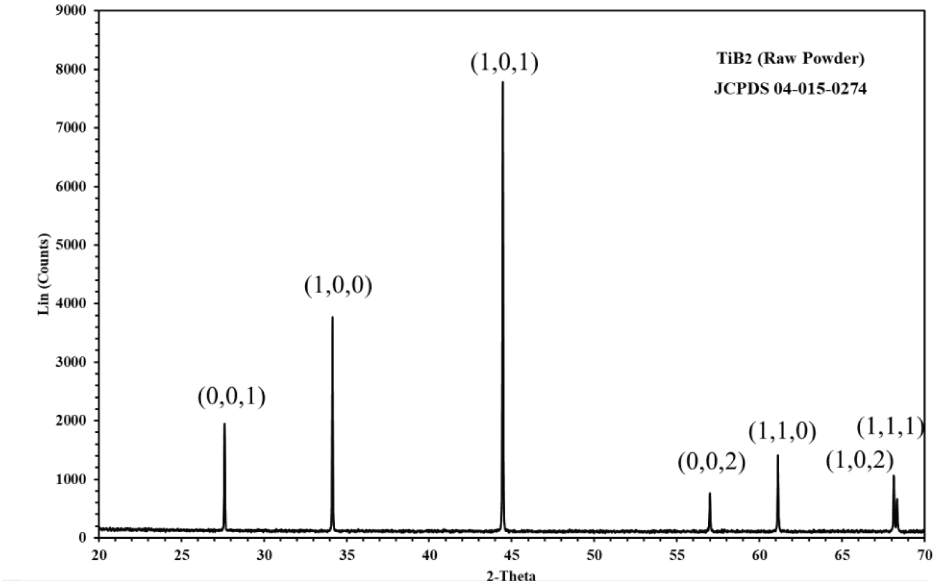

(C)

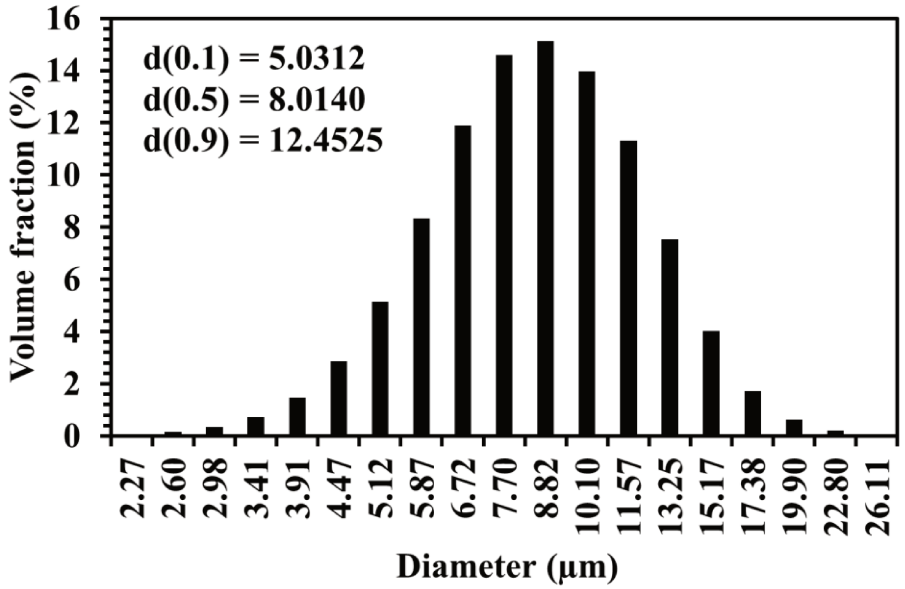

Figure 3.3: Analysis of TiB_2 raw powders. (A) SEM micrograph (2000×), (B) XRD pattern and (C) Particle size distribution.

3.1.2 Pressureless Sintering at 1900 °C

The sintering of 61 mol.% ZrB_2-SiC (61Z39S) and 61 mol.% TiB_2-SiC (61T39S) green body pellets at 1900 °C with the hold time of 2.5 h was carried out in a way to control the porosity in the appropriate range of 20% to 40%. At these range, the gas diffusion within the pores were effective as reported by Mougin et al. (2009). In Figure 3.4, the SEM micrographs of 61Z39S and 61T39S sintered pellets were observed at different magnifications. SEM micrographs reveal the porosities and different morphologies of sintered grains.

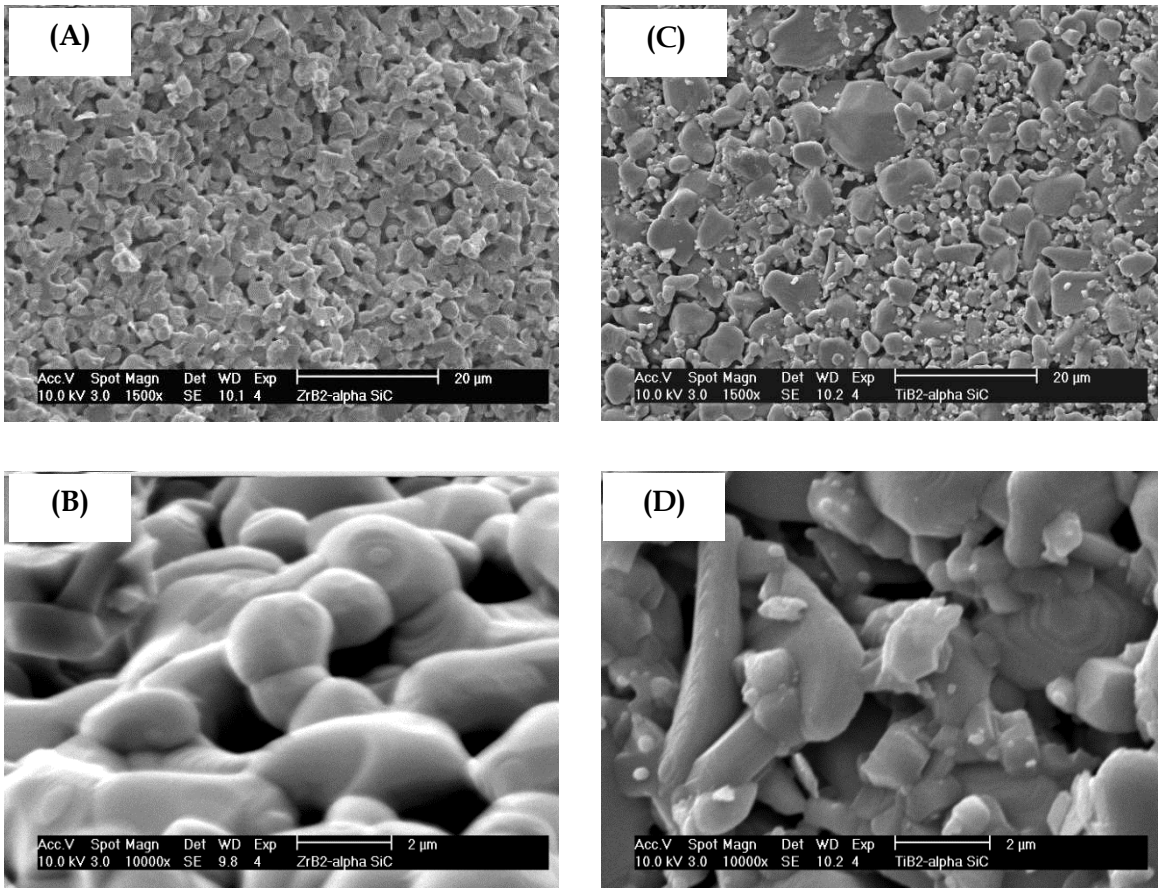

Figure 3.4: The SEM micrographs of sintered samples at different magnifications. (A) 61 mol.% ZrB_2-SiC (1500×), (B) 61 mol.% ZrB_2-SiC (10000×), (C) 61 mol.% TiB_2-SiC (1000×), and (D) 61 mol.% TiB_2-SiC (10000×).

The structure of sintered 61Z39S was observed in Figure 3.4(A) and it exhibited similar structure from the previous reported studies (Lonné et al. 2011; Sarin et al. 2010; Karlsdottir & Halloran 2009b). The porosity was measured by helium pycnometry and exhibited ca. 30% and this was also calculated geometrically as defined in Chapter 2 (Section 2.6.2, Page 82). The densification process had occurred, and the grain boundary diffusion can be observed better at higher magnification in Figure 3.4(B). The structures were observed more homogeneous and regular.

In Figure 3.4(C), the sintered 61T39S structures looked irregular. This was probably due to TiB_2 larger grains. SEM micrograph of sintered 61T39S at higher magnification in Figure 3.4(D) is presented for better view. It can be observed that the densification process had also occurred, however most of the consolidated structures were irregular. The porosity can also be observed. The porosity of sintered 61T39S was measured ca. 29%. Sintering at 1900 °C had shown the densification process of 61Z39S and 61T39S had occurred and exhibited porosities approximately 30%.

XRD was conducted to verify the elements presence in the sintered pellets of ZrB_2-SiC and TiB_2-SiC ceramic composites. As presented in Figure 3.5(A), sintered pellets of ZrB_2-SiC shows peaks of ZrB_2 however the SiC peaks were nearly invisible to observe. Initially, the XRD pattern was plotted in Lin (Counts) unit for y-axis. Therefore, the XRD pattern was again plotted in arbitrary unit to intensify the peaks of SiC as shown in Figure 3.5(B). From the new plotted XRD pattern, the SiC peaks were visible. It is evidenced that the SiC grains were retained in the pellet. Figure 3.5(C) displays the XRD pattern of the sintered pellet of TiB_2-SiC. Both peaks of TiB_2 and SiC can be observed in the XRD pattern. This concludes that throughout the sintering process, no other significant grains, or impurities were formed that might affect the densification of pellets.

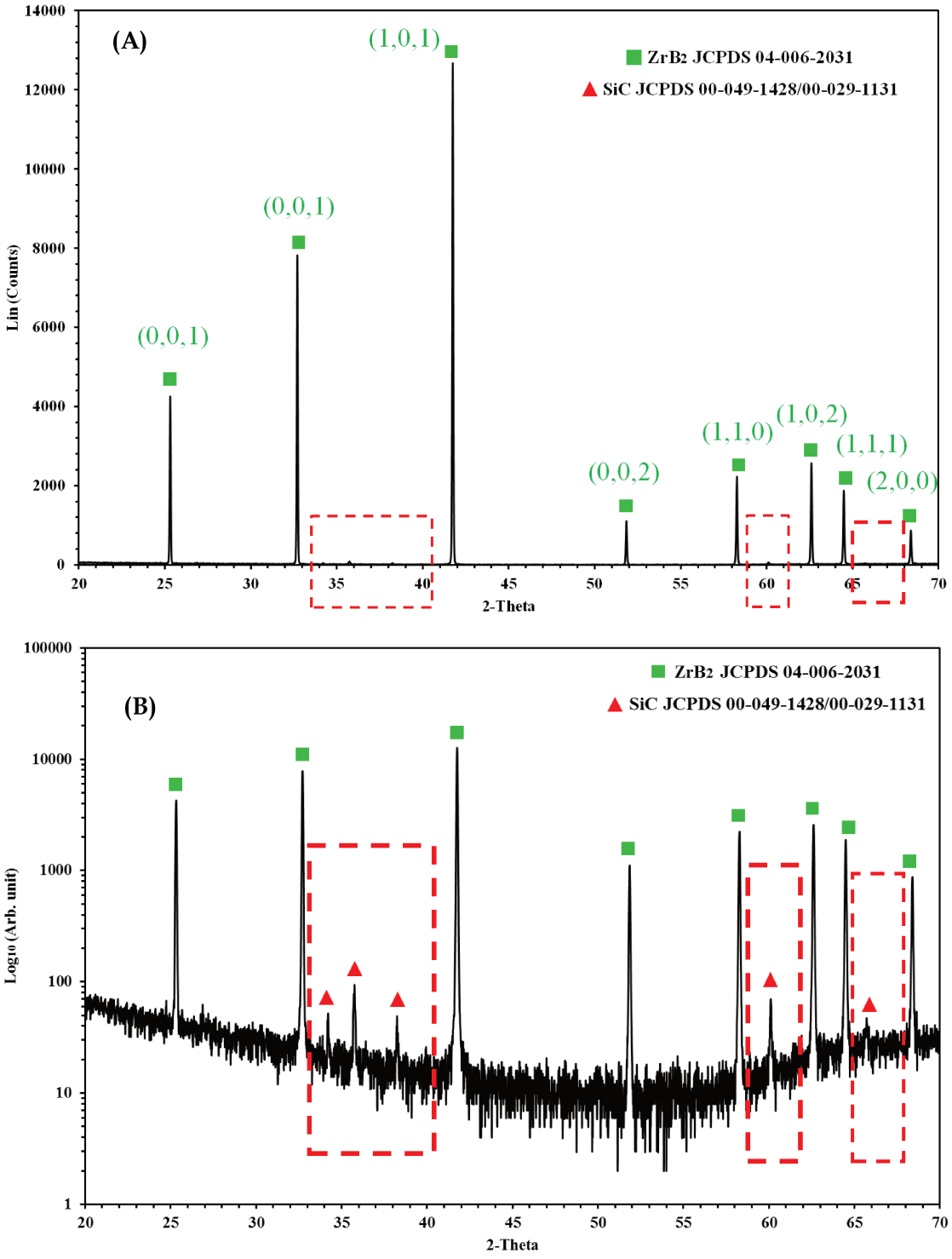

Figure 3.5: XRD patterns of sintered samples. (A) ZrB_2-SiC (Counts per second unit), (B) ZrB_2-SiC (Arbitrary unit), and (C) TiB_2-SiC (Counts per second unit).

Figure 3.5 continued.

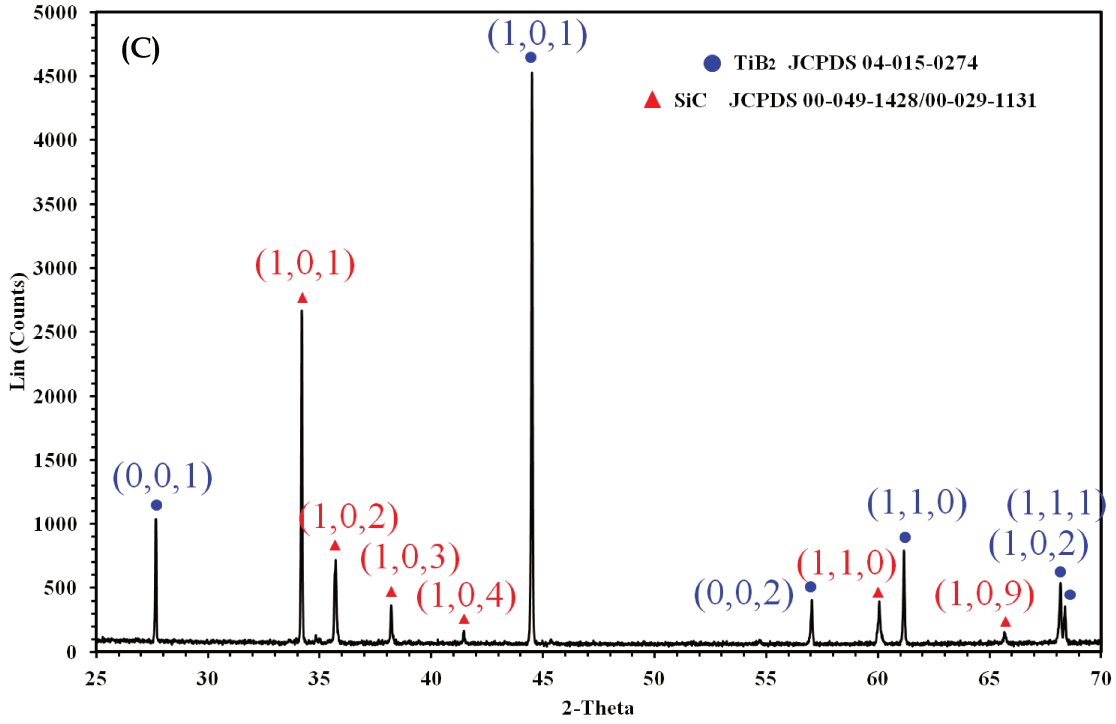

3.1.3 Microstructure Evolution after Laser Surface Treatment

This section discusses on the transformation of 61Z39AS and 61T39AS after laser oxidation at laser power of 60 W. The scanning rate of 1 mm/s and 10 mm/s were employed. Figure 3.6 and Figure 3.7 represent the SEM micrographs of 61Z39AS and 61T39AS transformation before and after laser treatment. The EDS analysis was conducted to identify the presence of elements after laser treatment.

Figure 3.6(A) to (C) displays the SEM micrographs and EDS analysis of sintered 61Z39AS. At scanning rate of 1 mm/s, the pellet can be seen changing its structure as observed in Figure 3.6(A) which displays the sintered structure to Figure 3.6(B), the laser-treated surface. Meanwhile, for scanning rate of 10 mm/s, the pellet was totally damaged and broken. Thus, this section discusses on the scanning rate of 1 mm/s only as presented in Figure 3.6(B) and Figure 3.6(C).

Figure 3.4(B) displays the sintered 61Z39AS grain surfaces at higher magnification which appeared to be smooth compared to Figure 3.6(C), the laser-treated pellet. It shows the grain structure was incompletely oxidized. No glassy surface can be observed, and it was just an

incomplete oxidation of 61Z39AS. The structure might display the beginning of oxidation. It displays the uniform stones-like structures of 61Z39AS. The presence of zirconium, boron, silicon, carbon, and oxygen elements were detected by EDS analysis. The compounds probably identified as remaining ZrB_2 and SiC phases and several new phase formations of boron oxide/boria (B_2O_3), silica (SiO_2) and zirconia (ZrO_2) grains. These formations would probably because of the evaporation-condensation phase, which atoms were diffused from the grain surface to the neck surface. In this mass transfer process, the neck grows but centre-to-centre distance between grains remains the same. Therefore, no glassy feature occurred.

Overall, the results indicate that at 60 W laser power, the ZrB_2-SiC ceramic composites (61Z39AS) were unable to be fully oxidized to form glassy structures. The changes of structures were incomplete due to insufficient laser power at the scanning rate of 1 mm/s. For higher scanning rate of 10 mm/s, it was unsuitable. It was too fast that led to the damaged of the pellet. The increase of laser power was later performed to see if there were any changes.

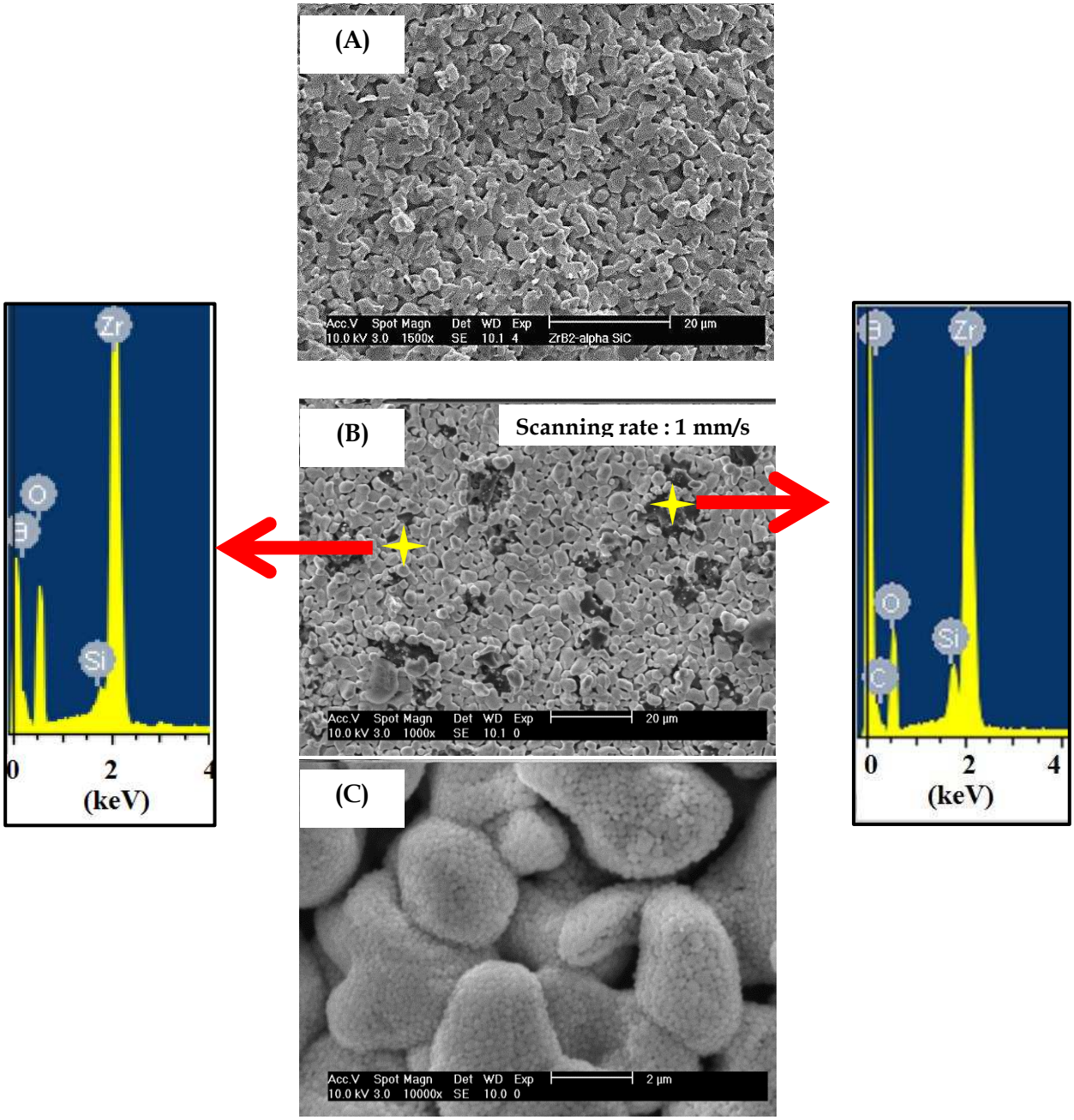

Figure 3.6: Secondary electron images of the transformation of sintered pellet of ZrB_2-SiC after laser treatment. (A) Sintered pellet (1500×), (B) Laser-treated pellet (1000×) and (C) High-magnification (10000×).

Figure 3.7(A) to (D) present the evolution of 61T39AS structures before and after 60 W laser treatment at scanning rate of 1 mm/s and 10 mm/s, respectively.

Figure 3.7(A) shows the 61T39AS sintered structure and changes after 60 W laser power and 10 mm/s scanning rate as shown in Figure 3.7(B). It exhibited irregular and unsmooth structure. To observe better, higher magnification in Figure 3.7(C) is presented. Hairy structure can be observed in Figure 3.7(C). This structure represents the initial state of oxidation. From EDS analysis, the presence of boron, titanium, oxygen, and silicon elements can be observed. These phases probably be the formation of TiO_2, SiO_2 B_2O_3 grains or the residual of TiB_2 and SiC grains. Carbon could not be seen from the EDS pattern due to its light element. It might be overlapping with boron element.

For scanning rate of 1 mm/s, the microstructures resulted in cracked, bubble look alike and dense as shown in Figure 3.7(D). The cracked was due to the rapid cooling of oxidation. Generally, it was due to the melted B_2O_3 and TiO_2. The bubbles formation was due to the release of gases throughout the oxidation process. They were observed as the residual feature of evaporation of SiO_2, SiO, CO or CO_2 gaseous. EDS analysis shows the Ti, Si, B and O elements were very likely under the form of oxidized phases such as TiO_2, SiO_2 B_2O_3 compounds. It is concluded that the occurrence of oxidation can be observed from the formation of dense structure, however an inhomogeneous surface was exhibited.

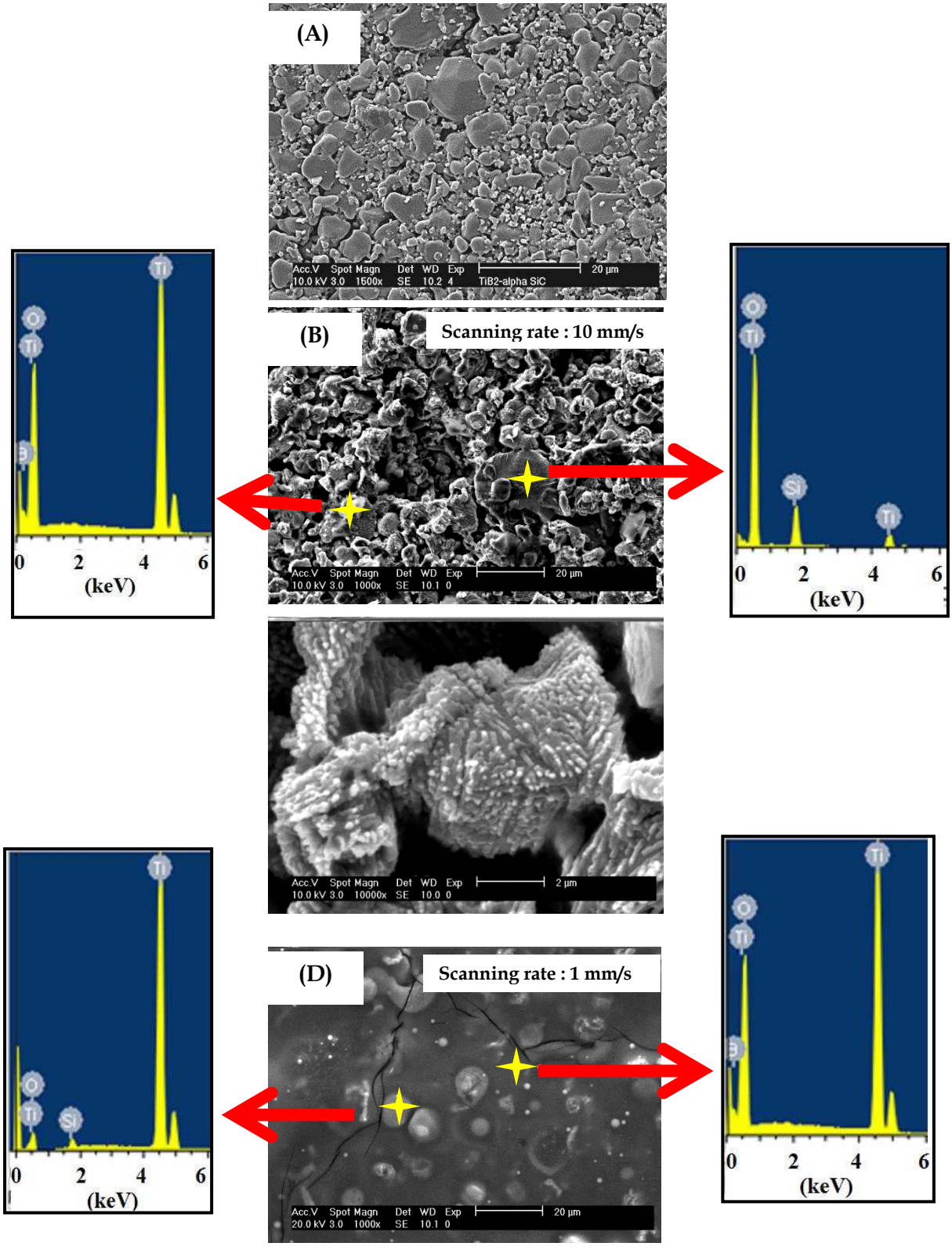

Figure 3.7: Secondary electron images of the transformation of sintered pellet of TiB_2-SiC after laser treatment. (A) Sintered pellet (1500×), (B) Laser-treated pellet (Area 1-1000×), (C) High-magnification (10000×) and (D) Laser-treated pellet (Area 1-1000×).

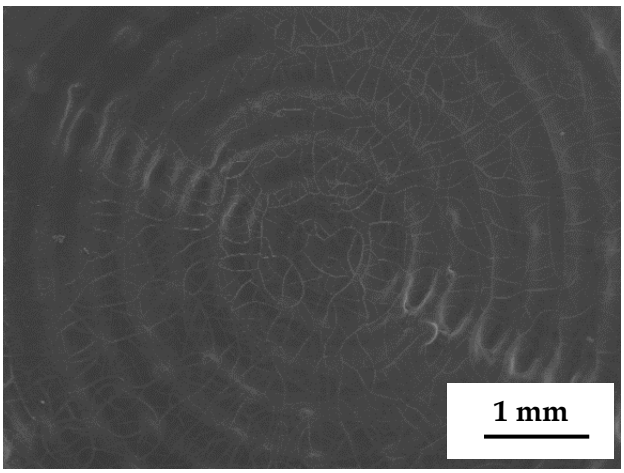

Figure 3.8: SEM micrograph of ZrB_2-SiC laser-treated at 70 W (20×).

As laser power of 60 W and 1 mm/s scanning rate was insufficient for ZrB_2-SiC (61Z39S) pellet, the laser power was then increased to 70 W with the same scanning rate to observe the changes. It shows a smooth layer feature as shown in Figure 3.8. It seems that at 70 W, a layer was successfully formed and even the spiral laser tracks can be observed too. This study would further be explained and discussed in Chapter 4.

3.2 Summary

The different laser effects have been observed for ZrB_2-SiC (61Z39S) and TiB_2-SiC (61T39S) samples. For 61T39S pellet, 60 W laser power and 1 mm/s scanning rate exhibited a dense structure with presence of various shapes of bubbles and crack deflection on the surface. For 61Z39S pellet, 60 W laser power was insufficient to form a glassy layer. However, when increased to 70 W laser power, the 61Z39S ceramic composites exhibited better surface. Further study on a detailed observation of laser-treated surface would be discussed in Chapter 4.

CHAPTER 4

Surface Oxidation of Porous Zirconium Diboride-Silicon Carbide (ZrB_2-SiC) Ceramic Composites by Continuous-Wave Ytterbium Fiber Laser

4.1 Results and Discussion

4.1.1 Pressureless Sintering at 1900 °C

After sintering and polishing, the surface of ZrB_2-SiC pellets exhibit a typical microstructure (Figure 4.1), in very good agreement devoted to ZrB_2-SiC composites with other results of the literature (Fahrenholtz, 2007; Han et al., 2007; Hu et al., 2009; Karlsdottir and Halloran, 2007; Karlsdottir et al., 2009b; Karlsdottir et al., 2007; Kim et al., 2014; Li et al., 2013; Lonné et al., 2011; Lonné et al., 2012a; Patel et al., 2012; Rezaie et al., 2007; Simonenko et al., 2013; Tian et al., 2011; Wuchina et al., 2007; Zhu et al., 2007; Zimmermann et al., 2008). In Figure 4.1(A), the SEM image in the backscattered electrons mode shows typical SiC grains in dark grey, and the ZrB_2 matrix in light grey. The SiC grains are uniformly dispersed within the ZrB_2 matrix. With the image of Figure 4.1(B) in the secondary electrons mode, it also reveals the remaining porosity of the sintered ZrB_2-SiC pellets. It has been estimated at ca. 30% and the error was ± 0.01 as measured by helium pycnometry and this is in accordance with Mougin et al. (2009) that suggested, the preferable porosity of electrodes is in the range of 20 to 40% particularly for solid oxide fuel cell application.

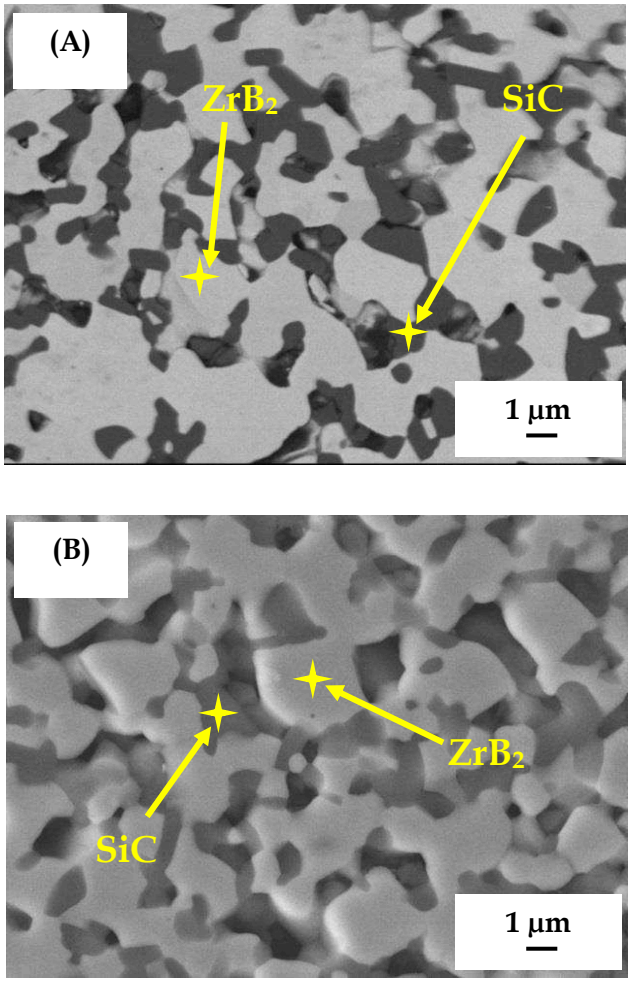

Figure 4.1: Surface morphology of ZrB_2-SiC polished surface after sintering at 1900 °C for 2.5 h. (A) Backscattered electrons mode (BSE) (4000×), and (B) Secondary electrons mode (SE) (4000×).

Table 4.1: The operating parameters of ytterbium fibre laser irradiation.

Operation mode	Laser pattern	Beam diameter (mm)	Laser power (W)	Power density (kW/cm²)
Continuous-wave	Round spiral	1.25	50	4.07
			60	4.89
			70	5.70

4.1.2 Laser Pattern and Settings for Oxidation Process

The surface treatment was performed by an ytterbium fibre laser as discussed in detail in Chapter 2 (Section 2.5, Page 77). The operating parameters are represented in Table 4.1. Initially, the laser treatment was performed at 50 W and gradually increased to 60 and 70 W on the same surface area. However, at 50 and 60 W the oxidation was incomplete and inhomogeneous. The photographs of untreated and laser-treated on the surface samples can be observed in Figure 4.2. A better laser surface treatment was achieved by employing the laser power of 70 W. The beam diameter was reduced to 1.25 mm with the beam reducer and the power density of 5.7 kW/cm^2 was used in this experiment. The velocity of the X-Y table was employed at 2 mm/s followed by acceleration and deceleration at 1 mm/s, respectively. The laser process with a round spiral pattern was accomplished in a ca. 5 min. It is evidently a short processing time with a high degree of heat localization.

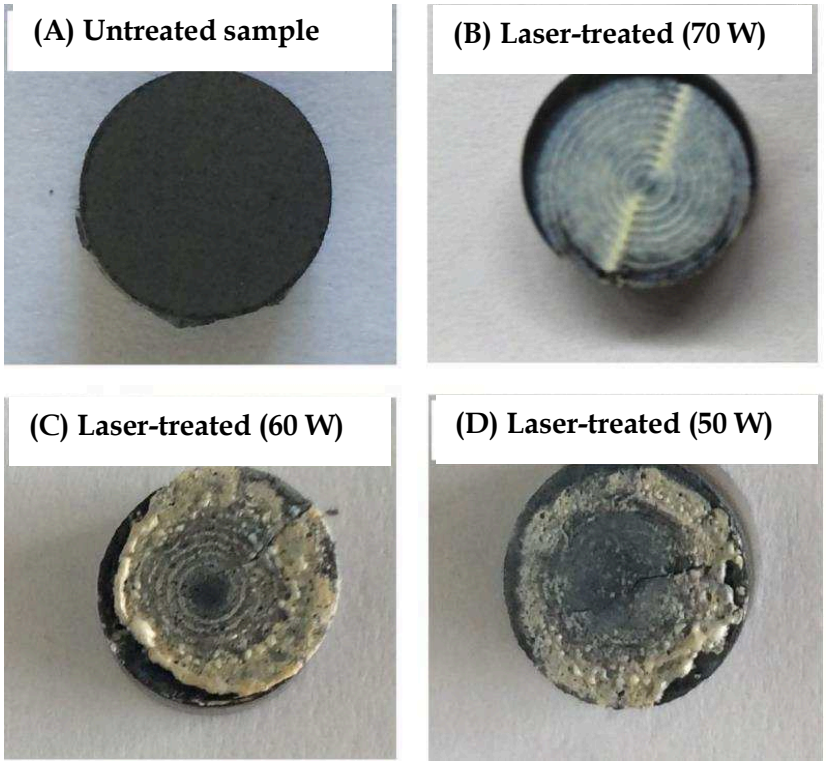

Figure 4.2: Photographs of ZrB_2-SiC pellet. (A) Untreated sample, (B) Laser-treated at 70 W, (C) Laser-treated at 60 W and (D) Laser-treated at 50 W.

4.1.3 Morphological Structure at Laser Power of 70 W

Then, the laser surface treatment was conducted at laser power of 70 W. The surface transformation of ZrB_2-SiC after laser oxidation can be observed in Figure 4.3(A). The laser pattern is visible because of the overlapping laser track. The heat diffusion ignited at the centre and homogeneously spreads out. As a result, the ZrB_2-SiC surface melted and re-solidified, which contributed to the molten tracks formation, as displayed in Figure 4.3(A).

Generally, one of the crucial issues of performing laser for ceramic surface treatment is the crack formation during the rapid cooling. As can be seen in Figure 4.3(A), large and deep cracks are undetectable on the surface of laser-oxidized ZrB_2-SiC. The un-cracked surface formation is probably due to the appropriate laser pattern and parameters applied in the present work that might modify the heat transfer conditions on the ZrB_2-SiC surface, resulting in slower surface cooling rates. Nevertheless, crazing of very fine cracks is present. However, it seems that the network made by these very fine cracks are not connected. Indeed -and as the reader will see below- there is no ingress of air and oxygen, because the zone just below and the bulk is not oxidized. The laser surface treatment employed in this work can eliminate pores and creating a homogeneous surface, hence improving the high-temperature degradation resistance of ZrB_2-SiC, under ambient temperature.

The SEM image in Figure 4.3(B) shows a higher magnification of the laser-oxidized ZrB_2-SiC surface. Again, it can be seen a smooth glassy surface, with no cracks. This is in accordance with previous works (Hu et al., 2009; Li et al., 2013; Lonné et al., 2011) but where oxidation was carried out with classical furnaces. The surface layer is principally made of a completely covering, borosilicate glass due to the following reaction equations (4.1) and (4.2):

$$ZrB_2(c) + \frac{5}{2}O_2(g) \rightarrow ZrO_2(c) + B_2O_3(l) \qquad (4.1)$$

$$SiC(c) + \frac{3}{2}O_2(g) \rightarrow CO(g) + SiO_2(c) \qquad (4.2)$$

and mixing of the products SiO_2, B_2O_3, and very probably ZrO_2 (Karlsdottir & Halloran 2009b). This determines that the laser is highly applicable for heating this kind of ceramics. Moreover, surface oxidation of the laser is a rapid process (ca. 5 min) compared to classical furnaces, the heated zone is highly localized, and there is a great choice of various pattern shapes (spiral round, square etc.). Figure 4.3(B) also shows white spherical particles with a

roughly 2 μm diameter, embedded below the glass outer layer. These had already been reported in previous research (Han et al., 2007; Hu et al., 2009; Patel et al., 2012). The formation of white spherical particles is attributed to the liquid transport of the SiO_2-ZrO_2 solution to the surface and then coagulated at the silica rich surface layer (Han et al. 2007). The white spherical particles consist of Si, O and Zr as shown in EDS analysis of Figure 4.3(C). It is concluded that these particles made of ZrO_2 that are trapped in the silica-rich glass layer.

Figure 4.4 displays the fractured cross-section of the laser treated ZrB_2-SiC at various magnifications. The wavy nature of laser pattern is evident on the Figure 4.4(A); it is interesting to note that the distance between two apexes, i.e., where the laser track overlaps, is indeed 400 μm, that is parallel with the parameter set for the pattern (cf. Figure 2.5). Figure 4.4(B) shows a multilayer structure and Figure 4.4(C) is a close-up of the SiO_2-rich top layer. The formation of a glassy SiO_2-rich layer on the surface of ZrB_2-SiC in this work strongly indicated that the heat of the laser beam is assumable at around 1300 °C or more (Hu et al., 2009). As the ZrB_2-SiC is heated, the morphology and composition of the surface layer change according to equation (4.1), and as the heat increases B_2O_3 evaporates rapidly due to its very high vapor pressure at high temperatures (ca. 0.7 kPa at 1300 °C), leaving ZrO_2:

$$B_2O_3(l) \rightarrow B_2O_3(g) \qquad (4.3)$$

Then, from the kinetic point of view (Hu et al., 2009), the oxidation of SiC has taken place (Reaction 4.2). Figure 4.4(B) reveals that the laser-formed multilayer structure comprises a thin glassy layer rich of silica, the zirconia particulates embedded inside this silica layer and an unoxidized zirconium diboride with much more porous than the starting material because it is SiC-depleted layer, and with minor traces of ZrO_2. The SiC-depleted zone is developed due to the active oxidation of equations (4.4) and (4.5), where silicon monoxide SiO is gaseous (Fahrenholtz 2007):

$$SiC(cr) + O_2(g) \rightarrow SiO(g) + CO(g) \qquad (4.4)$$

$$SiC(cr) + 2O_2(g) \rightarrow SiO_2(g) + CO_2(g) \qquad (4.5)$$

The formation of SiO_2-rich layer (Figure 4.4(C)) is identified to be a shield from inward oxygen penetration into the inner bulk, thus enhancing the resistance to oxidation (Han et

al., 2007; Hu et al., 2009). Meanwhile, the zirconia particulates formed inside the glassy SiO_2 can act as the secondary barrier that restricts the oxygen incoming (Hu et al., 2009).

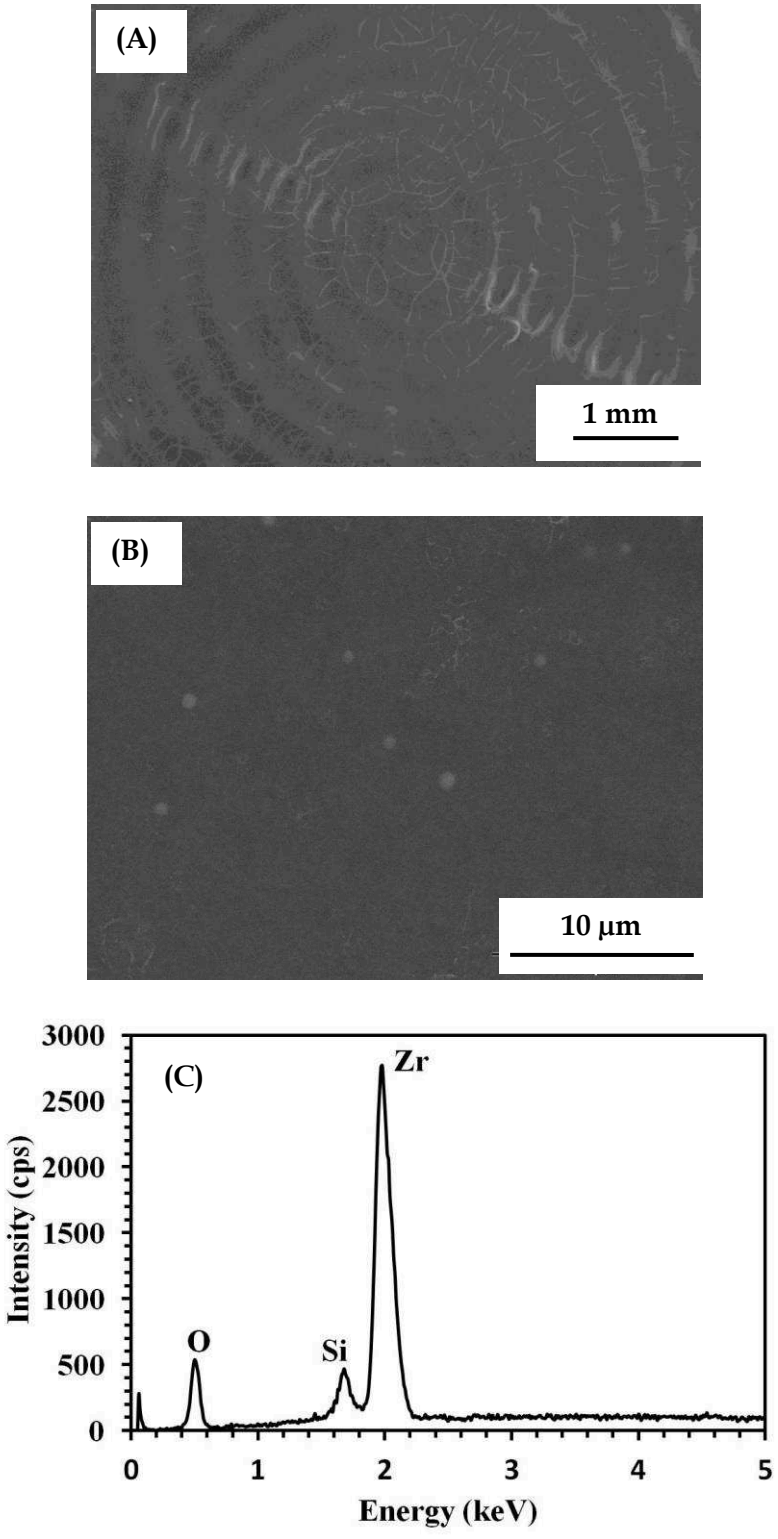

Figure 4.3: SEM micrographs and EDS analysis of ZrB_2-SiC surface after laser treatment performed at 70 W. (A) Low-magnification SEM image (20×), (B) High-magnification SEM image (4000×) and (C) EDS analysis of white spherical particles.

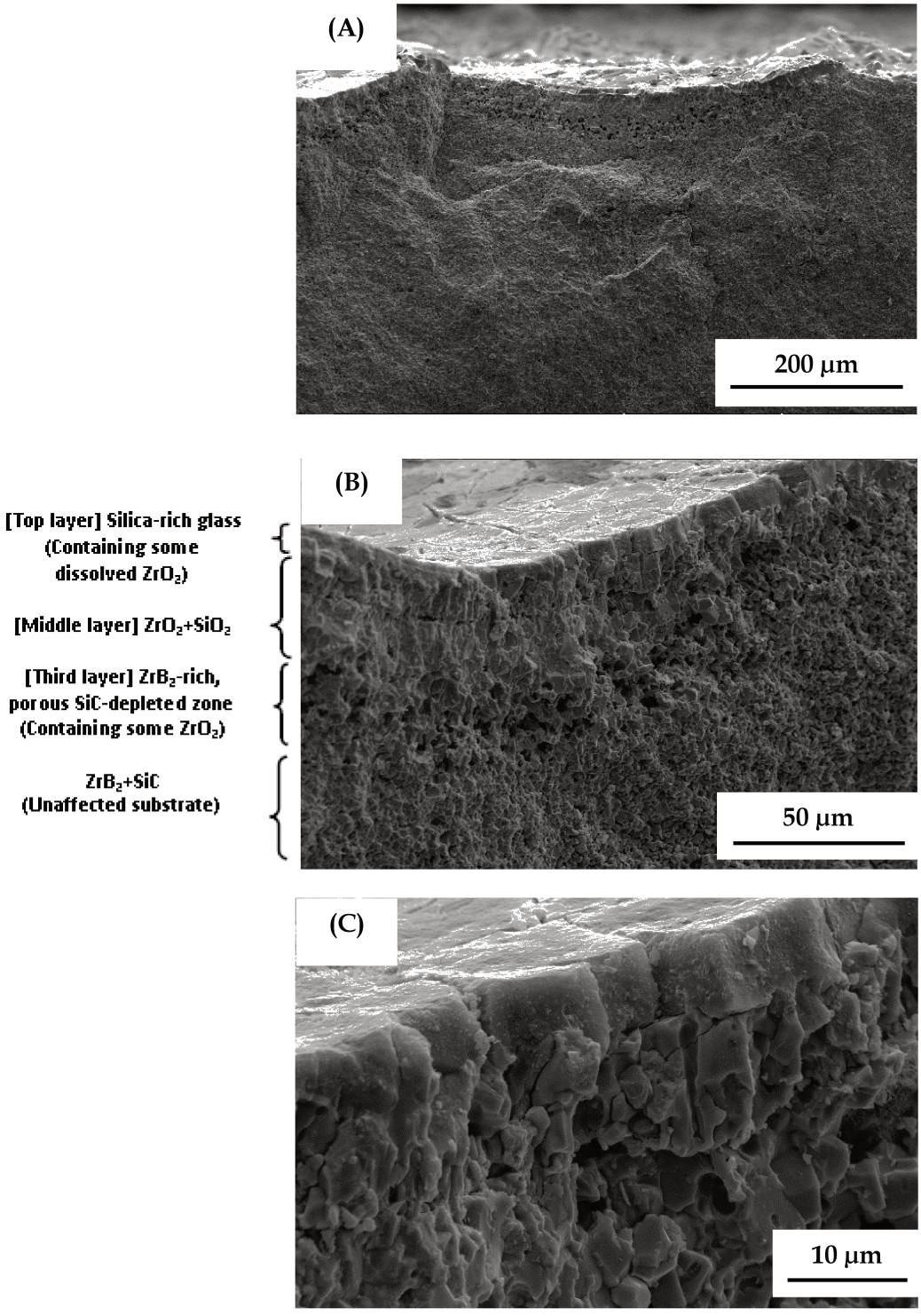

Figure 4.4: Micrographs of ZrB_2-SiC fractured cross-section after laser treatment (70 W) at various magnifications. (A) 200 µm (150×), (B) 50 µm (600×), (C) 10 µm (2000×), and (D) 20 µm (1000×) in BSE mode.

Figure 4.4 continued.

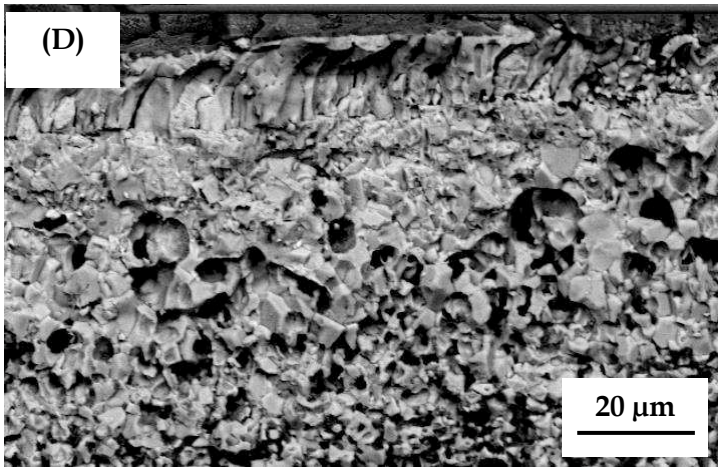

From Figure 4.5(A), the distinct thin glassy of SiO_2-rich outer layer can be observed and the thickness is estimated at about 8.3 ± 1.4 µm. This layer is recognized to act as a barrier to prevent inward oxygen diffusion into the inner bulk; this layer blocks the oxidation process by protecting the surface of the grains hence enhancing the resistance towards oxidation (Hu et al., 2009; Li et al., 2013; C. Tian et al., 2011) as discussed earlier in the previous paragraph.

Figure 4.5(B) also exposes ZrO_2 particulates present inside the borosilicate layer. They are observed clearly inside the SiO_2-rich scale. This is consistent with previous studies (Han et al., 2007; Karlsdottir and Halloran, 2007; Karlsdottir et al., 2007). The presence of zirconia particulates in the glassy layer is considered to act as secondary protector to restrict the permeability of oxygen (Gao et al. 2013).

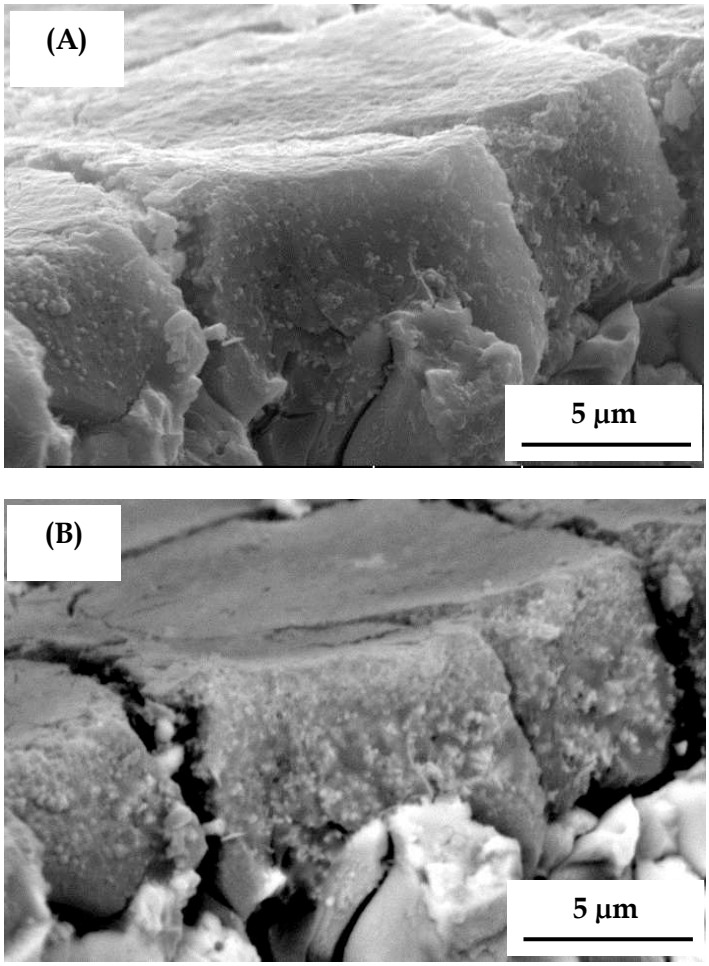

Figure 4.5: Micrographs of SiO_2-rich glassy layer fractured cross-section. (A) Secondary electrons mode (SE) (5000×) and (B) Backscattering electrons mode (BSE) (5000×).

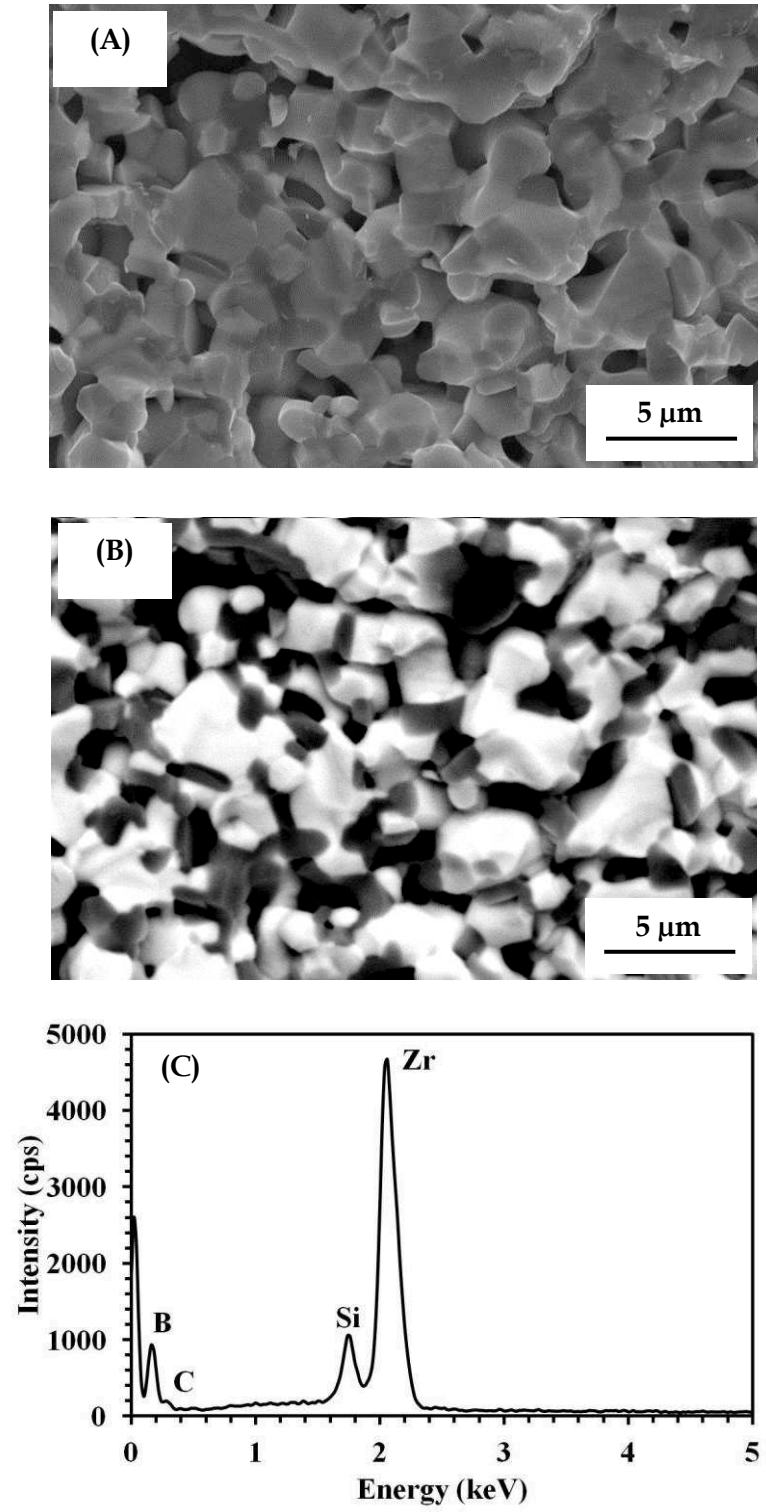

Figure 4.6: Micrographs and EDS analysis of ZrB_2-SiC inner bulk fractured cross-section after laser treatment (70 W). (A) Secondary electrons mode (SE) (4000×), (B) Backscattering electrons mode (BSE) (4000×) and (C) EDS spectrum of (B).

Figure 4.6 shows the inner bulk structure of fractured ZrB_2-SiC after surface treatment. From the observation of Figure 4.6(A) and (B), the structure is very well preserved. The morphology is similar to that of initial sintered non-oxidized pellets (cf. Figure 4.1). The EDS analysis in Figure 4.6(C) verifies the oxidation did not take place in the inner bulk of ZrB_2-SiC due to the undetectable oxygen element. A classical approach of oxidation in a furnace would tend to oxidize the whole pellet and at this point, the laser had proven that it could particularly oxidize the top of ZrB_2-SiC layer and still preserved the inner bulk layer. It has been strongly demonstrated the high heat-localized ability of a laser.

The EDS analysis of the fractured cross-section is presented in Figure 4.7. It allows to confirm the SEM description of multilayer structure above (cf. Figure 4.4(B)). The EDS analysis of Figure 4.5(A) displays that the top layer consists of Si, O, Zr, and C elements. The presence of these elements can be explained from the oxidation equations of Equation 4.1 and Equation 4.2. Once the SiC starts to oxidize, it produces the molten SiO_2. It was due to the presence of B_2O_3. It is possible for gaseous species such as CO and/or CO_2 to evaporate at higher temperature due to reaction equations (4.2), (4.4) and (4.5).

However, it is also interesting to see that EDS detects the carbon. The possible reason is the decomposition of SiC, since it is unable to oxidize fast enough under rapid cooling non-equilibrium conditions. Another potential possibility is the detection of CO and/or CO_2 gases trapped inside during the rapid solidification of the liquid borosilicate glass. Meanwhile, the Zr element is detected primarily due to the existence of ZrO_2 particulates that are embedded inside the SiO_2-rich glass layer (cf. Figure 4.5(B)) but this Zr can be in the form of oxides which is B and O. A slight shoulder peak of boron element also spotted next to carbon element in the EDS analysis. It might contribute to the crystallized B_2O_3 that are discussed further in the XRD diffraction analysis.

Figure 4.7(B) indicates the EDS analysis of the middle layer. It reveals the similar elements as in the top layer. Nevertheless, despite the presence of B, C, O and Si elements, it is detected in a degrade peak, in contrast to the Zr element. In the presence of greater Zr peak, it suggests that the layer is dominant of ZrO_2 particulates and a minority of SiO_2. It is most likely that the presence of C element is due to the remaining trapped gaseous and decomposition of SiC from the effect of rapid cooling. Probably, it might also be residual from the unreacted starting materials.

As revealed in Figure 4.4(B), it shows a loose porous structure if compared to the previous layers, and the starting material. EDS spectrum of Figure 4.7(C) for this third layer represents principally Zr and B. The Zr and B elements are detected as a boron element from ZrB_2 that are unoxidized and slight O element, which comes from ZrO_2 particulates. Beneath the multilayer structure, the unaffected ZrB_2-SiC structure can be observed. The overall EDS analysis in Figure 4.7 pointed out to the transition of Si, O, C, Zr and B peaks at each layer that affected due to the oxidation.

(A)

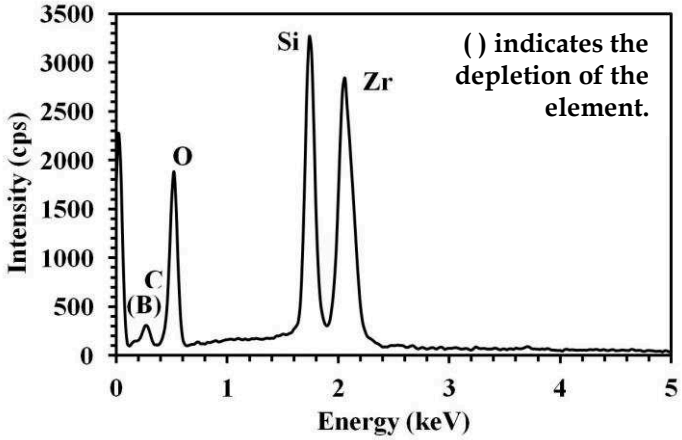

(B)

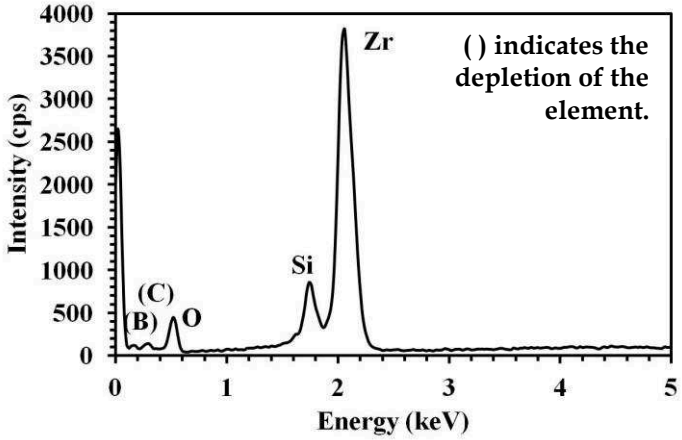

(C)

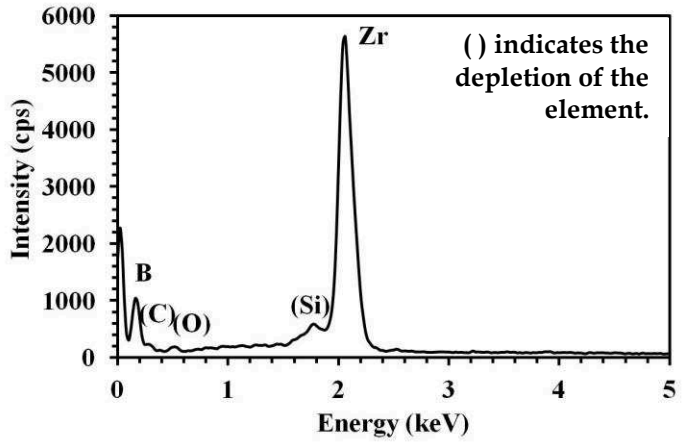

Figure 4.7: EDS analysis for the multilayer structure of ZrB_2-SiC fractured cross-section in Figure 4.4(B). (A) Top layer, (B) Middle layer and (C) Third layer.

The existence of a glassy layer is also supported by the X-ray diffraction pattern as shown in Figure 4.8. It shows the XRD patterns of the sample surface layer, before and after laser treatment. Majority of sharp and high intensity of diffraction peaks is assigned to ZrB_2, and minor, small, sharp and low intensity peaks of SiC are clearly identified before laser treatment. After laser treatment, the X-ray diffraction displays various crystalline peaks presence and evidently displays a very broad hump between angle at 2θ = 15° and 35° due to the presence of thin amorphous SiO_2-rich glass layer. The diffraction peaks of oxide also appear, that composed of crystallized ZrO_2. These crystallized ZrO_2 is mainly present in monoclinic form and at ≈ 30° angle, ZrO_2 tetragonal form is also detected.

Peaks showing crystallized B_2O_3 are also present at peak of 15° and in between the angle of ≈ 28° to 45°. From the practical point of view, these peaks are formed due to the evolution of gaseous B_2O_3, during laser treatment. Throughout laser oxidation, the B_2O_3 vaporized once exposes to high temperatures, and this occurs at the irradiation of a laser beam. However, it happens that the B_2O_3 also easily condensates at the coldest part around the irradiated laser zone. This phenomenon explains the presence of crystallized B_2O_3 peaks. A comparable mechanism has been reported by Goutier et al. (2011) and Gao et al. (2013). In addition, part of ZrB_2 and SiC peaks are still observable due to the thin thickness of the oxide layer. Some unidentified peaks are also found in the diffractogram that is unexplainable.

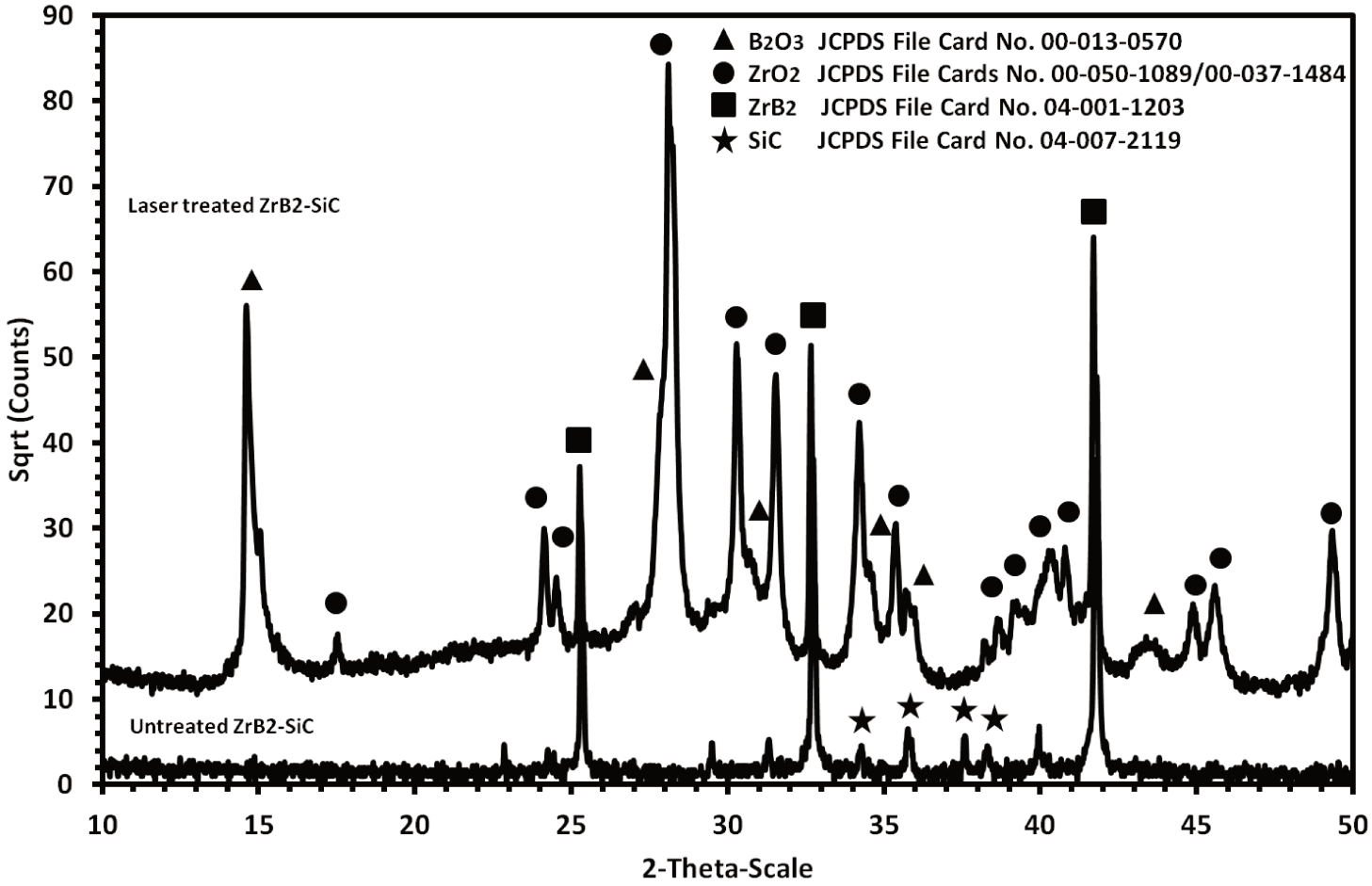

Figure 4.8: XRD pattern of ZrB_2-SiC composites before and after laser treatment (70 W).

4.2 Summary

An investigation into the oxidation behaviour of ZrB_2-SiC ceramic composite surface-treated through continuous-wave ytterbium fibre laser under an ambient atmosphere was conducted. The laser-treated pellets were characterized for their structural and morphological properties. Laser surface oxidation was achieved uniformly at a laser power of 70 W. The following conclusions can be drawn:

a) Laser surface treatment with a desirable spiral pattern onto the porous ZrB_2-SiC ceramic composite substrate resulted in a uniform glassy layer about 8 μm thick. This layer is continuous and protects further oxidation of the bulk ceramic composite. The porous composite remains unaffected only a few microns below the glassy layer.

b) The SEM study of the cross section of treated samples reveals the formation of a multilayer structure. Beneath the glassy layer there are two layers which have been affected by the surface treatment. EDS study demonstrates that Si gets depleted in the layers beneath the glassy layer.

c) Beneath the multilayer structure of oxidized ZrB_2-SiC, a well-preserved ZrB_2-SiC morphology was observed. This remarkable microstructure verifies the high-localized heat treatment by laser. Interestingly, the laser pattern can be customized and can be employed in various applications.

The present study represents an alternative option of oxidation process for ceramic materials and opens the possibility of developing new laser patterns for various types of ceramics specifically for surface modifications. Although the laser-treated of ZrB_2-SiC at 70 W exhibited a glassy layer, the cracks can be observed in Figure 4.5 under high magnification of the SEM. The cracks obviously will impact on the efficiency of the cell system as gas leaking will occur. The observation of fine cracks lead to the further study on the sintered structure of ZrB_2-SiC at a higher sintering temperature of 2100 °C to improve the densification of ZrB_2-SiC.

The Chapter 5 discusses on the further study of sintered ZrB_2-SiC at a higher temperature. It was conducted to reduce the crazing effect in the attempt to improve laser scanning surface. One of the possibilities was to increase the sintering temperature.

CHAPTER 5

An Evaluation of Zirconium Diboride-Silicon Carbide (ZrB_2-SiC) Ceramic Composites Sintered at 2100 °C

5.1 Results and Discussion

5.1.1 Pressureless Sintering at 2100 °C

Pressureless sintering at 2100 °C was performed on 100Z, 90Z10S, 85Z15S and so on (Refer to Table 2.3). The densities of sintered pellets were obtained and analysed. The percentage of experimental/theoretical density ratios versus SiC composition are presented in Figure 5.1. The theoretical densities were obtained from the law of mixtures. For example, $0.9\rho_{ZrB_2} + 0.1\rho_{SiC} = 5.8977$ g/cm^3. Meanwhile, the experimental densities were obtained by measuring the mass (m), diameter (d), thickness (t) and area (A) of the sintered pellets. Then, the densities (ρ) were calculated using the formula: $\rho = \frac{m}{V}$. The densification behaviour was investigated through the analysis of the plotted density.

As can be seen in Figure 5.1, the increase of density was expected in parallel of increment of SiC additive. However, the fall of density was observed at 20 mol.% SiC (80Z20S) and increased again up till to 30 mol.% SiC. The fall of density at 20 mol.% SiC had raised a question that something had caused the decreased density. As reported by the previous researcher, the SiC addition of 20 to 30 vol.% improves the densification of ZrB_2 (Chamberlain et al., 2004; Neuman et al., 2013; Neuman et al., 2015; Wang et al., 2009; Zhang et al., 2009b) and this result can be seen in contradiction of other studies. Nevertheless, the densification of 70Z30S was favourable and achieved the highest relative density, ~ 96%. It was still in agreement with reported studies which exhibited relative density approximately ~ 95% relative density via pressureless sintering (Fahrenholtz et al., 2008; Mashhadi et al., 2015; Wang et al., 2009; Zhang et al., 2009b). To further investigate the cause and clarify the reason of decreased density, the SEM-EDS were performed to observe the morphology of sintered ZrB_2-SiC and identify the presence of other elements that might be an extraordinary.

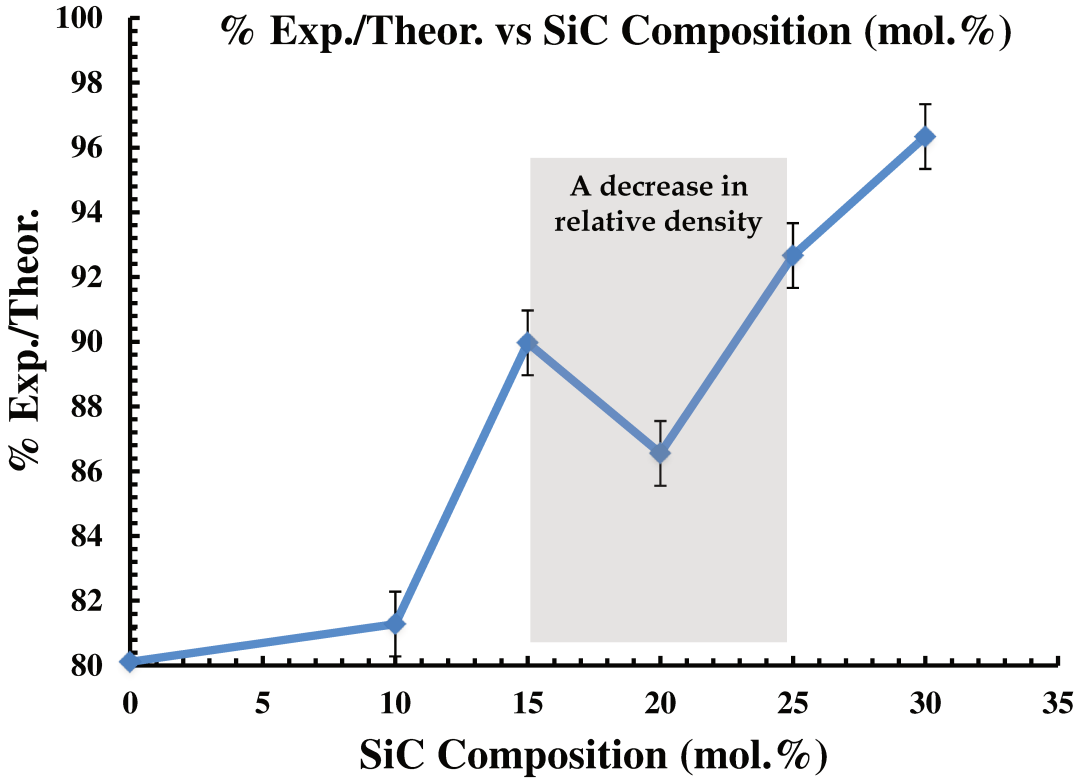

Figure 5.1: Percentage of experimental/theoretical density measurement of sintered pellet versus SiC composition (mol.%).

5.1.2 Microstructures and XRD analysis

All selected SEM micrographs in the Secondary Electron (SE) mode are presented in Figure 5.2(A) to (F). SEM micrographs indicate the typical structure of ZrB_2-SiC ceramic composites in agreement with the previous studies (Hwang et al., 2007; Lü et al., 2011; Neuman et al., 2013; Neuman et al., 2015; Sai Krupa et al., 2013; Wang et al., 2009; Zhang et al., 2009b; Zhu et al., 2009). In general, the light shaded phase is identified as ZrB_2 grains, and dark phase is cylindrical SiC grains. Also, there are few cuboidal darker grains, which can be seen in Figure 5.2(D) to (F). Since pressureless sintering was employed in the study, the existence of residual porosity was as expected and can be observed in the micrographs. From Figure 5.2(A) to (C), the porosities were reduced, and the densities increased function to increase of SiC concentration which proved that the addition of SiC improved the densification of ZrB_2. The pure ZrB_2 sample exhibited highest porosity (around 20%) whereas lowest porosity was observed in the 70Z30S sample (approximately 5%).

However, the 80Z20S in Figure 5.2(D), exhibited slightly higher porosity compared to 75Z25S in Figure 5.2(E). It is in parallel of early detection of the decrease in density as presented in Figure 5.1. In addition, there was an existence of cuboidal grains observed in Figure 5.2(D) to (F). Overall, the EDS analysis did not exhibit other than typical elements that can be observed in SEM micrographs as shown in Figure 5.2. These elements were Zr, B, Si, and C. A small amount of oxygen (O) was also detected, as partial oxidation in non-oxide ceramics. Avoiding the occurrence of little oxidation is difficult.

Because of the EDS elemental analysis did not feature any other element, the much darker grains were suspected to be boron carbide (B_4C). To further track the impact of changes due to the cuboidal shape grains appearance, the Si/Zr ratio obtained by EDS as a function of SiC composition (mol.%) is plotted to confirm and understand the behaviour of fall in the density at 20 mol.% SiC.

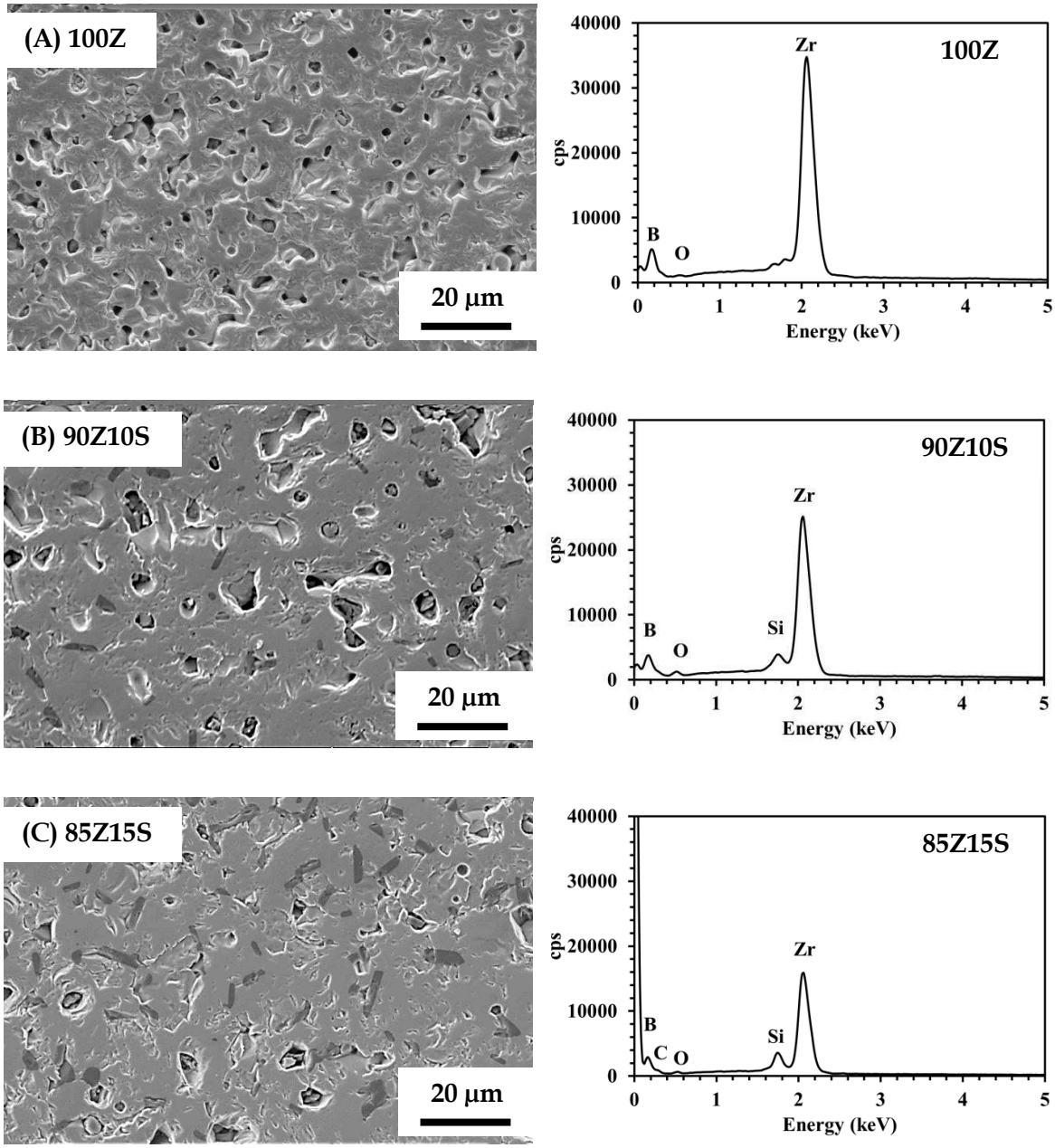

Figure 5.2: SEM micrographs in secondary electron. (SE) mode and EDS spectrums of sintered pellets at 2100 °C (1000×). (A) 100Z, (B) 90Z10S, (C) 85Z15S, (D) 80Z20S, (E) 75Z25S and (F) 70Z30S.

Figure 5.2 continued.

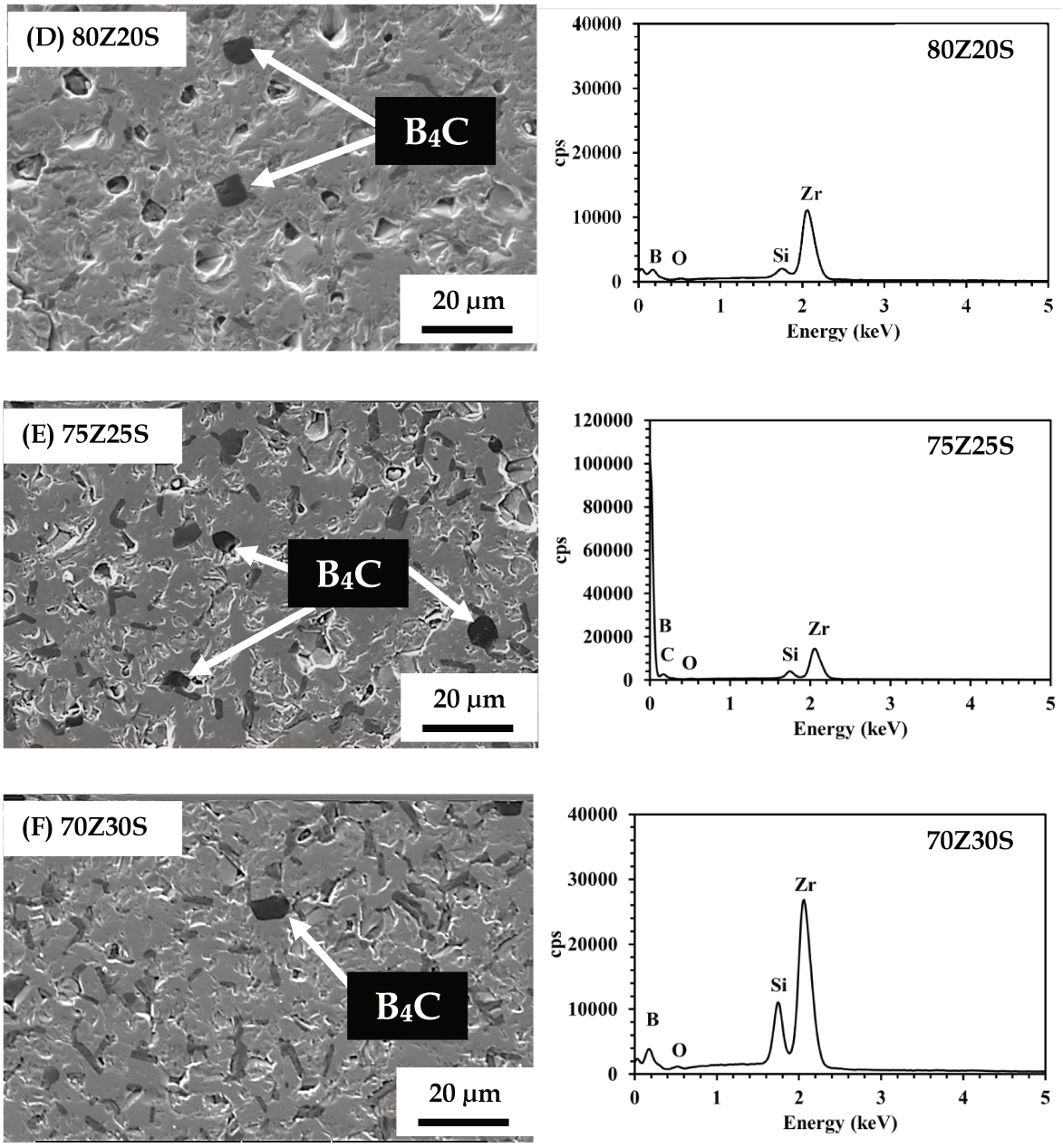

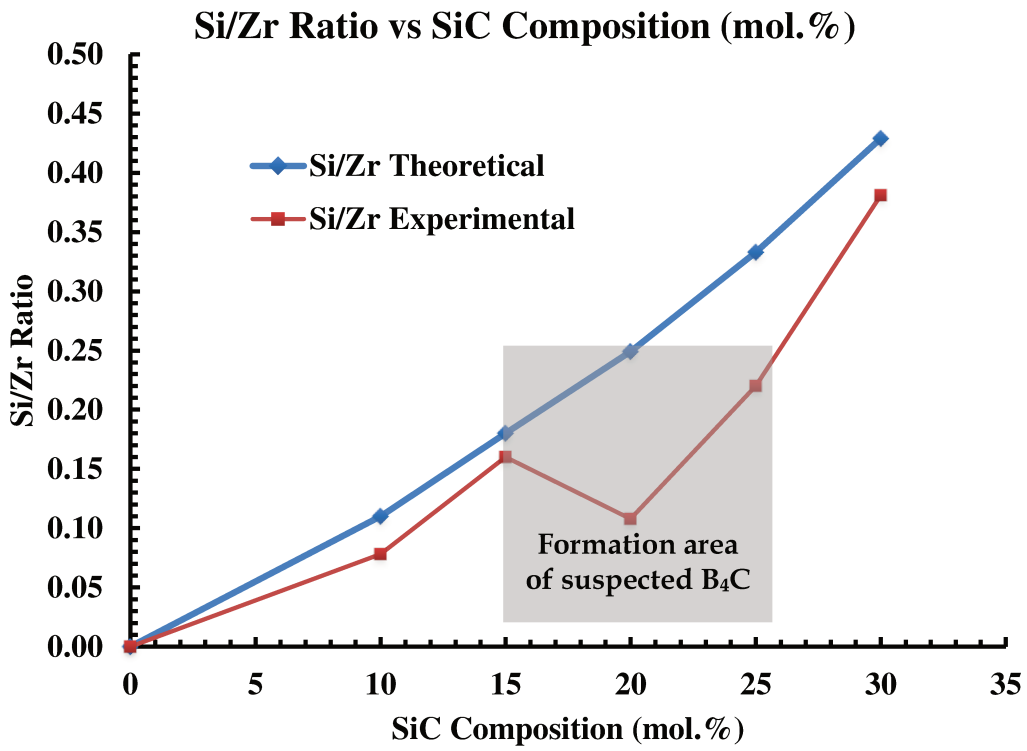

Figure 5.3: Si/Zr ratio obtained by EDS as a function of SiC composition (mol.%).

The Si/Zr ratio as a function of SiC composition obtained from EDS as shown in Figure 5.3 was also plotted to demonstrate these changes. Both graphs clearly illustrate changes occurring in the sample 80Z20S. Figure 5.1 shows the fall of density was apparently seen at 20 mol.% SiC. The density decreased from approximately 90% of the sample with 15 mol.% SiC to 86% at 20 mol.% SiC. In Figure 5.3, the theoretical and experimental Si/Zr ratio obtained through EDS curves exhibit a difference of about 56% for the 80Z20S sample.

Further analysis of phases was performed through XRD to verify the presence of B_4C compounds. The results are presented in Figure 5.4. Surprisingly, the detection of B_4C peaks can be obviously observed in 80Z20S sample, but not for other samples that also indicates the cuboidal shape grains in the earlier seen in SEM micrographs (Figure 5.2).

The B_4C phase can be found in at least one sample with 20 mol.% SiC (80Z20S). As reported by Harrington et al. (2013), who added carbon in ZrB_2 for the densification purpose, the formation of B_4C can take place if the carbon concentration in the ceramic is more than 0.75 wt.%. In the present study, carbon was not added to the initial powder mixture, and the only

probable reason behind the presence of B_4C was the carbon which can result from a reaction between ZrB_2 and SiC. The present study also demonstrated that the presence of 20 mol.% SiC in the mixture produced the most amount of B_4C, which was also detectable in the XRD spectra. Meanwhile, Dole et al. (1989) have studied the sintering of B_4C in a pure state as well as with the addition of 6 wt.% C and have observed that the presence of carbon can improve the densification.

Figure 5.4 displays the XRD patterns of pressureless sintered ZrB_2-SiC with various compositions. Apparently, it represents the dominating compounds such as ZrB_2 and SiC and in good agreement with SEM micrographs earlier. Meanwhile, the cuboidal darker grains that were predicted to be B_4C initially can also be observed at 20 mol.% SiC (80Z20S), several B_4C peaks were noted in the XRD analysis. This analysis validated the presence of B_4C peaks whereas, for other composition of SiC, the B_4C were undetectable. The reason might be due to insufficient amount of B_4C formation in the samples compared to 80Z20S.

From the point of view, the reaction might start at 15 mol.% SiC (85Z15S) due to decreasing peaks for SiC which observed in Figure 5.4. However, the decomposition of carbon from SiC was insufficient to develop B_4C. As reported by Harrington et al. (2013), the carbon addition would also contribute to the development of B_4C. Nevertheless, the carbon addition was not added. The only probable reason behind the presence of B_4C was from ZrB_2 and SiC. Therefore, at 20 mol.% SiC was the optimum for B_4C to be produced in a big amount and can be detected by XRD.

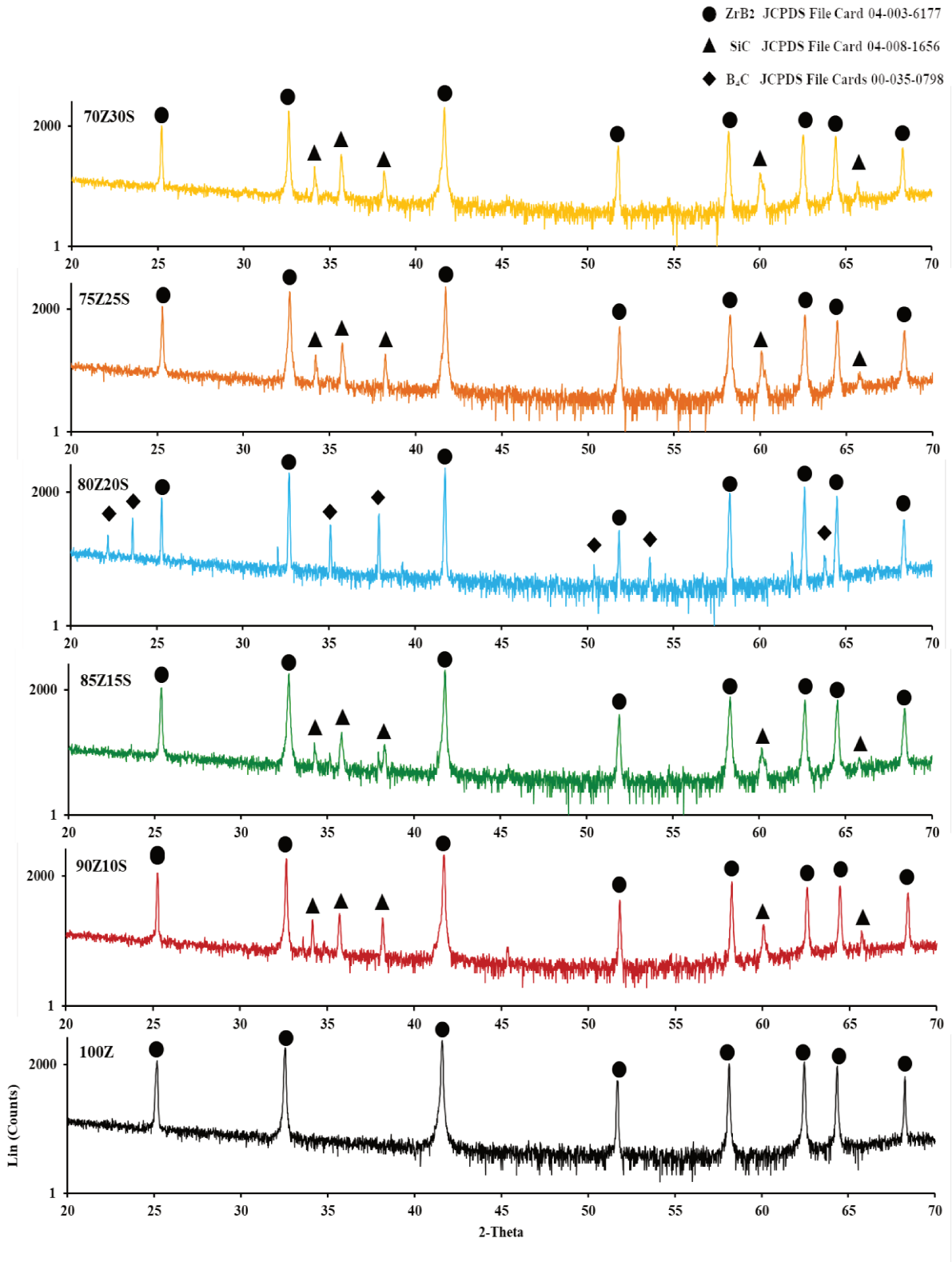

Figure 5.4: XRD patterns of pressureless sintered ZrB2-SiC at 2100 °C at 100Z, 90Z10S, 85Z15S, 80Z20S, 75Z25S and 70Z30S compositions.

5.1.3 Thermodynamic Analysis

The thermodynamic analysis was performed to figure out the possible reactions that might occur and contribute to the formation of B_4C. Since the pressureless sintering conducted at 2100 °C, the volatility diagram at 2400 K ≈ 2126.85 °C was chosen to be analysed.

Figure 5.5 and Figure 5.6 represent the volatility diagram of SiC-O_2 and ZrB_2-O_2 at 2400 K, respectively. The volatility diagrams are the thermodynamics representations to provide the gaseous and condensed species formed during oxidation of the materials at a given temperature. Both diagrams were constructed to relate the decomposition of SiC and ZrB_2 in the contribution of the B_4C formation.

JANAF thermodynamics tables are used to explain the construction of SiC and ZrB_2 volatility. These diagrams were plotted at 2400 K as this temperature was employed during the furnace sintering to demonstrate the possibility of how the B_4C can be formed from the decomposition of SiC.

Table 5.1, the Log K_i that is the decimal logarithms of their equilibrium constants at 2400 K summarized for each reaction considered. For each reaction, the partial pressure of the type of the volatile species formed the $Si_xC_yO_z$ that can be written as Equation 5.1 (Lonné 2011):

$$\text{Log } P_{SixCyOz} = a \text{ Log } P_{O2} + b \text{ Log } K_i + \text{constant} \qquad (5.1)$$

Table 5.2 is the list of the decimal logarithms of their equilibrium constants, Log Ki at 2400 K. For each reaction, the partial pressures of the volatile species $Zr_xB_yO_z$ formed can be expressed in an equivalent way to Equation 5.1 and written as Equation 5.2 (Lonné 2011):

$$\text{Log } P_{ZrxByOz} = a \text{ Log } P_{O2} + b \text{ Log } K_i + \text{constant} \qquad (5.2)$$

The reference pressure is equal to 10^5 Pa.

Table 5.1: Reactions considered during the oxidation of SiC and their equilibrium constants at 2400 K (Chase 1998; Lonné 2011).

Reactions	Log K_i
	2400 K
1) $SiC\ (s) + 1.5\ O_2 \rightarrow SiO_2\ (l) + CO\ (g)$	16.593
2) $SiC\ (s) + O_2 \rightarrow SiO\ (g) + CO\ (g)$	12.242
3) $SiC\ (s) + 0.5O_2 \rightarrow Si\ (g) + CO\ (g)$	3.603
4) $SiC\ (s) \rightarrow Si\ (g) + C\ (s)$	-3.433
5) $2SiO_2\ (l) \rightarrow 2SiO\ (g) + O_2$	-8.702
6) $SiO_2\ (l) \rightarrow SiO_2\ (g)$	-4.116
7) $SiO\ (g) + 0.5O_2 \rightarrow SiO_2\ (g)$	0.235
8) $Si\ (g) + 0.5O_2 \rightarrow SiO\ (g)$	8.639
9) $2C\ (s) + O_2 \rightarrow 2CO\ (g)$	13.892

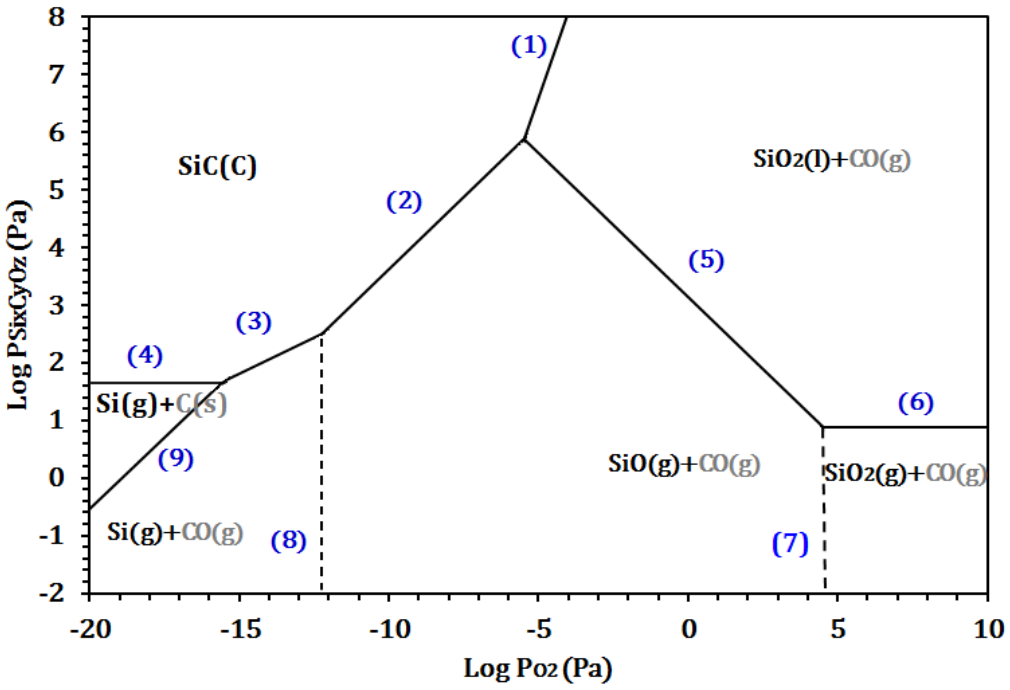

Figure 5.5: Volatility diagram of SiC-O_2 system at 2400K (Lonné 2011).

Table 5.2: Reactions considered during the oxidation of ZrB_2 and their equilibrium constants at 2400 K (Chase 1998).

Reactions	Log K_i 2400 K
10) ZrB_2 (s) + 2.5O_2 → ZrO_2 (s) + B_2O_3 (l)	24.240
11) ZrB_2 (s) + 2.5O_2 → ZrO_2 (s) + B_2O_3 (g)	24.400
12) ZrB_2 (s) + 2O_2 → ZrO_2 (s) + B_2O_2 (g)	19464
13) ZrB_2 (s) + 2O_2 → ZrO_2 (s) + 2BO (g)	17.680
14) ZrB_2 (s) + O_2 → ZrO_2 (s) + 2B (g)	-0.544
15) B_2O_3 (l) → B_2O_3 (g)	0.205
16) B_2O_3 (l) + 0.5O_2 → 2BO_2 (g)	-1.508
17) B (g) + 0.5O_2 → BO (g)	9.112
18) ZrB_2 (s) + 2BO (g) + 2O_2 → ZrO_2 (s) + 2B_2O_2 (g)	21.248
19) B_2O_2 (g) + 0.5O_2 → B_2O_3 (g)	4.981
20) 2B_2O_3 (g) + 0.5O_2 → 2BO_2 (g) + B_2O_3 (l)	-1.918

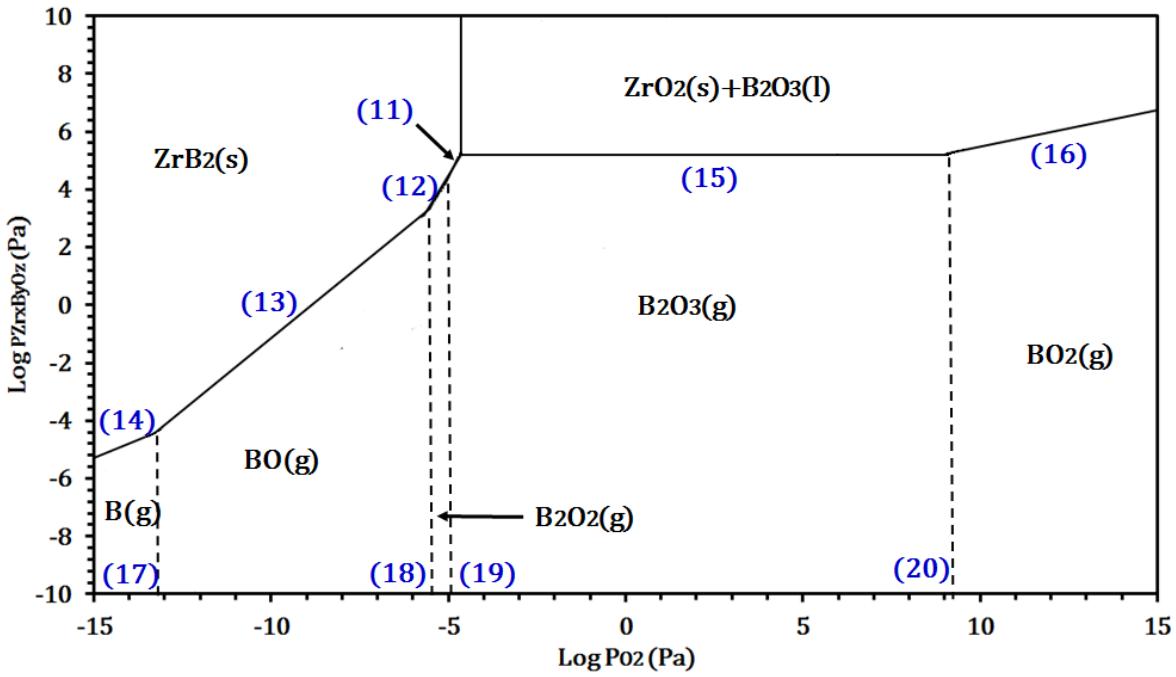

Figure 5.6: Volatility diagram of ZrB_2-O_2 system at 2400 K (Lonné 2011).

As already known, the overall reaction of B_4C preparation is in Equations (5.3) - (5.10) (Thévenot 1990):

$$2B_2O_3(g) + 7C(s) \rightarrow B_4C(s) + 6CO(g) \qquad (5.3)$$

The reaction normally takes place in two stages:

$$B_2O_3(g) + 3CO(g) \rightarrow 2B(c) + 3CO_2(g) \qquad (5.4)$$

$$4B(c) + C(c) \rightarrow B_4C(s) \qquad (5.5)$$

In the present work, the formation of B_4C might be probably due to the extremely low oxygen partial pressure and high porosity at the beginning of the reaction. The B_4C is possible to form in the environment of low oxygen partial pressure. It can be shown in Figure 5.5 and Figure 5.6 whereby the carbon and boron are present in low oxygen partial pressure environment.

In addition, the reaction tendency of B_4C was probably due to the approach of pressureless sintering at 2100 °C, itself. Initially, the pellet appeared to be low densified and high residual porosity. The high amount of residual porosity would perhaps create the low oxygen partial pressure environment in the pellets themselves. It would lead to the volatilization of B_2O_3 and condensate as boron. The boron might react with the carbon that came from the decomposition of SiC which resulted in the formation of B_4C (Equations 5.3 and 5.10). With one condition that boron and carbon elements were sufficient to react with each other. In this work, it occurred at 20 mol.% SiC.

Some of the following reactions are proposed for the ZrB_2-SiC system:

$$ZrB_2(s) + 2.5O_2(g) \rightarrow ZrO_2(s) + B_2O_3(l) \quad (5.6)$$

$$SiC(s) + O_2(g) \rightarrow CO(g) + SiO(g) \quad (5.7)$$

$$SiC(s) \rightarrow Si(g) + C(s) \quad (5.8)$$

$$2B_2O_3(g) + 7C(s) \rightarrow B_4C(s) + 6CO(g) \quad (5.9)$$

$$ZrO_2(s) + B_2O_3(g) + 5C(s) \rightarrow ZrB_2(s) + 5CO(g) \quad (5.10)$$

5.2 Summary

The laser treatment of sintered ZrB_2-SiC and TiB_2-SiC ceramic composites was performed. The ZrB_2-SiC and TiB_2-SiC were sintered at 1900 °C before going through the laser treatment. Although, the sintered ZrB_2-SiC exhibited better laser results compared to the sintered TiB_2-SiC yet some fine cracks were found under high magnification of the SEM. Initial SEM characterization of sintered ZrB_2-SiC at low magnification was unable to observe the fine cracks only crazing effects were observed.

To further investigate the ZrB_2-SiC substrates, the ZrB_2 ceramics containing up to 30 mol.% SiC were densified by pressureless sintering at 2100 °C without any sintering aids. The aim to conduct the sintering at higher temperature was to improve the sinterability and structural properties. The sintered ZrB_2-SiC at 2100 °C demonstrated high densification up to ± 96% for 30 mol.% SiC addition but at 20 mol.% SiC demonstrated the decrease of density. Generally, the ZrB_2 increased in the density with the increase of SiC addition. Nevertheless, at 20 mol.% SiC addition displayed a fall of density. Observation of SEM images revealed the presence of darker cuboidal grains. It was further analysed by EDS and XRD. It concluded that the darker grains were B_4C.

To the best of knowledge, it was the first-time discovery of B_4C in the sintered ZrB_2-SiC at the sintering temperature of 2100 °C by pressureless sintering and without any sintering aids. Previous research typical employed B_4C as an additive or sintering aid (Ma et al., 2015; Neuman et al., 2015; Zhang et al., 2009a). Besides, the B_4C was formed typically in the presence of carbon and oxygen (Harrington et al. 2013).

An interest of unexpected B_4C presence in the sintered ZrB_2-SiC prepared by pressureless sintering at 2100 °C was investigated. A thermodynamic study was performed to propose the possible reactions of the B_4C formation. It was concluded that the optimum composition for the B_4C formation was at 20 mol.% SiC addition. Furthermore, the ZrB_2-SiC sintered pellet structure should possess low densification with high residual porosity at the initial during the sintering. This type of structure would create the environment of low oxygen partial pressure inside the pellet during the sintering process at 2100 °C. Furthermore, the boron decomposition from ZrB_2 and carbon decomposition from SiC should also be sufficient to form B_4C. Conclusively, this study may trigger the potential of developing B_4C by pressureless sintering. Despite the presence of intrusion B_4C, the sinterability properties were improved for sintered 70 mol.% ZrB_2-SiC. It exhibited approximately 96% density by pressureless sintering.

CONCLUSIONS

The research on the porous non-oxide ZrB_2-SiC and TiB_2-SiC ceramic composites sintered at 1900 °C and after laser treatment demonstrated various remarkable results. It can be summarized as follows:

a) The cold-pressing of 61 mol.% ZrB_2-SiC (61Z39S) and 61 mol.% TiB_2-SiC (61T39S) ceramic composites followed by pressureless sintering at 1900 °C resulted in a porosity of ca. 29% and the error was ± 0.01. The specific importance of our work was that this density was obtained without any sintering additives.

b) Laser treatment was performed onto the surface of sintered 61Z39S and 61T39S ceramic composites at different laser power, scanning rate, reduced beam diameter and a round spiral laser pattern. It was found that 61Z39S ceramic composites exhibited a glassy surface layer with a round spiral laser track at 70 W laser power. 61T39S ceramic composites developed bubbles on the surface and distinct cracks when treated at the laser power of 60 W and scanning rate of 1 mm/s.

c) It was decided that 61Z39S ceramic composites are a better option for the protonic conducting fuel cell due to the present work exhibited feature of a glassy surface by laser and the previous study of Lonné (2011) that obtained 2 $mScm^{-1}$ (25 °C) conductivity of 61Z39S.

d) The in-depth structural study on the cross-section of 61Z39S ceramic composites treated at 70 W laser power under the SEM revealed that the formation of a multi-layer and unaffected bulk structure. The multi-layer structures were comprised of a SiO_2 glassy layer with dissolved ZrO_2 on the top layer, the second layer contained high-concentration of ZrO_2 and SiO_2, the third layer was ZrB_2-rich and SiC-depleted with little ZrO_2. The bulk was composed of the preserved ZrB_2-SiC structures.

e) At higher magnification of SEM micrographs of 61Z39S ceramic composites treated at 70 W laser power, a continuous glassy was observed to have cracks. It was difficult to notice whether the fine cracks were interconnected or not. It was concluded that this effect can be improved by sintering the 61Z39S ceramic composites at higher temperatures and thus with lower porosity to increase the densification and to improve the 61Z39S properties.

The subsequent conclusions are based on the research conducted on the sintering of ZrB_2-SiC ceramic composites at 2100 °C by pressureless sintering with different SiC compositions. The following conclusions can be drawn:

a) At 2100 °C sintering temperature, a higher densification of ZrB_2-SiC ceramic composites was achieved (approximately 96%) compared to the density obtained when sintering at 1900 °C which achieved only 71% densification.
b) The SEM results showed the presence of darker and cuboidal shaped grains in addition to the regular grains structure of ZrB_2 and SiC for the morphological structure of ZrB_2-SiC ceramic composites sintered at 2100 °C. These grains were absent in the microstructure of ZrB_2-SiC sintered at 1900 °C. Further analysis using XRD exposed the B_4C peaks attributed to this cuboidal phase. As reported in the previous section of this conclusion, a higher densification of 96% obtained for these ceramics can also be the result of this simultaneous formation of B_4C phase during the sintering at 2100 °C.
c) It was strongly believed that B_4C formation took place during the pressureless sintering of ZrB_2-SiC at 2100 °C due to low oxygen partial pressure and high porosity of sample in the beginning of the sintering process.
d) In the study of thermodynamic aspect, the volatility diagrams of SiC-O and ZrB_2-O were constructed and investigated. Several reactions have been recommended for the formation of B_4C at the 2100 °C sintering temperature.

Challenges throughout the Research Work

A few crucial challenges of the current work are highlighted as below:

a) The stability of SiO_2 glassy layer had not been studied thoroughly to ensure its function as a protonic conducting electrolyte for the fuel cell system. It was because of the crazing effects (the phenomenon that produces a network of fine cracks on the surface of a material) on the surface of ZrB_2-SiC ceramic composites.
b) Although the TiB_2-SiC ceramic composites did not demonstrate a positive result when treated with 60 W laser beam, it was suggested that a different laser power with a different scanning pattern and scanning rate can be applied for this system.
c) A controlled atmosphere during the laser treatment of all the sintered samples was not utilized due to the fact that our laser treatment was also conducted for oxidizing the sample surface. A controlled atmosphere laser treatment can be envisaged in future.

Recommendations for Future Work

Further research is necessary to shed more light on the present work. The following recommendations are for future work in the field of fuel cell technology.

a) A simulation study of the different laser power properties, various beam diameters, scanning rates and different environment on the ceramic composites is recommended to be carried out. The purpose is to investigate the different laser parameters configuration available as it would predict the power properties at various levels. It would provide a powerful tool for a preliminary study that might minimize the samples/specimens loses at the experimental level.
b) Further investigation on the sintered ZrB_2-SiC and TiB_2-SiC ceramic composites comprised of higher densification at higher laser power (above 100 W) is recommended to be conducted to accommodate precise parameter estimation for promoting a complete and favourable thickness of glassy layer feature.

REFERENCES

Andujar, J.M. & Segura, F., 2009. Fuel cells: History and updating. A walk along two centuries. *Renewable and Sustainable Energy Reviews*, 13(9), pp.2309–2322.

Ang, C. et al., 2013. Modification of ZrB_2 powders by a sol–gel ZrC precursor—A new approach for ultra high temperature ceramic composites. *Journal of Asian Ceramic Societies*, 1(1), pp.77–85.

Appetecchi, G.B. et al., 2003. Hot-pressed, dry, composite, PEO-based electrolyte membranes: I. Ionic conductivity characterization. *Journal of Power Sources*, 114(1), pp.105–112.

Aygun, G. et al., 2004. Oxidation of Si surface by a pulsed Nd : YAG laser. *Journal of Physics D: Applied Physics*, 37(11), pp.1569–1575.

Bacciochini, A., Glandut, N. & Lefort, P., 2009. Surface densification of porous ZrC by a laser process. *Journal of the European Ceramic Society*, 29(8), pp.1507–1511.

Badwal, S.P.S. & Foger, K., 1996. Solid Oxide Electrolyte Fuel Cell Review. *Ceramics International*, 22(95), pp.257–265.

Beauvais-Réveillon, S. et al., 1995. Comparison of classical oxidation and laser oxidation of a chromium PVD coating on a pure-iron substrate. *Oxidation of Metals*, 43(3–4), pp.279–300.

Bechstedt, F. & Belabbes, A., 2013. Structure, energetics, and electronic states of III-V compound polytypes. *Journal of physics. Condensed matter : an Institute of Physics journal*, 25(27), p.273201.

Blokhina, I. a. & Ivanov, V. V., 2014. Analysis of TiB_2 powders oxidation in the air. *Journal of Thermal Analysis and Calorimetry*, 119(1), pp.123–130.

Boutinguiza, M. et al., 2013. Synthesis of Titanium Oxide Nanoparticles by Ytterbium Fiber Laser Ablation. *Physics Procedia*, 41, pp.787–793.

Buyakova, S. et al., 2016. The influence of ZrB_2-SiC powders mechanical treatment on the structure of sintered ceramic composites. *IOP Conference Series: Materials Science and*

Engineering, 140, p.12006.

Canada, N.R.C., 2011. Cathode Materials for Low Temperature Solid Oxide Fuel Cells. *Institute for Fuel Cell Innovation*, pp.3–4.

Casalino, G., Mortello, M. & Campanelli, S.L., 2015. Ytterbium fiber laser welding of Ti6Al4V alloy. *Journal of Manufacturing Processes*, 20, pp.250–256.

Chamberlain, A.L. et al., 2004. High-Strength Zirconium Diboride-Based Ceramics. *Journal of the American Ceramic Society*, 87(6), pp.1170–1172.

Chamberlain, A.L., Fahrenholtz, W.G. & Hilmas, G.E., 2006. Pressureless sintering of zirconium diboride. *Journal of the American Ceramic Society*, 89(2), pp.450–456.

Chao, S., Goldsmith, J. & Banerjee, D., 2015. Titanium diboride composite with improved sintering characteristics. *International Journal of Refractory Metals and Hard Materials*, 49(1), pp.314–319.

Chase, M.W., 1998. NIST-JANAF Thermochemical Tables, 4th Ed. J. Phys. Chem. Ref. Data. 1998, Monograph 9(Part I and Part II). *Journal of Physical and Chemical Reference Data*, Monograph, p.Part I&II.

Choi, S.M. et al., 2013. Fabrication and characterization of $Ba(Zr_{0.84}Y_{0.15}Cu0.01)O_{3-\delta}$ electrolyte-based protonic ceramic fuel cells. *Ceramics International*, 39(8), pp.9605–9611.

Christof M. Stotko, 2009. Laser Sintering Layer By Layer. *Nature Photonics*, 3(May), pp.265–266.

CLEFS CEA -No.50/51, 2005. SOFC high-temperature fuel cells. *Winter 2004-2005*, (50), pp.87–92.

Cook, B. & Heliocentris, 2001. *An Introduction to Fuel Cells and Hydrogen Technology*, Vancouver Canada.

Coors, W.G., 2003. Protonic ceramic fuel cells for high-efficiency operation with methane. *Journal of Power Sources*, 118(1–2), pp.150–156.

Cui, C.Y. et al., 2015. Novel morphologies and growth mechanism of Cr_2O_3 oxide formed on stainless steel surface via Nd: YAG pulsed laser oxidation. *Journal of Alloys and*

Compounds, 635, pp.101–106.

Dahotre, N.B. & Harimkar, S.P., 2008. *Laser Fabrication and Machining of Materials*, Springer Science + Business Media, LLC.

Dayton, D.C., Ratcliff, M. & Bain, R., 2001. *Fuel Cell Integraton - A Study of the Impacts of Gas Quality and Impurities*,

Demirskyi, D. et al., 2013. Densification and grain growth during microwave sintering of titanium diboride. *Scripta Materialia*, 69(8), pp.610–613.

Dole, S.L., Svante Prochazka & Doremu, R.H., 1989. Microstructural Coarsening During Sintering of Boron Carbide. *Journal American Ceramic Society*, 72(6), pp.958–966.

Dong, Z.H., Peng, X. & Wang, F.H., 2015. Oxidation of a ZrB2 coating fabricated on Ta–W alloy by electrophoretic deposition and laser melting. *Materials Letters*, 148, pp.76–78.

Duan, C. et al., 2015. Readily processed protonic ceramic fuel cells with high performance at low temperatures. *Science*, 349(6254), pp.1321–1326.

Eakins, E., Jayaseelan, D.D. & Lee, W.E., 2011. Toward oxidation-resistant ZrB_2-SiC ultra high temperature ceramics. *Metallurgical and Materials Transactions A: Physical Metallurgy and Materials Science*, 42(4), pp.878–887.

Enerdata, 2016. Global Energy Statistical Yearbook 2016: Total Energy Consumption. *Enerdata*, pp.4–7.

Evans, W.K. et al., 2011. The simulations of tubular solid oxide fuel cells (SOFCs). *Chemical Engineering Journal*, 168(3), pp.1301–1310.

Fabbri, E. et al., 2012. Towards the next generation of solid oxide fuel cells operating below 600 °C with chemically stable proton-conducting electrolytes. *Advanced Materials*, 24(2), pp.195–208.

Fahrenholtz, W.G. et al., 2008. Pressureless Sintering of Zirconium Diboride: Particle Size and Additive Effects. *Journal of the American Ceramic Society*, 91(5), pp.1398–1404.

Fahrenholtz, W.G. et al., 2007. Refractory Diborides of Zirconium and Hafnium. *Journal of the American Ceramic Society*, 90(5), pp.1347–1364.

Fahrenholtz, W.G., 2007. Thermodynamic Analysis of ZrB_2-SiC Oxidation: Formation of a SiC-Depleted Region. *Journal of the American Ceramic Society*, 90(1), pp.143–148.

Fergus, J.W., 2006. Electrolytes for solid oxide fuel cells. *Journal of Power Sources*, 162(1), pp.30–40.

Fergus, J.W., 2006. Oxide anode materials for solid oxide fuel cells. *Solid State Ionics*, 177, pp.1529–1541.

Frontera, P. et al., 2010. Catalytic features of Ni/Ba-$Ce_{0.9}$-$Y_{0.1}$ catalyst to produce hydrogen for PCFCs by methane reforming. *International Journal of Hydrogen Energy*, 35(20), pp.11661–11668.

Fu, H. et al., 2010. Elastic and thermodynamic properties of ZrB_2: First principle study. *Physica B: Condensed Matter*, 405(3), pp.846–851.

Gao, Z.-H. et al., 2013. Effects of ZrB_2 and SiC dual addition on the oxidation resistance of graphite at 1600–2000°C. *Corrosion Science*, 76, pp.182–191.

Garche, J. & Ludwig, J., 2015. Applications of Fuel Cell Technology : Status and Perspectives. *The Electrochemical Society Interface*, pp.39–43.

Gawel, R., Przybylski, K. & Viviani, M., 2014. Chemical stability and electrical properties of $BaCe_{0.85}Y_{0.15}O_{3-\delta}$–$Ce_{0.85}Y_{0.15}O_{2-\delta}$ composite bulk samples for use as central membrane materials in dual PCFC–SOFC fuel cells. *Materials Chemistry and Physics*, 147(3), pp.804–814.

Ghosal, A., Manna, A. & Lall, A.K., 2014. Modelling of Ytterbium Fiber Laser parameters during micro machining of Al-15 wt%Al_2O_3-MMC. *Procedia Engineering*, 90, pp.704–709.

Gonzalez-Julian, J. et al., 2014. Enhanced oxidation resistance of ZrB_2/SiC composite through in situ reaction of gadolinium oxide in patterned surface cavities. *Journal of the European Ceramic Society*, 34(16), pp.4157–4166.

Gorte, R.J. & Vohs, J.M., 2009. Nanostructured anodes for solid oxide fuel cells. *Current Opinion in Colloid & Interface Science*, 14(4), pp.236–244.

Goutier, F., Glandut, N. & Lefort, P., 2011. Purification of hot-pressed ZrCO into ZrC by a laser treatment. *Journal of Materials Science*, 46(21), pp.6794–6800.

Guan, T. & Alvfors, P., 2015. An Overview of Biomass-fuelled Proton Exchange Membrane Fuel Cell (PEMFC) Systems. *Energy Procedia*, 75, pp.2003–2008.

Guerrero Moreno, N. et al., 2015. Approaches to polymer electrolyte membrane fuel cells (PEMFCs) and their cost. *Renewable and Sustainable Energy Reviews*, 52, pp.897–906.

Guo, S., 2014. Densification, microstructure, elastic and mechanical properties of reactive hot-pressed ZrB_2–ZrC–Zr cermets. *Journal of the European Ceramic Society*, 34(3), pp.621–632.

Guo, S.-Q., 2009. Densification of ZrB_2-based composites and their mechanical and physical properties: A review. *Journal of the European Ceramic Society*, 29(6), pp.995–1011.

Guo, W.-M. & Zhang, G.-J., 2010. Oxidation resistance and strength retention of ZrB_2–SiC ceramics. *Journal of the European Ceramic Society*, 30(11), pp.2387–2395.

Han, J. et al., 2007. Oxidation Behavior of Zirconium Diboride–Silicon Carbide at 1800°C. *Scripta Materialia*, 57(9), pp.825–828.

Harrington, G.J.K., Hilmas, G.E. & Fahrenholtz, W.G., 2013. Effect of carbon and oxygen on the densification and microstructure of hot pressed zirconium diboride. *Journal of the American Ceramic Society*, 96(11), pp.3622–3630.

He, R. et al., 2012. Aqueous gelcasting of ZrB_2–SiC ultra high temperature ceramics. *Ceramics International*, 38(7), pp.5411–5418.

Holland, B., Zhu, J. & Jamet, L., 2001. Fuel cell technology and application. *Proceedings of Australasian Universities Power Engineering Conference*.

Honma, T., Nguyen, P.T. & Komatsu, T., 2008. Crystal growth behavior in CuO-doped lithium disilicate glasses by continuous-wave fiber laser irradiation. *Journal of the Ceramic Society of Japan*, 116(1360), pp.1314–1318.

Hu, C. et al., 2010. Microstructure and properties of ZrB_2–SiC composites prepared by spark plasma sintering using $TaSi_2$ as sintering additive. *Journal of the European Ceramic Society*, 30(12), pp.2625–2631.

Hu, P., Guolin, W. & Wang, Z., 2009. Oxidation mechanism and resistance of ZrB_2–SiC composites. *Corrosion Science*, 51(11), pp.2724–2732.

Huang, J. et al., 2006. A high-performance ceramic fuel cell with samarium doped ceria–carbonate composite electrolyte at low temperatures. *Electrochemistry Communications*, 8(5), pp.785–789.

Huijsmans, J., 2001. Ceramics in solid oxide fuel cells. *Current Opinion in Solid State and Materials Science*, 5(4), pp.317–323.

Hwang, S.S., Vasiliev, A.L. & Padture, N.P., 2007. Improved processing and oxidation-resistance of ZrB_2 ultra-high temperature ceramics containing SiC nanodispersoids. *Materials Science and Engineering: A*, 464(1–2), pp.216–224.

IPG Photonics Corporation, 2016. Industrial Laser Solutions for Manufacturing. *PennWell*, p.31.

Ivanov, V. V., Blokhina, I.A. & Kirik, S.D., 2014. High-temperature oxidation kinetics of TiB_2 powders in air. *Oxidation of Metals*, 82(1–2), pp.71–84.

Iwahara, H. et al., 2004. Prospect of hydrogen technology using proton-conducting ceramics. *Solid State Ionics*, 168(3–4), pp.299–310.

Iwahara, H., 1995. Technological challenges in the application of proton conducting ceramics. *Solid State Ionics*, 77, pp.289–298.

Jan, P., 2014. Review article : Silicon Carbide . Structure , Properties and Processing. , pp.1–18.

Jayaseelan, D.D. et al., 2010. Laser modified microstructures in ZrB_2, ZrB_2/SiC and ZrC. *Journal of the European Ceramic Society*, 30(11), pp.2279–2288.

Jiang, S.P., 2012. Nanoscale and nano-structured electrodes of solid oxide fuel cells by infiltration: Advances and challenges. *International Journal of Hydrogen Energy*, 37(1), pp.449–470.

Jwad, T. et al., 2016. Laser induced single spot oxidation of titanium. *Applied Surface Science*, 387, pp.617–624.

Karlsdottir, S.N. & Halloran, J.W., 2009a. Formation of Oxide Films on ZrB_2-15 vol% SiC Composites During Oxidation: Evolution with Time and Temperature. *Journal of the American Ceramic Society*, 92(6), pp.1328–1332.

Karlsdottir, S.N. & Halloran, J.W., 2009b. Oxidation of ZrB_2 -SiC: Influence of SiC Content on Solid and Liquid Oxide Phase Formation. *Journal of the American Ceramic Society*, 92(2), pp.481–486.

Karlsdottir, S.N. & Halloran, J.W., 2007. Rapid Oxidation Characterization of Ultra-High Temperature Ceramics. *Journal American Ceramic Society*, 90(10), pp.3233–3238.

Karlsdottir, S.N., Halloran, J.W. & Grundy, A.N., 2007. Zirconia Transport by Liquid Convection during Oxidation of Zirconium Diboride-Silicon Carbide. *Journal of the American Ceramic Society*, 91(1), pp.272–277.

Kazemzadeh Dehdashti, M., Fahrenholtz, W.G. & Hilmas, G.E., 2013. Effects of temperature and the incorporation of W on the oxidation of ZrB_2ceramics. *Corrosion Science*, 80, pp.221–228.

Kazemzadeh Dehdashti, M., Fahrenholtz, W.G. & Hilmas, G.E., 2013. Oxidation of zirconium diboride with niobium additions. *Journal of the European Ceramic Society*, 33(10), pp.1591–1598.

Kido, H., Takahashi, M., Tani, J., Sawairi, Y., et al., 2014. Laser patterning of thermoelectric iron silicide on alumina substrates by continuous-wave ytterbium fiber laser irradiation. *Journal of the Ceramic Society of Japan*, 122(9), pp.802–805.

Kido, H., Takahashi, M., Tani, J., Chigane, M., et al., 2014. Modification of electrical properties of TiO_2 by continuous-wave ytterbium fiber laser irradiation. *Journal of the Ceramic Society of Japan*, 1(122), pp.21–24.

Kido, H. et al., 2011. Modification of electrical properties of zinc oxide by continuous wave ytterbium fiber laser irradiation. *IOP Conference Series: Materials Science and Engineering*, 18, pp.1–4.

Kim, S. et al., 2014. Change in microstructures and physical properties of ZrB_2–SiC ceramics hot-pressed with a variety of SiC sources. *Ceramics International*, 40(2), pp.3477–3483.

King, D.S., Fahrenholtz, W.G. & Hilmas, G.E., 2013. Silicon carbide–titanium diboride ceramic composites. *Journal of the European Ceramic Society*, 33(15–16), pp.2943–2951.

Kirubakaran, A., Jain, S. & Nema, R.K., 2009. A review on fuel cell technologies and power

electronic interface. *Renewable and Sustainable Energy Reviews*, 13(9), pp.2430–2440.

Krasnikov, A.S., Berezhnoi, A.I. & Mirkin, L.I., 1999. Science for ceramic production treatment: Structure and properties of ceramic materials after laser treatment. *Glass and Ceramics*, 56, pp.172–176.

Kreuer, K.D., 1997. On the development of proton conducting materials for technological applications. *Solid State Ionics*, 97(1–4), pp.1–15.

Kulpa, A. & Troczynski, T., 1996. Oxidation of TiB_2 below 900 °C. *Communications of the American Ceramic Society*, 79(2), pp.518–520.

Larminie, J. & Dicks, A., 2001. *Fuel Cell Systems Explained*,

Lee, K.-S., Seo, D.-K. & Whangbo, M.-H., 1997. Structural and Electronic Factors Governing the Metallic and Nonmetallic Properties of the Pyrochlores $A_2Ru_2O_{7-y}$. *Journal of Solid State Chemistry*, 408(131), pp.405–408.

Lee, K.T., Yoon, H.S. & Wachsman, E.D., 2012. The evolution of low temperature solid oxide fuel cells. *Journal of Materials Research*, 27(16), pp.2063–2078.

Li, C.-X. et al., 2012. Microstructure, performance and stability of Ni/Al_2O_3 cermet-supported SOFC operating with coal-based syngas produced using supercritical water. *International Journal of Hydrogen Energy*, pp.1–6.

Li, H. et al., 2010. Crystal structure and elastic properties of ZrB compared with ZrB_2: A first-principles study. *Computational Materials Science*, 49(4), pp.814–819.

Li, N. et al., 2013. Effects of oxygen partial pressure and atomic oxygen on the microstructure of oxide scale of ZrB_2–SiC composites at 1500°C. *Corrosion Science*, 73, pp.44–53.

Li, W. et al., 2009. Microstructure and mechanical properties of zirconia-toughened ZrB_2–$MoSi_2$ composites prepared by hot-pressing. *Scripta Materialia*, 60(2), pp.100–103.

Li, W.-J., Tu, R. & Goto, T., 2006. Preparation of TiC-TiB_2-SiC Ternary Eutectic Composites by Arc-Melting and Their Characterizations. *Materials Transactions*, 47(4), pp.1193–1197.

Li, X. et al., 2006. Effect of ZrB_2 on the ablation properties of carbon composites. *Materials Letters*, 60(7), pp.892–896.

Lilavivat, V. et al., 2015. Current Distribution Mapping for PEMFCs. *Electrochimica Acta*, 174, pp.1253–1260.

Lin, J. et al., 2014. Oxidation behavior and phase transition of ZrB_2–SiC_{w2}–ZrO_{2f} ceramic. *Corrosion Science*, 78, pp.13–21.

Lonné, Q. et al., 2011. Fabrication and characterization of ZrB_2–SiC ceramic electrodes coated with a proton conducting, SiO_2-rich glass layer. *Electrochimica Acta*, 56(20), pp.7212–7219.

Lonné, Q., 2011. *Réactivité et densification sous irradiation laser de composites ZrB_2 – SiC : application aux piles à combustible*. Université de Limoges.

Lonné, Q., Glandut, N. & Lefort, P., 2012. Laser densification of porous ZrB_2-SiC composites. *Processing and Properties of Advanced Ceramics and Composites IV: Ceramic Transactions Volume 234*, 234, pp.199–209.

Lonné, Q., Glandut, N. & Lefort, P., 2012. Surface densification of porous ZrB_2–39mol.% SiC ceramic composites by a laser process. *Journal of the European Ceramic Society*, 32(4), pp.955–963.

Loong, C.W., 2014. *Fabrication of sulfonated poly (ether ether ketone) (SPEEK)-Calcium oxide multilayer membrane for fuel cell application*. Universiti Malaysia Sarawak.

Lü, Z. et al., 2011. Processing and properties of ZrB_2–SiC composites obtained by aqueous tape casting and hot pressing. *Ceramics International*, 37(1), pp.293–301.

Lusquiños, F. et al., 2008. Laser cladding of SiC/Si composite coating on Si–SiC ceramic substrates. *Surface and Coatings Technology*, 202(9), pp.1588–1593.

Ma, H.-B. et al., 2015. Pressureless sintering, mechanical properties and oxidation behavior of ZrB_2 ceramics doped with B_4C. *Journal of the European Ceramic Society*, 35(10), pp.2699–2705.

Mahato, N. et al., 2015. Progress in material selection for solid oxide fuel cell technology: A review. *Progress in Materials Science*, 72, pp.141–337.

Mahmod, D.S.A. et al., 2015. Surface oxidation of porous ZrB_2-SiC ceramic composites by continuous-wave ytterbium fibre laser. *Applied Surface Science*, 357, pp.1982–1990.

Majumdar, J.D. & Manna, I., 2003. Laser processing of materials. , 28(August), pp.495–562.

Mallik, M. et al., 2017. Effect of SiC content on electrical, thermal and ablative properties of pressureless sintered ZrB_2-based ultrahigh temperature ceramic composites. *Journal of the European Ceramic Society*, 37(2), pp.559–572.

Mashhadi, M., Khaksari, H. & Safi, S., 2015. Pressureless sintering behavior and mechanical properties of ZrB_2– SiC composites : effect of SiC content and particle size. *Integrative Medicine Research*, 4(4), pp.416–422.

Menzler, N.H. et al., 2010. Materials and manufacturing technologies for solid oxide fuel cells. *Journal of Materials Science*, 45(12), pp.3109–3135.

Minh, N.Q., 2004. Solid oxide fuel cell technology - features and applications. *Solid State Ionics*, 174(1–4), pp.271–277.

Mohamed, W., Atan, R. & Yiap, T., 2009. Current and possible future applications of hydrogen fuel cells in Malaysia. *Proceedings of International Conference on Advances in Mechanical Engineering (ICAME) 2009*, pp.1–9.

Mohamed N. Rahaman, 2003. *Ceramic processing and sintering*, New York: Marcel Dekker Inc.

Mougin, F.L.G.G.J. et al., 2009. Current status of proton-conducting solid oxide fuel cells development. *Journal of Applied Electrochemistry*, 39(4), pp.535–543.

Mukhopadhyay, A. et al., 2007. Pressureless sintering of ZrO_2–ZrB_2 composites: Microstructure and properties. *International Journal of Refractory Metals and Hard Materials*, 25(2), pp.179–188.

Munro, R.G., 2000. Material properties of titanium diboride. *Journal of Research of the National Institute of Standards and Technology*, 105(5), p.709.

Nánai, L., Vajtai, R. & F. George, T., 1997. Laser-induced oxidation of metals: state of the art. *Thin Solid Films*, 298, pp.160–164.

Napoli, R. et al., 2015. Techno-economic analysis of PEMFC and SOFC micro-CHP fuel cell systems for the residential sector. *Energy and Buildings*, 103, pp.131–146.

Nasani, N. et al., 2015. Electrochemical behaviour of Ni-BZO and Ni-BZY cermet anodes for

Protonic Ceramic Fuel Cells (PCFCs) – A comparative study. *Electrochimica Acta*, 154, pp.387–396.

Nasani, N. et al., 2013. Synthesis and conductivity of $Ba(Ce,Zr,Y)O_{3-\delta}$ electrolytes for PCFCs by new nitrate-free combustion method. *International Journal of Hydrogen Energy*, 38(20), pp.8461–8470.

Nasani, N. et al., 2014. The impact of porosity, pH_2 and pH_2O on the polarisation resistance of $Ni–BaZr_{0.85}Y_{0.15}O3−\delta$ cermet anodes for Protonic Ceramic Fuel Cells (PCFCs). *International Journal of Hydrogen Energy*, 39(36), pp.21231–21241.

National, I. & Recherche, D., 2008. Silicon Carbide : Synthesis and Properties. , (C), pp.361–389.

Neuman, E.W., Hilmas, G.E. & Fahrenholtz, W.G., 2015. Mechanical behavior of zirconium diboride-silicon carbide-boron carbide ceramics up to 2200◦C. *Journal of the European Ceramic Society*, 35, pp.463–467.

Neuman, E.W., Hilmas, G.E. & Fahrenholtz, W.G., 2013. Mechanical behavior of zirconium diboride–silicon carbide ceramics at elevated temperature in air. *Journal of the European Ceramic Society*, 33(15–16), pp.2889–2899.

Novaresio, V. et al., 2012. An open-source library for the numerical modeling of mass-transfer in solid oxide fuel cells. *Computer Physics Communications*, 183(1), pp.125–146.

O'Hayre, R.P. et al., 2006. *Fuel cell fundamentals*, Wiley.

Oliveros, A., Guiseppi-Elie, A. & Saddow, S.E., 2013. Silicon carbide: a versatile material for biosensor applications. *Biomedical microdevices*, 15(2), pp.353–68.

Ormerod, R.M., 2003. Solid oxide fuel cells. *Chemical Society Reviews*, 32(1), pp.17–28.

Patel, M. et al., 2012. Strength of hot pressed ZrB_2–SiC composite after exposure to high temperatures (1000–1700°C). *Journal of the European Ceramic Society*, 32(16), pp.4455–4467.

Peng, F., 2008. *Pressureless Sintering and Oxidation Resistance of ZrB_2 based Ceramic Composites*. Georgia Institute of Technology.

Pines, M.L., 2004. *Pressureless Sintering of Powder Processed Functionally Graded Metal-Ceramic Plates*. University of Maryland, College Park.

Qian, B. & Shen, Z., 2013. Laser sintering of ceramics. *Journal of Asian Ceramic Societies*, 1(4), pp.315–321.

Qu, Z. et al., 2016. Fabrication and characterization of B_4C-ZrB_2-SiC ceramics with simultaneously improved high temperature strength and oxidation resistance up to 1600 °C. *Ceramics International*, 42(7), pp.8000–8004.

Ralph, J.M., Schoeler, A.C. & Krumpelt, M., 2001. Materials for lower temperature solid oxide fuel cells *. *Journal of Materials Science*, 6(36), pp.1161–1172.

Rams, J. et al., 2007. Surface treatment of aluminum matrix composites using a high power diode laser. *Surface and Coatings Technology*, 202(4–7), pp.1199–1203.

Rayment, C. & Sherwin, S., 2003. *Introduction to Fuel Cell Technology*, Notre Dame, U.S.A.

Reed, M.W. & Brodd, R.J., 1965. Porous Carbon for Fuel Cell Electrodes. *Carbon*, 3, pp.241–246.

Rezaie, A., Fahrenholtz, W.G. & Hilmas, G.E., 2007. Evolution of Structure during the Oxidation of Zirconium Diboride–Silicon Carbide in Air up to 1500°C. *Journal of the European Ceramic Society*, 27(6), pp.2495–2501.

Richter, J. et al., 2009. Materials design for perovskite SOFC cathodes. *Monatshefte für Chemie - Chemical Monthly*, 140(9), pp.985–999.

Royon, R. et al., 2013. High power, continuous-wave ytterbium-doped fiber laser tunable from 976 to 1120 nm. *Optics Express*, 21(11), p.13818.

Sahibzada, M. et al., 2000. Intermediate temperature solid oxide fuel cells operated with methanol fuels. *Chemical Engineering Science*, 55(16), pp.3077–3083.

Sai Krupa, M. et al., 2013. Effect of zirconium diboride addition on the properties of silicon carbide composites. *Ceramics International*, 39(8), pp.9567–9574.

Saigal, A., 2007. Fabrication of Low Temperature Solid Oxide Fuel Cells with Ultra-Thin Film Yttria-Stabilized Zircona Electrolytes. *National Nanotechnology Infrastructure Network*,

pp.72–73.

Samant, A.N. & Dahotre, N.B., 2009. Laser machining of structural ceramics—A review. *Journal of the European Ceramic Society*, 29(6), pp.969–993.

Sarin, P. et al., 2010. In situ studies of oxidation of ZrB_2 and ZrB_2–SiC composites at high temperatures. *Journal of the European Ceramic Society*, 30(11), pp.2375–2386.

Scientific, H., 2010. a Guidebook To Particle Size Analysis. *Distribution*, pp.1–17.

Shahedi Asl, M., Sabahi Namini, A. & Ghassemi Kakroudi, M., 2016. Influence of silicon carbide addition on the microstructural development of hot pressed zirconium and titanium diborides. *Ceramics International*, 42(4), pp.5375–5381.

Shao, Z. & Haile, S.M., 2004. A high-performance cathode for the next generation of solid-oxide fuel cells. *Nature*, 431(7005), pp.170–3.

Shirakawa, A. et al., 2011. High power ytterbium fiber lasers at extremely long wavelengths by photonic bandgap fiber technology. *2011 IEEE Winter Topicals, WTM 2011*, 16(6), pp.183–184.

Simonenko, E.P. et al., 2013. Promising ultra-high-temperature ceramic materials for aerospace applications. *Russian Journal of Inorganic Chemistry*, 58(14), pp.1669–1693.

Singhal, S., 2000. Advances in solid oxide fuel cell technology. *Solid State Ionics*, 135(1–4), pp.305–313.

Singhal, S.C. & Kendall, K., 2003. High Temperature and Solid Oxide Fuel Cells. In *High Temperature and Solid Oxide Fuel Cells*. pp. xv–xvi.

Slavica Ristić, Suzana Polić, Bojana Radojković, J.S., 2014. Analysis of ceramics surface modification induced by pulsed laser treatment. *Processing and Application of Ceramics*, 8(1), pp.15–23.

Snyder, A. et al., 2012. The effect of heating rate and composition on the properties of spark plasma sintered zirconium diboride based composites. *Materials Science and Engineering: A*, 538, pp.98–102.

Souza, S. De, Visco, S.J. & Jonghe, L.C. De, 1997. Thin-film solid oxide fuel cell with high

performance at low- temperature. *Solid State Ionics*, 98, pp.57–61.

Specac, 2013. Atlas Manual Hydraulic Press Datasheet. , p.1. Available at: http://www.specac.com/userfiles/file/MD20ManualPress.pdf.

Spivey, B.J. & Edgar, T.F., 2012. Dynamic modeling, simulation, and MIMO predictive control of a tubular solid oxide fuel cell. *Journal of Process Control*, pp.1–19.

Stambouli, A.B. & Traversa, E., 2002. Solid oxide fuel cells (SOFCs): a review of an environmentally clean and efficient source of energy. *Renewable and Sustainable Energy Reviews*, 6, pp.433–455.

Steele, B.C. & Heinzel, a, 2001. Materials for fuel-cell technologies. *Nature*, 414(6861), pp.345–52.

Steen, W.M. & Mazumder, J., 2010. *Laser Material Processing*, Springer.

Subhash C Singhal & Kendall, K., 2003. *High Temperature Solid Oxide Fuel Cells: Fundamentals, Design and Applications*,

Sun, C.-N., Baldridge, T. & Gupta, M.C., 2009. Fabrication of ZrB_2–Zr cermet using laser sintering technique. *Materials Letters*, 63(28), pp.2529–2531.

Sun, C.-N. & Gupta, M.C., 2008. Laser Sintering of ZrB_2. *Journal of the American Ceramic Society*, 91(5), pp.1729–1731.

Sun, C. & Stimming, U., 2007. Recent anode advances in solid oxide fuel cells. *Journal of Power Sources*, 171(2), pp.247–260.

Tadros, T., 2013. Ostwald Ripening. In T. Tadros, ed. *Encyclopedia of Colloid and Interface Science*. Berlin, Heidelberg: Springer Berlin Heidelberg, p. 820.

Tampieri, A., Landi, E. & Bellosi, A., 1992. On the oxidation behaviour of monolithic TiB_2 and Al_2O_3-TiB_2 and Si_3N_4-TiB_2 composites. *Journal of Thermal Analysis*, 38(12), pp.2657–2668.

Taroco, H.A. et al., 2011. Ceramic Materials for Solid Oxide Fuel Cells. In *Advances in Ceramics - Synthesis and Characterization, Processing and Specific Applications*. pp. 423–446.

Thévenot, F., 1990. Boron carbide-A comprehensive review. *Journal of the European Ceramic*

Society, 6(4), pp.205–225.

Tian, C. et al., 2011. Oxidation behaviour of zirconium diboride–silicon carbide ceramic composites under low oxygen partial pressure. *Corrosion Science*, 53(11), pp.3742–3746.

Tietz, F., Buchkremer, H. & Stöver, D., 2002. Components manufacturing for solid oxide fuel cells. *Solid State Ionics*, 152–153(2), pp.373–381.

Torizuka, S. et al., 1995. Effect of SiC on Interfacial Reaction and Sintering Mechanism of TiB_2. *Journal American Ceramic Society*, 78(6), pp.1606–1610.

Triantafyllidis, D., Li, L. & Stott, F.H., 2006. Crack-free densification of ceramics by laser surface treatment. *Surface and Coatings Technology*, 201(6), pp.3163–3173.

Tseronis, K., Kookos, I.K. & Theodoropoulos, C., 2008. Modelling mass transport in solid oxide fuel cell anodes: a case for a multidimensional dusty gas-based model. *Chemical Engineering Science*, 63(23), pp.5626–5638.

University of Miskolc, 2014. Surface Engineering: Laser Surface Treatment. *Miskolc, University of Centre, North Hungary Regional Distance*, pp.2–7. Available at: http://emrtk.uni-miskolc.hu/projektek/adveng/home/kurzus/korsz_anyagtech/1_konzultacio_elemei/laser_surface_treat.htm.

Veyko, V.P., 2008. Local Laser Oxidation of Thin Metal Films: Ultra-resolution in Theory and in Practice. *Journal of Laser Micro/Nanoengineering*, 3(3), pp.201–205.

Vlasova, M. et al., 2009. Laser irradiation of α-SiC ceramics. *Ceramics International*, 35(6), pp.2503–2508.

Wachsman, E. & Singhal, S., 2009. Solid oxide fuel cell commercialization, research and challenges. *The Electrochemical Society Interface*, (Fall), pp.38–43.

Wachsman, E.D. & Lee, K.T., 2011. Lowering the Temperature of Solid Oxide Fuel Cells. *Science*, 334, pp.935–939.

Wang, X.-G., Guo, W.-M. & Zhang, G.-J., 2009. Pressureless sintering mechanism and microstructure of ZrB2–SiC ceramics doped with boron. *Scripta Materialia*, 61(2), pp.177–180.

Wang, Y. et al., 2011. A review of polymer electrolyte membrane fuel cells: Technology, applications, and needs on fundamental research. *Applied Energy*, 88(4), pp.981–1007.

Wuchina, E. et al., 2007. UHTCs : Ultra-High Temperature Ceramic Materials for Extreme Environment Applications. *The Electrochemical Society Interface*, pp.30–35.

Xie, Z. et al., 2006. $Fe_xCo_{0.5-x}Ni_{0.5}$–SDC anodes for low-temperature solid oxide fuel cells. *Electrochimica Acta*, 51, pp.3052–3057.

Yan, Y. et al., 2006. Pressureless Sintering of High-Density ZrB_2-SiC Ceramic Composites. *Journal of the American Ceramic Society*, 89(11), pp.3589–3592.

Yang, D. et al., 2007. Low temperature solid oxide fuel cells with pulsed laser deposited bi-layer electrolyte. *Journal of Power Sources*, 164, pp.182–188.

Yang, X. et al., 2013. ZrB_2/SiC as a protective coating for C/SiC composites: Effect of high temperature oxidation on mechanical properties and anti-ablation property. *Composites Part B: Engineering*, 45(1), pp.1391–1396.

Yano, M. et al., 2007. Recent advances in single-chamber solid oxide fuel cells: A review. *Solid State Ionics*, 177(39–40), pp.3351–3359.

Zha, S., Rauch, W. & Liu, M., 2004. Ni-$Ce_{0.9}Gd_{0.1}O_{1.95}$ anode for GDC electrolyte-based low-temperature SOFCs. *Solid State Ionics*, 166(3–4), pp.241–250.

Zhang, H. et al., 2009a. Pressureless sintering of ZrB_2-SiC ceramics: the effect of B_4C content. *Scripta Materialia*, 60(7), pp.559–562.

Zhang, H. et al., 2009b. Properties of ZrB_2 -SiC Ceramics by Pressureless Sintering. *Journal of the American Ceramic Society*, 92(7), pp.1599–1602.

Zhang, S.C., Hilmas, G.E. & Fahrenholtz, W.G., 2008. Pressureless Sintering of ZrB_2-SiC Ceramics. *Journal of the American Ceramic Society*, 91(1), pp.26–32.

Zhang, X. et al., 2007. Internal shorting and fuel loss of a low temperature solid oxide fuel cell with SDC electrolyte. *Journal of Power Sources*, 164(2), pp.668–677.

Zhang, X.-H., Hu, P. & Han, J.-C., 2011. Structure evolution of ZrB_2–SiC during the oxidation in air. *Journal of Materials Research*, 23(7), pp.1961–1972.

Zhang, Y. et al., 2015. Micromachining features of TiC ceramic by femtosecond pulsed laser. *Ceramics International*, 41(5), pp.6525–6533.

Zhao, G. et al., 2014a. A study on in-situ synthesis of TiB_2–SiC ceramic composites by reactive hot pressing. *Ceramics International*, 40(1), pp.2305–2313.

Zhao, G. et al., 2014b. Microstructure and mechanical properties of hot pressed TiB_2-SiC composite ceramic tool materials at room and elevated temperatures. *Materials Science and Engineering A*, 606, pp.108–116.

Zhi, M. et al., 2012. An intermediate-temperature solid oxide fuel cell with electrospun nanofiber cathode. *Energy & Environmental Science*, 5(5), p.7066.

Zhu, B., 2003. Functional ceria-salt-composite materials for advanced ITSOFC applications. *Journal of Power Sources*, 114(1), pp.1–9.

Zhu, B. et al., 2003. Innovative low temperature SOFCs and advanced materials. *Journal of Power Sources*, 118(1–2), pp.47–53.

Zhu, M. & Wang, Y., 2009. Pressureless sintering ZrB_2–SiC ceramics at low temperatures. *Materials Letters*, 63(23), pp.2035–2037.

Zhu, S., Fahrenholtz, W.G. & Hilmas, G.E., 2007. Influence of silicon carbide particle size on the microstructure and mechanical properties of zirconium diboride–silicon carbide ceramics. *Journal of the European Ceramic Society*, 27(4), pp.2077–2083.

Zhu, W.Z. & Deevi, S.C., 2003. A review on the status of anode materials for solid oxide fuel cells. *Materials Science and Engineering: A*, 362(1–2), pp.228–239.

Zimmermann, J.W. et al., 2008. Thermophysical Properties of $ZrB_2$and ZrB_2–SiC Ceramics. *Journal of the American Ceramic Society*, 91(5), pp.1405–1411.

APPENDIX A

Ytterbium Fibre Laser Commands

Table A-1: Ytterbium fiber laser commands description for round spiral pattern.

Line No.	Axis	Command	Unit	Description
1	1	mo		Turn axis #1 motor power on
2	2	mo		Turn axis #2 motor power on
3	1	hn	1,2	Create a new group (#1) with physical axes 1 and 2
4	1	hv	0.5	Set vectorial velocity of group #1 to 0.5units/second
5	1	ha	0.25	Set vectorial acceleration of group #1 to 0.25 units/second2
6	1	hd	0.25	Set vectorial deceleration of group #1 to 0.25 units/second2
7	1	ho		Turn group #1 power ON
8	1	hc	0,0.1,180	Set axis #1 arc center = 0 unit Set axis #2 arc center = 0.1 unit Set sweep angle of arc = 180 degrees
9	1	hw		Wait for the group to reach target position
10	1	hc	0,-0.1,180	Set axis #1 arc center = 0 unit Set axis #2 arc center = -0.1 unit Set sweep angle of arc = 180 degrees
11	1	hw		Wait for the group to reach target position
12	1	hc	0,0.1,180	Set axis #1 arc center = 0 unit Set axis #2 arc center = 0.1 unit Set sweep angle of arc = 180 degrees
13	1	hw		Wait for the group to reach target position
14	1	hc	0,-0.1,180	Set axis #1 arc center = 0 unit Set axis #2 arc center = -0.1 unit Set sweep angle of arc = 180 degrees
15	1	hw		Wait for the group to reach target position
16	1	hc	0,0.1,180	Set axis #1 arc center = 0 unit Set axis #2 arc center = 0.1 unit Set sweep angle of arc = 180 degrees
17	1	hw		Wait for the group to reach target position
18	1	hc	0,-0.1,180	Set axis #1 arc center = 0 unit Set axis #2 arc center = -0.1 unit Set sweep angle of arc = 180 degrees
19	1	hw		Wait for the group to reach target position
20	1	hc	0,0.1,180	Set axis #1 arc center = 0 unit Set axis #2 arc center = 0.1 unit Set sweep angle of arc = 180 degrees
21	1	hw		Wait for the group to reach target position
22	1	hc	0,-0.1,180	Set axis #1 arc center = 0 unit Set axis #2 arc center = -0.1 unit

				Set sweep angle of arc = 180 degrees
23	1	hw		Wait for the group to reach target position
24	1	hc	0,0.1,180	Set axis #1 arc center = 0 unit
				Set axis #2 arc center = 0.1 unit
				Set sweep angle of arc = 180 degrees
25	1	hw		Wait for the group to reach target position
26	1	hc	0,-0.1,180	Set axis #1 arc center = 0 unit
				Set axis #2 arc center = -0.1 unit
				Set sweep angle of arc = 180 degrees
27	1	hw		Wait for the group to reach target position
28	1	hc	0,0.1,180	Set axis #1 arc center = 0 unit
				Set axis #2 arc center = 0.1 unit
				Set sweep angle of arc = 180 degrees
29	1	hw		Wait for the group to reach target position
30	1	hc	0,-0.1,180	Set axis #1 arc center = 0 unit
				Set axis #2 arc center = -0.1 unit
				Set sweep angle of arc = 180 degrees
31	1	hw		Wait for the group to reach target position
32	1	hc	0,0.1,180	Set axis #1 arc center = 0 unit
				Set axis #2 arc center = 0.1 unit
				Set sweep angle of arc = 180 degrees
33	1	hw		Wait for the group to reach target position
34	1	hc	0,-0.1,180	Set axis #1 arc center = 0 unit
				Set axis #2 arc center = -0.1 unit
				Set sweep angle of arc = 180 degrees
35	1	hw		Wait for the group to reach target position
36	1	hc	0,0.1,180	Set axis #1 arc center = 0 unit
				Set axis #2 arc center = 0.1 unit
				Set sweep angle of arc = 180 degrees
37	1	hw		Wait for the group to reach target position
38	1	hc	0,-0.1,180	Set axis #1 arc center = 0 unit
				Set axis #2 arc center = -0.1 unit
				Set sweep angle of arc = 180 degrees
39	1	hw		Wait for the group to reach target position
40	1	hc	0,0.1,180	Set axis #1 arc center = 0 unit
				Set axis #2 arc center = 0.1 unit
				Set sweep angle of arc = 180 degrees
41	1	hw		Wait for the group to reach target position
42	1	hc	0,-0.1,180	Set axis #1 arc center = 0 unit
				Set axis #2 arc center = -0.1 unit
				Set sweep angle of arc = 180 degrees
43	1	hw		Wait for the group to reach target position
44	1	hc	0,0.1,180	Set axis #1 arc center = 0 unit
				Set axis #2 arc center = 0.1 unit
				Set sweep angle of arc = 180 degrees
45	1	hw		Wait for the group to reach target position

46	1	hc	0,-0.1,180	Set axis #1 arc center = 0 unit Set axis #2 arc center = -0.1 unit Set sweep angle of arc = 180 degrees

The meaning of laser command description is as follows:

a) mo = motor on
b) hn = create new group
c) hv = set group velocity
d) ha = set group acceleration
e) hd = set group deceleration
f) ho = group on
g) hw = move group along an arc

APPENDIX B

Publications

Article B-1: Journal Publication

a) **Dayang Salyani Abang Mahmod**, Amir Azam Khan, Nicolas Glandut, Jean-Claude Labbe, An evaluation of the B_4C formation in sintered ZrB_2-SiC ceramic composites at 2100 °C, *Journal of Alloys and Compounds, Volume 735, 25 February 2018, Pages 510-515. https://doi.org/10.1016/j.jallcom.2017.11.170.*

b) **D.S.A. Mahmod**, M. Andrew-Munot, A.A. Khan, N. Glandut and J.-C. Labbe, Laser Surface Treatment of Porous Ceramic Substrate for Application in Solid Oxide Fuel Cells, *14th International Symposium on Advanced Materials (ISAM 2015). IOP Conference Series: Materials Science and Engineering 146 (2016) 012002, Pages 1-7. doi:10.1088/1757-899X/146/1/012002.*

c) **Dayang Salyani Abang Mahmod,** Nicolas Glandut, Amir Azam Khan, Jean-Claude Labbe, Surface oxidation of porous ZrB_2-SiC ceramic composites by continuous-wave ytterbium fibre laser, *Applied Surface Science, Volume 357, Part B, 1 December 2015, Pages 1982-1990. http://dx.doi.org/10.1016/j.apsusc.2015.09.164.*

Article B-2: Conference Paper

d) **D.S.A. Mahmod**, M. Andrew-Munot, A.A. Khan, N. Glandut and J.-C. Labbe, Laser Surface Treatment of Porous Ceramic Substrate for Application in Solid Oxide Fuel Cells, *14th International Symposium on Advanced Materials (ISAM 2015). IOP Conference Series: Materials Science and Engineering 146 (2016) 012002, Pages 1-7. doi:10.1088/1757-899X/146/1/012002.*

e) **D.S.A. Mahmod**, M. Andrew-Munot, A.A. Khan, N. Glandut and J.-C. Labbe, Formation of a Silica-rich glassy outer layer of ZrB_2-SiC Composite by Continuous Wave Ytterbium Fibre Laser Irradiation, 7th *International Engineering Conference, Energy and Environment (ENCON 2014),* ISBN*: 978-981-09-4587-9*, *Pages 129-135. doi: 10.3850/978-981-09-4587-9_P18.*

f) **D.S.A. Mahmod**, M. Andrew-Munot, A.A. Khan, N. Glandut and J.-C. Labbe, Advanced Materials for Low Temperature Solid Oxide Fuel Cells (LTSOFCs): A Review, *6th International Engineering Conference, Energy and Environment (ENCON 2013), ISBN: 978-981-07-6059-5, Pages 573-580. doi: 10.3850/978-981-07-6059-5_149.*

Poster B-3: Poster Presentation

g) **D.S.A. Mahmod**, M. Andrew-Munot, A.A. Khan, N. Glandut and J.-C. Labbe, Innovative Ceramic Electrodes for Low Temperature Solid Oxide Fuel Cell (LT-SOFC), *STEMFest Exhibition & Tradeshow 2013 PROSPECTUS, UNIMAS International Festival of Science, Technology, Engineering and Mathematics.*